EVENT CLASSIFICATION FOR 3-D POSITION SENSITIVE SEMICONDUCTOR DETECTORS

by

Stephen E. Anderson

A dissertation submitted in partial fulfillment
of the requirements for the degree of
Doctor of Philosophy
(Nuclear Engineering and Radiological Sciences)
in The University of Michigan
2011

Doctoral Committee:

Professor Zhong He, Chair
Professor Frederick D. Becchetti, Jr
Professor Ronald F. Fleming
Associate Professor Sara A. Pozzi

To my family.

ACKNOWLEDGEMENTS

I am humbled as I look back at my academic career and remember the individuals who made it possible. To the family, friends, mentors, teachers, fellow students, and staff members who have supported me in this journey, it is my hope that you do not measure my gratitude by these words alone.

Financial support for this research was provided by the U.S. Department of Defense, and the U.S. Department of Energy.

TABLE OF CONTENTS

LIST OF FIGURES

Figure

LIST OF TABLES

Table

CHAPTER I

Introduction

1.1 Event Classification for Three-Dimensional Position-Sensitive Semiconductor Detectors

Event classification is the process of measuring the detailed interaction history of energetic particles in a detection medium. This thesis demonstrates how event classification based on digitized preamplifier output pulse waveforms from 3-D position sensitive semiconductor detectors improves the key performance parameters of a gamma-ray imaging spectrometer. To accomplish this goal, simulations and experiments have been conducted using large volume pixelated CdZnTe (CZT) and HgI_2 detectors. A new experimental tool developed for this study is a prototype digital pulse waveform readout system. Data collected by this system provide a basis for the development of photon event classification algorithms for pixelated 3-D semiconductor detectors.

Accurate classification of individual radiation interaction histories has two general components. The first is identification of the specific interaction mechanism. Examples include the ability to distinguish between a pair production and a Compton scatter interactions, and identification of photoelectric absorption. The second component is identification of systematic interaction complexities. This type of classification is necessitated by the relatively complex pixelated design of the high-energy

photon detectors used in this study. Examples of system-based event classifications include identification of charge sharing between neighboring pixels and detection of multiple photon interactions. Classification of multiple photon interactions includes detection of multiple interactions from a single source photon (Compton scatter, pair production, characteristic x-ray) and events from more than one source photon (pulse pile-up).

The ideal event classification algorithm would process data from a single interaction history in a detector and return a probability that the event falls in a specific classification category. An example will help illustrate the concept. Imagine that a 1.5 MeV gamma-ray interacts in a detector depositing all of its energy. Without knowing any further information, the interaction could be a Compton scattering sequence, a single photoelectric absorption, or pair production. Since the interaction position can be measured in three dimensions, it is further observed that this particular interaction history contains four separate energy deposition locations. The energies, as well as the location of the interactions are sent into an event classification algorithm. The event might be classified as pair production if the energies of the annihilation radiation add up correctly and are deposited in the expected locations relative to the location of the pair creation. If annihilation radiation is not detected, the likelihood of Compton scattering would dominate and subsequent classifications of this event, such as detection of a characteristic X-ray or charge sharing, yield additional useful information.

Event classification adds another dimension to the event-by-event response of a 3-D detector. Traditionally, the amount of energy deposited and the interaction location are the sole information available to reconstruct an event. Each interaction in a single event history has an associated energy and position. For example,

a typical Compton scatter might have two interactions with the following energy and position parameters: (E_1, x_1, y_1, z_1), and (E_2, x_2, y_2, z_2). The subsequent reconstruction of the event would be combined with other events to generate spectra and/or images of the radiation source. Event classification adds an additional dimension to each individual interaction history in the hope of improving the final aggregate response(s). For example, the Compton sequence described above would add event classification parameters to the existing energy and position measurements: $[(E_1, x_1, y_1, z_1), (E_2, x_2, y_2, z_2), \mathbf{C}, \mathbf{P}]$ where $\mathbf{C}$ is a set of possible event classifications and $\mathbf{P}$ are the corresponding likelihoods.

This additional information provides a variety of benefits, some of which will be explored in this study, while others are delegated to future work. However, the general benefit of event classification is an increase in physical knowledge of an event combined with a reduction of the systematic uncertainties associated with pixelated semiconductor detectors. These systematic errors occur every time an energy or interaction position is estimated or an event is chosen and sequenced for a Compton imaging application. The next chapter explores these sources of error in relation to the application of an imaging spectrometer, and introduces how event classification empowers a user to better correct these errors. Before addressing the details of event classification, the remainder of this chapter is devoted to developing a better understanding of the motivations, context, and scope of this study, including related work by other authors. At the end of the chapter, a list of the major goals and a summary of the work completed is presented.

1.2 Research Motivation

This study is motivated by the persistent demand for improvements in the spectroscopic and imaging performance of room temperature semiconductor detectors. The performance of this type of detector is limited by how accurately and efficiently it can measure the interaction position and energy deposition of X- or gamma ray radiation. As the following chapters demonstrate, the detectors used in this study represent state of the art technology in the continuing effort to optimize these factors. However, there are still opportunities for improvement. The availability of high-performance multichannel analog to digital conversion (ADC) electronics combined with the computational power of modern personal computers reveals new research avenues. The ability to digitize and subsequently analyze a pulse waveform via inherently flexible software opens the door to analysis and optimization techniques beyond the reach of traditional analog-based pulse analysis.

This thesis study began as an exploration into "what can be achieved by digitizing preamplifier output pulses instead of reading out analog pulse heights?" The study quickly moved from reproducing and improving on the performance of the analog system to more advanced topics such as sub-pixel interaction position calculation and classification of interactions on an event-by-event basis. This thesis represents the critical first steps in advancing the current performance limits of 3-D position-sensitive semiconductor detectors. Ultimately, the technical motivations of this work are closely tied to the end-use applications of this technology. The ability to measure the energy and source position of gamma and X-ray radiation is a central challenge in fields including astrophysics, medical imaging, radiation protection, nuclear terrorism prevention, and nuclear safeguards.

1.3 Thesis Context

While the previous sections naturally introduce the context of this study, it is important to explore how event classification fits into the broader research context of 3-D room temperature semiconductor detectors. It is useful to break this discussion into three sections: a history of the 3-D detectors used in this study, a brief background of the readout electronics, and the context of photon interaction classification algorithms.

1.3.1 Detector Background

The goal of this subsection is to understand how 3-D position-sensitive CZT and HgI_2 detectors fit into the larger field of X- and gamma ray spectroscopy and imaging. The detectors chosen for this study were designed for the purpose of room-temperature Compton imaging and spectroscopy for photons in the 30 keV to 3 MeV energy range. Compton imaging requires position sensing capability and spectroscopic information. To efficiently measure photons in this energy range, dense, high atomic number (Z), large volume detectors are preferred. Room temperature operation can be achieved using scintillators, gases, and wide band-gap semiconductors. The large-volume, pixelated CZT and HgI_2 semiconductor detectors used in this study meet all of these requirements. Table 1.1 is a summary of the properties of CZT and HgI_2. Details of the detectors used in this study are specified in chapter III.

Table 1.1: Properties of CZT and HgI_2 [33]

Material	Z	Density (g/cm^3)	Band Gap (eV)	Average Ionization Energy (eV/e-h pair)
CZT	48,30,52	6	1.64	5.0
HgI_2	80,53	6.4	2.13	4.3

Room temperature compound-semiconductor detector research is motivated by

the desire to combine the energy resolution of semiconductors, such as germanium and silicon, with additional desirable factors including a high-Z interaction medium and room temperature operation. As a result, wide band-gap compound semiconductor detectors such as CZT and HgI_2 have been under investigation for decades. Development of HgI_2 detectors began in the early 1970s [60, 61, 58]. In the early 1990s, CZT-based room temperature X- and gamma ray detectors were developed [7, 8, 13] to help solve the problem of polarization in earlier CdTe detectors. At first, the spectroscopic performance of CZT and HgI_2 detectors suffered from significant hole trapping. A monoenergetic particle interacting at different depths relative to an electrode would induce different amounts of charge on that electrode. The result was a continuous energy response to a monoenergetic source. This problem was ultimately solved by the application of single-polarity charge sensing methods including the coplanar-grid [41, 40] and small-pixel readout technologies [4] which are similar in principle with the earlier Frisch grid design for electron-sensitive ion chambers [16].

Single-polarity charge sensing solved the problem of poor hole mobility, but another problem arose as detector thickness increased. The signal amplitude resulting from electron motion in a detector varies with interaction position due to electron trapping and weighting potential effects of the electrode design. The solution for coplanar devices is known as the relative gain method [41]. This technique corrects the depth-dependant signal response through application of an appropriate relative electronic gain difference between the coplanar electrode signals. The other popular uniformity correction technique is based on the ability to sense the actual depth(s) of particle interaction in a detector. If the interaction location is known, corrections can be applied to normalize non-uniformities due to electron trapping,

weighting potential, and material non-uniformities. These methods were developed and demonstrated by He et al. in 1996 and 1997 [25, 24]. Because depth-sensing methods are used extensively in this thesis, details of the method are presented in chapter V.

The concept of a 3-D position-sensitive semiconductor detector soon followed as depth sensing methods were combined with the inherent lateral position knowledge that can be measured using a detector with a pixelated anode [26]. The ability to measure 3-D interaction position effectively divides a single detector into a large number of virtual sub-detectors. Physical and virtual segmentation, combined with accurate energy deposition measurements, allow for Compton imaging using a single detector crystal. A single pixelated CZT or HgI_2 detector can be operated as an imaging spectrometer. Today, the performance of these devices continues to improve as detector manufacturing methods, readout electronics, and event reconstruction methods improve. The energy resolution of some of the best systems is better than 0.5% full width at half maximum (FWHM) at 662 keV when interactions occur under a single pixel, and better than 1.0% FWHM at 662 keV for all events. Figure 1.1 is a comparison of ^{152}Eu spectra from NaI, CZT and high purity germanium (HPGe) detectors. The number of counts in the three spectra have been scaled and plotted on a log scale so that the features of each spectrum can be seen.

1.3.2 Readout Electronics Background

The design of the pixelated detectors used in this event classification study requires electronics capable of reading out the multiple independent channels of the individual electrodes of the detector. For example, the standard 11x11 pixel array would need at least 121 separate readout channels plus a channel for the planar cathode. The digital multichannel readout system used in this thesis is a 15-channel prototype

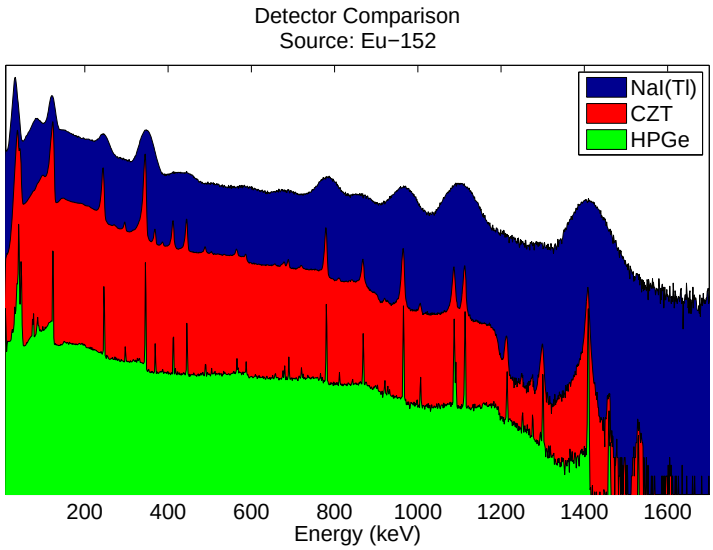

Figure 1.1: A comparison of ^{152}Eu spectra collected by NaI(Tl), CZT, and HPGe detectors.

system. The goal of this subsection is to place this prototype system in the context of the other analog and digital electronics used to readout 3-D detectors.

The use of application-specific integrated circuits (ASICs) for the detectors used in this study was first demonstrated in the late 1990s [39] and was succeeded by subsequent generations of ASICs resulting in consistent improvements in detector performance [38, 68, 64, 67, 63, 65, 17, 66, 59]. The details of each system are not relevant to this discussion. However, it is important to note the general capabilities of these ASIC systems since they are compared with the capabilities of the prototype digital readout system described in chapter III and with the performance of the event classification algorithms in chapter VI. A typical ASIC channel includes a preamplifier, shaping amplifiers for energy and timing, peak detection or peak hold circuitry, and a threshold discriminator. Ultimately, output voltage signals proportional to pulse heights and pulse trigger times for each individual lateral interaction position are sent to a digital interface so the data can be analyzed. Reference [18], and chapters 1 and 4 of reference [57] provide an excellent background to the components of

the analog readout electronics for semiconductor systems.

During the past two decades, pulse analysis using digitized waveforms has increased due to the availability of high-performance commercial digitizers including oscilloscopes and systems designed to interface with a PC. The sole requirement of a digitizer system is that it efficiently preserves the signal coming from a detector. Furthermore, the field of digital signal processing is a rich source of technology and methodology that can be applied to signals from radiation detectors. A useful resource that explains the basics of digital sampling systems can be found in reference [1]. References that provide more details related to nuclear detector systems include references [3, 48, 11]. Details and references to the digital signal processing methods used in this thesis are presented in chapter IV.

Digital readout systems similar to the one developed for this thesis have been used throughout the radiation detection research community. Examples that are closely related to the topic of 3-D semiconductor detectors include CZT and HgI_2 pulse timing studies [44, 45], and spectroscopic performance[46]. The ASICs used by CZT-based focusing telescope experiments such as the High Energy Focusing Telescope (HEFT) and the Nuclear Spectroscopic Telescope Array (NuSTAR) use capacitor banks to sample preamplifier outputs [10]. Another version of this ASIC known as the RadNet ASIC has been used for the Energetic X-ray Imaging Survey Telescope (EXIST) mission [27, 28] as well as homeland security applications [12]. As this thesis is being written, a new digital ASIC is being tested for use with the 3-D detectors analyzed in this study. Further details of this new system are presented in chapter VII.

1.3.3 Photon Interaction Classification Background

The goal of this subsection is to explore how the event classification algorithms developed in this thesis are connected to previous work. In the field of radiation detection there is a variety of techniques designed to characterize interactions in a specific detector. While it is beyond the scope of this study to examine these techniques in detail, it is valuable to include a brief list of methods that share analogous motivations with components of the methods developed in this study: pulse pileup rejection, Compton rejection[54], pair spectrometers[52, 43], and digital pulse shape discrimination[5].

The gain in popularity of segmented detectors has introduced the need for algorithms to identify and reconstruct events that take place in multiple detector segments. There are many examples of algorithms developed to better characterize such events. One category includes the gamma ray tracking detectors that are designed for nuclear spectroscopy experiments such as the Gamma-Ray Energy Tracking Array (GRETA) [36, 37]. These types of experiments rely on segmented HPGe detectors requiring algorithms to characterize single and multiple site interactions [35, 49]. More recently, Hayward has made a detailed study of charge sharing and incomplete charge collection in double sided strip HPGe detectors [20, 22]. He also goes on to describe how classification of "loss events" near the gap between strips allows for better detector performance[19, 21].

The most relevant work related to the classification algorithms presented in this thesis are the methods that have been developed for the actual 3-D room temperature detectors studied in this thesis. Charge sharing was analyzed in HgI_2 detectors by Meng [46]. Event reconstruction algorithms rely on identification of multiple pixel events in CZT detectors [63]. The relationship between charge sharing and multiple

pixel events for pixelated detectors including the effect of diffusion was modeled by Zhang [63]. In his Ph.D. thesis, Xu [62] identifies muon tracks in a 3-D CZT detector and specifies limitations related to pixelated CZT detectors including the need to better characterize charge sharing and multiple interactions occurring in a single pixel.

1.4 Thesis Scope and Overview

An understanding of the context of this work leads to the realization that there are an enormous number of research topics that one could choose. The primary purpose of this section is to state and qualify the specific goals of this thesis. The motivation and context of this work have already been presented in preceding sections of this chapter. Chapter II further defines the scope by presenting the relevant physical processes that are critical to this study, including photon interaction physics in CZT and HgI_2, and the physics of signal generation in a pixelated 3-D detector. However, the main goal of this work as a whole is to demonstrate the design, implementation, and performance of a prototype digital pulse waveform-based event classification system. This is accomplished in chapters III-VI.

The goals for the design and implementation of the event classification system can further be divided into two categories: hardware design and algorithm design. The goal of the hardware design component is to develop the electronics necessary to measure the time-dependant charge motion history for the existing standard 3-D position-sensitive semiconductor detectors used by the University of Michigan's room temperature semiconductor radiation measurements group. The technical requirements of this design are presented in chapter III. In summary, each electrode needs an independent readout channel capable of producing a low-noise voltage sig-

nal proportional to the induced charge variation on the electrode. This goal was accomplished through the development of two 15 channel discrete readout boards. One board is optimized for measuring CZT detectors, and the other is designed for HgI_2 detectors. The boards feature preamplifiers for as many as 14 pixels (out of a detector's 121 total pixels) as well as the cathode and grid bias networks. The second stage of the hardware design is the digitization electronics. In this case, the goal is to use commercially available multichannel digitizers to sample the preamplifier signals from the discrete readout board. This goal was accomplished through the use of digital oscilloscopes and a 16-channel PCI based digitizer system. Specifications of these components are given in section 3.3.

The goal of the event classification algorithm design is to develop software with the following general capabilities:

1. process digital pulse waveform data event-by-event,
2. measure signal features relevant to event classification and spectroscopy,
3. calculate and implement relevant calibration processes,
4. calculate interaction parameters such as energy deposition and interaction position,
5. assign an event classification and likelihood, and
6. event reconstruction.

The techniques associated with items 1 and 2 are presented in chapter IV. This chapter explains the signal processing methods that have been developed to extract valuable pulse waveform features including pulse height, the time of specific pulse features, charge collection, transient signal amplitude, and others. Initial steps are taken to optimize measurement of each waveform feature. Item 3, the waveform calibration step is described in chapter V. This chapter explains how the measurements made in chapter IV are converted to accurate energies and positions of the interaction

history in the detector. Chapter V includes a discussion of sub-pixel position calculations that allow interaction positions to be measured within a single pixel or voxel. Item 4, event classification, is covered in chapter VI. There are two major sections in chapter VI. The first presents the event classification procedure and the second describes how the methods have been verified using a collimator experiment and a sub-pixel experiment. The methods are also tested with data from the waveform simulation software described in chapter II. The last item, reconstruction, is also discussed in chapter VI. Proper event reconstruction improves the energy resolution and imaging performance of 3-D CZT and HgI_2 detectors. Chapter VII provides a summary of the thesis and discusses its impact on spectroscopy and imaging with 3-D CZT and HgI_2 detectors. Chapter VII also presents continuing and future work related to event classification in 3-D detectors.

CHAPTER II

Theoretical Considerations for Event Classification in 3-D Pixelated Detectors

Chapter II builds on the motivation for pulse waveform-based event classification described in chapter I by developing a theoretical foundation for the experimental, computational, and analytical methods that form the bulk of the remaining chapters. Chapter II also serves to further define the context and scope of this study by detailing the relevant physics of common photon interactions and their corresponding detector responses. Section 2.1 presents the three key photon interaction mechanisms in CZT and HgI_2. Section 2.2 examines the detector response to the ionizing interactions described in section 2.1. Section 2.3 introduces the waveform simulation software used to design and validate event classification algorithms. Finally, section 2.4 defines the concept of *interaction signatures* and illustrates how waveform signatures based on interaction physics and the expected detector response can be used to classify events in a pixelated 3D semiconductor detector.

2.1 Interaction Physics for Photon Interaction Events

A fundamental understanding of the mechanics of anticipated photon interactions is essential to the development of the analytical tools described in chapter VI. Because the detection systems in this study are designed to operate as gamma-ray

imaging spectrometers, photon interactions are the focus of this section. The classification of other types of particle interactions is possible in 3-D CZT and HgI_2 detectors; however, this subject is beyond the scope of this thesis.

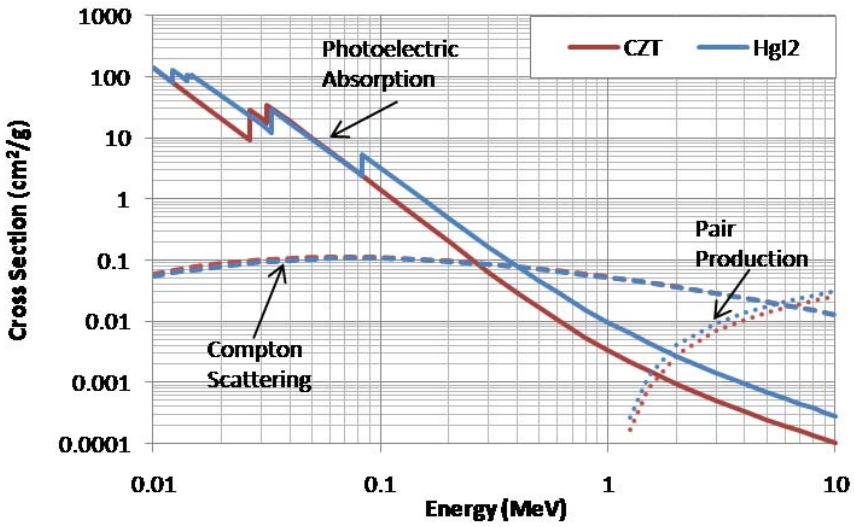

Figure 2.1: Photon cross sections for CZT and HgI_2 detector materials. Data for the plot are from tables in reference [6].

The photon interactions of interest are bound by the application and consequential design of the detector used. The detectors in this study are designed to detect photons between 30 keV and 3 MeV. Figure 2.1 compares the photon cross sections of CZT and HgI_2 for the three primary interactions between 10 keV and 10 MeV. At low energies, photoelectric absorption is the dominant interaction mechanism. At energies starting near 300 keV, Compton scattering is most likely. Pair production is possible starting at 1.022 MeV; however, it dominates above 5 MeV. The culminating goal of this chapter is to define waveform signatures that can be used to classify these three photon interactions. First, it is important to understand the physics of these three interaction mechanisms in CZT and HgI_2.

2.1.1 Photoelectric Absorption

Photoelectric absorption is the desired interaction for the detectors studied in this thesis. Measurements of photon energy are most accurate when they deposit all of their energy in a detector. Complete energy deposition is only possible through photoelectric absorption. As seen in Fig. 2.1, photoelectric absorption is the dominant mechanism below 300-400 keV. Photoelectric absorption following Compton scattering or interaction of annihilation radiation in the detector also yields a measurement of the full photon energy. A photoelectric absorption can only take place with an electron that is bound in an atom. About 80% of these interactions take place with electrons in the K-shell [14]. Following absorption, an electron is ejected from the atom with energy equal to the difference between the initial photon energy and the binding energy of the electron. For low photon energies, the emission direction of the photoelectron is most likely in the direction of the photon's electric field, normal to the direction of the photon. At higher energies, the photoelectron is more likely to be released in the direction that the incident photon was traveling. Theoretical distributions of these ejection directions for photons between 20 keV and 2.76 MeV can be found in reference [14], pages 696-697.

Once a photoelectron is ejected, the vacancy in the ionized atom is filled by an electron from another shell or an unbound electron in the system. The difference in energy between these two states is released as a characteristic X-ray. Table 2.1 lists the most likely characteristic X-ray energies for the detector materials used in this study. The table also lists the total K-shell yield and the K edge energy which provides an upper limit for the X-ray energy. Characteristic X-rays from transitions following a vacancy in L and other shells are also probable; however, the energy of these X-rays is too low to be of use in the event classification algorithms presented

in this study. Characteristic X-rays can also undergo absorption before leaving the atom. In this case, an Auger electron is released from the atom with an energy equal to the difference between the X-ray energy and the binding energy of the electron.

Table 2.1: Characteristic X-ray Energy (keV) and Atomic Yield (%) for the Elements of CZT and HgI_2 [15, 42, 34]

	$K_{\alpha 1}$		$K_{\alpha 2}$		$K_{\beta 1}$		$K_{\beta 2}$		$K_{\beta 3}$		K	Total K-
Element	Energy	Yield	Energy	Yield	Energy	Yield	Energy	Yield	Energy	Yield	Edge	Shell Yield
Cd	23.174	46.1	22.984	24.5	26.095	7.69	26.644	1.98	26.060	3.99	26.711	84.3
Zn	8.639	28.0	8.616	14.3	9.572	3.30			9.572	1.74	9.659	47.4
Te	27.472	46.2	27.202	25.0	30.995	8.21	31.704	2.37	30.944	4.26	31.813	87.7
Hg	70.818	46.3	68.894	27.5	80.255	10.70	82.473	3.87	79.824	5.59	83.103	96.5
I	28.612	46.4	28.317	25.2	32.295	8.34	33.047	2.47	32.239	4.32	33.169	88.4

2.1.2 Compton Scattering

Segmented detectors naturally have the ability to sense Compton scatter interactions. Knowledge of the energy and position of interaction locations enables Compton imaging. Between roughly 400 keV and 5 MeV Compton scattering is the dominant interaction in CZT and HgI_2. When a photon scatters off an unbound electron, a fraction of the photon's energy is transferred to that electron. If the photon scattering angle is ϕ and the recoil electron is emitted at angle θ, then the energy ($h\nu'$) of the scattered photon is related to the initial photon energy ($h\nu$) by

$$h\nu' = \frac{h\nu}{1 + \frac{h\nu}{m_o c^2}(1 - cos\theta)}, \tag{2.1}$$

where $m_o c^2$ is the rest mass of the electron. The angular distribution of a scattered gamma ray can be estimated using the Klein-Nishina formula.

2.1.3 Pair Production

At energies above 1.02 MeV, pair production is possible. During pair production, the incident photon is absorbed in the coulomb field of the nucleus. The result of the interaction is an electron-positron pair. The kinetic energy shared by the electron

and positron is equal to the difference between the initial photon energy and the total rest mass of the electron and positron. At relatively low energies, it is most likely that the electron and positron share the remaining kinetic energy equally. Theoretical distributions of the fraction of energy of each particle can be found in Ref. [14] page 704. Annihilation occurs after the positron loses its kinetic energy and annihilates with an electron. As a result, two 511 keV photons are released in opposite directions satisfying conservation of momentum.

2.2 Signal Generation Physics

The goal of this section is to describe how energy-proportional signals are generated in pixelated CZT and HgI_2 detectors. After an interaction occurs, the energy of the secondary radiation must be completely absorbed in the detector in order to obtain a signal proportional to the original incident photon energy. Following photoelectric absorption, the energy of photoelectrons, characteristic x-rays, and Auger electrons must be deposited. After Compton scatter, the energy of the recoil electron, the scattered photon, and subsequent Compton scatter and photoelectric absorption energies must all be deposited. The total energy of a pair production interaction is deposited when the kinetic energy of the electron-positron pair and the energy from the interaction histories of the two 511 keV annihilation photons are all deposited in the detector.

If a detector is small relative to the range of the secondary photons and/or electrons, the detector may not absorb all the energy of the incident photon. Large detectors are more likely to capture all the energy of primary and secondary particles. In either case, the signal measured is proportional to the energy deposited in the detector by the secondary radiation. In semiconductor detectors, the desired

final result of all of this energy loss is the generation of charge carriers that can provide an electronic signal proportional to the energy deposition. This section is divided into subsections describing three components of signal formation: charge cloud generation, charge carrier transport, and charge induction in pixelated detectors.

2.2.1 Charge Cloud Generation

As secondary electrons or positrons lose energy, the atoms they encounter ionize if enough energy is transferred to raise an electron from the valence band to the conduction band. As shown in table 1.1, this bandgap is relatively high in CZT and HgI_2, 1.64 and 2.13 eV respectively. A wide bandgap is preferable for room temperature detector operation to minimize thermally generated electron-hole pairs. The actual number of atoms ionized can be estimated using an experimentally determined quantity known as the ionization energy. This value represents the experimentally measured average energy required to generate an electron-hole pair in a specific material. A typical 662 keV full energy deposition in CZT would generate approximately 132,000 electron-hole pairs.

The initial distribution of a charge cloud is determined by the path of the ionizing electron or positron that resulted from the photon interaction. This distribution has been studied through simulation for the CZT detectors used in this study. The mean diameter, defined as the difference between the maximum lateral cloud dimension, of an electron cloud was measured to be 220 μm at 662 keV, roughly 500 μm at 1.3 MeV, and 1.3 mm at 2.6 MeV [63]. Based on the simulation results, a first order approximation for the relationship between cloud diameter and energy deposition can be estimated using a linear function. Once created, charge carriers experience the effect of diffusion due to random thermal motion of the individual particles. For a given carrier mobility μ and temperature, T, the diffusion coefficient D in m^2/s

can be calculated using the Einstein relation:

$$D = \mu \frac{k_B T}{q}, \tag{2.2}$$

where k_B is the Boltzmann constant, and q is the charge of the carrier. The standard deviation of the Gaussian-shaped charge carrier distribution is given by

$$\sigma = \sqrt{2Dt}, \tag{2.3}$$

where t is the time elapsed. When a detector is operational, t is equivalent to the distance the charge travels in the detector (x) divided by the velocity of the charge (v). The consequence of diffusion is a broadening of the charge cloud over time (i.e. distance) as charge is transported through the detection medium.

2.2.2 Charge Carrier Transport

In order to collect charge carriers generated by radiation interactions, they must be transported through the semiconductor material by application of an electric field. There are three general factors that affect charge carriers during the charge transport process: diffusion, trapping, and recombination. Table 2.2 lists a number of useful parameters related to charge transport in CZT and HgI_2. The mobility of the charge carriers (μ) is a measure of how fast charge moves through a material. Mobility determines how rapidly a signal pulses will disseminate in a detector of various sizes. The mobility-lifetime product $\mu\tau$ determines what fraction of charges can be collected at a given bias voltage.

Table 2.2: Charge Transport Properties of CZT and HgI_2 [57]

Material	μ_e cm^2/Vs	μ_h cm^2/Vs	$(\mu\tau)_e$ cm^2/V	$(\mu\tau)_h$ cm^2/V
CZT	1000	120	$4{\cdot}10^{-3}$	$1.2{\cdot}10^{-4}$
HgI_2	100	4	$3{\cdot}10^{-4}$	$4{\cdot}10^{-5}$

The drift velocity of a charge cloud can be defined as the product of charge mobility μ and the electric field E,

$$v = \mu E. \tag{2.4}$$

The electric field is equal to the bias voltage applied to the planar cathode divided by the thickness of the detector. Using the values in table 2.2, the velocity of electrons and holes can be calculated in CZT and HgI_2 at a given electric field. The amount of diffusion a charge cloud experiences depends on the velocity of the electrons and holes and the distance the cloud travels. Incorporating Eq. 2.2 with 2.3, the standard deviation of charge carrier diffusion can be expressed using only constants[1], experimental variables, or measureable quantities:

$$\sigma = d\sqrt{\frac{2k_B T F_d}{qV}}, \tag{2.5}$$

where d is the thickness of the detector and F_d is the fraction of the detector thickness the charge carriers travel. For CZT, assuming 20°C, 15 mm detector thickness, and a cathode bias of -3000V, the standard deviation (in μm) as a function of relative transport distance would be described as roughly

$$\sigma(F_d) = 62\sqrt{F_d}, \tag{2.6}$$

where F_d is a number between 0 and 1. The standard deviation of a distribution for a charge cloud that has traveled the full thickness of the detector would be approximately 62 μm (145 μm FWHM). In the case of the 11 mm thick HgI_2 detectors studied, the standard deviation would be

$$\sigma(F_d) = 45\sqrt{F_d}. \tag{2.7}$$

[1] at 20°C, kT/q = 0.0253V

Diffusion alters the spatial distribution of the charge cloud; however, the primary effect of trapping and recombination is a decrease in the number of charge carriers. Impurities in the detector material are the most common source of trapping sites and recombination centers. Their net effect is a reduction in the average charge carrier lifetime. Trapping can have a significant effect on the energy resolution of thick semiconductor detectors. Assuming a constant electric field, charge carriers created at different depths are transported through varying lengths of detector material. Charge clouds that travel greater lengths lose more charge than clouds that travel short distances. The result is a broadening of the detector energy response to a monoenergetic source. This effect can be corrected if the depth of interaction and charge deficit is known. Details of how interaction depth is calculated in pixelated CZT and HgI_2 detectors are provided in chapter V. Further details concerning recombination and trapping mechanisms in CZT and HgI_2 can be found in reference [53], pages 195-201 and reference [57] pages 459-468.

Comparing the electron and hole transport properties in table 2.2, the mobility and lifetime products of holes are roughly an order of magnitude lower than that of electrons. In thick detectors, it is often impractical to measure the charge induction contribution of the slowly moving holes. As explained in section 1.3.1, single-polarity charge sensing techniques can be used to improve the spectroscopic performance of materials with significantly different charge mobilities. One of the single-polarity techniques is the small pixel effect. The next subsection describes the details of charge induction in pixelated detectors.

2.2.3 Charge Induction in Pixelated Detectors

As electrons move through a pixelated semiconductor detector, charge is induced on all of the detector's electrodes. The amount of charge induced on an electrode

can be calculated using the Shockley-Ramo theorem [56, 51]. The theorem is applied to pixelated semiconductor detectors in Ref. [23]. The induced charge Q on an electrode by a charge q at an instantaneous position $\mathbf{x}$ is given by

$$Q = -q\psi_o(\mathbf{x}). \tag{2.8}$$

In this equation, $\psi_o(\mathbf{x})$ is the weighting potential at position $\mathbf{x}$. The current i on the electrode is the product of the instantaneous velocity ($\mathbf{v}$) of the charge and the weighting field $\mathbf{E}_o(\mathbf{x})$ at position $\mathbf{x}$:

$$i = q\mathbf{v} \cdot \mathbf{E_o}(\mathbf{x}) \tag{2.9}$$

using the following boundary conditions: the potential of the electrode to be calculated is set to 1, the potential of the remaining electrodes is set to 0, and no space charge is present. For a specific electrode geometry, $\psi_o(\mathbf{x})$ and $\mathbf{E}_o(\mathbf{x})$ can be calculated using the Laplace equation. The electric field determines the velocity of the charge carriers; however, it is important to note that $\psi_o(\mathbf{x})$ is independent of the operating field. $\psi_o(\mathbf{x})$ is solely a function of the electrode geometry. The task of calculating $\psi_o(\mathbf{x})$ for the complex case of a pixelated detector is accomplished using Ansoft Maxwell field simulation software[2].

Figure 2.2 is a schematic drawing showing the anode surface of a pixelated detector modeled using the Maxwell software. Figure 2.3 shows the result of the calculation. The weighting potential, $\psi_o(\mathbf{x})$ is calculated for the cathode, collecting anode pixel, and two non-collecting neighbor anode pixels. The weighting potential of the collecting pixel is shown in red. The weighting potential of the pixel is zero on the cathode side (0 mm) and slowly increases across the thickness of the detector until it rises rapidly near the anode region. Using these results in equation 2.8, it can be seen that little charge is induced on an anode pixel until the charge is in the vicinity of the

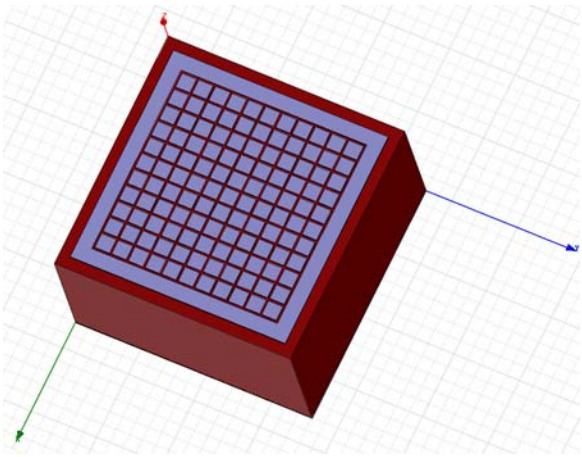

Figure 2.2: A schematic of the pixelated anode design for a HgI_2 detector used in the Maxwell model. The detector has 121 anode pixels surrounded by a guard ring. The cathode is planar.

anode. The green line shows the weighting potential of a pixel located on the edge of a collecting pixel. The blue line is a corner pixel. Since these neighbor pixels do not collect charge, their final weighting potential is zero. The weighting potential for the planar cathode is shown in black. The final weighting potential for the cathode is also zero. Interactions that occur near the cathode induce a larger amount of charge than interactions that occur near the anode. The contrast in weighting potential of the cathode and pixel is a demonstration of the small pixel effect as described in reference [4]. This is also the basis for 3-D depth sensing.

2.3 Detector System Model

Simulation tools that incorporate the physics discussed in section 2.2 are used to design and test event classification algorithms. As mentioned in chapter I, the event classification algorithms in this thesis rely on measurements of pulse waveforms from multiple electrodes to determine the interaction history of a photon in a pixelated detector. The goal of this section is to describe how pulse waveforms are simulated for various interactions. Further details of the simulation software used in this thesis

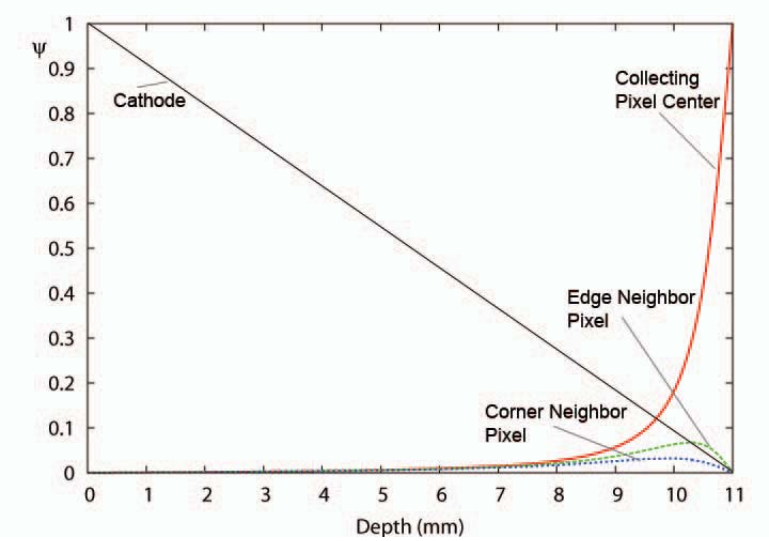

Figure 2.3: Multiple weighting potentials are shown as a function of depth for the cathode, the collecting pixel, a cardinal neighbor pixel, and a corner pixel. The detector modeled in this simulation is 11 mm thick pixelated HgI_2.

study can be found in references [30, 31, 32]. Also included in these references are validity tests that compare the simulation response to experimental results.

Figure 2.4 shows a view of the simulation software output. From the simulation interface, a user can enter a desired interaction history and view or save the calculated pulse waveform response. There are two options for generating events. First, the user can generate individual histories by entering positions and energies for the interaction locations of an event. Another input method is to open an interaction history file from a GEANT4 [9] simulation. Figure 2.4 shows the interaction location and energy deposition distribution for a 662 keV full energy deposition located in the center of a pixel at a depth near the middle of the detector. The anode configuration of this particular example is a simple pixel design which does not use a charge steering grid.

The pulse waveforms for the collecting pixel as well as its neighbor pixels are calculated with knowledge of the charge transport and induction physics described in section 2.2. The charge Q induced on an anode pixel from drifting electrons and

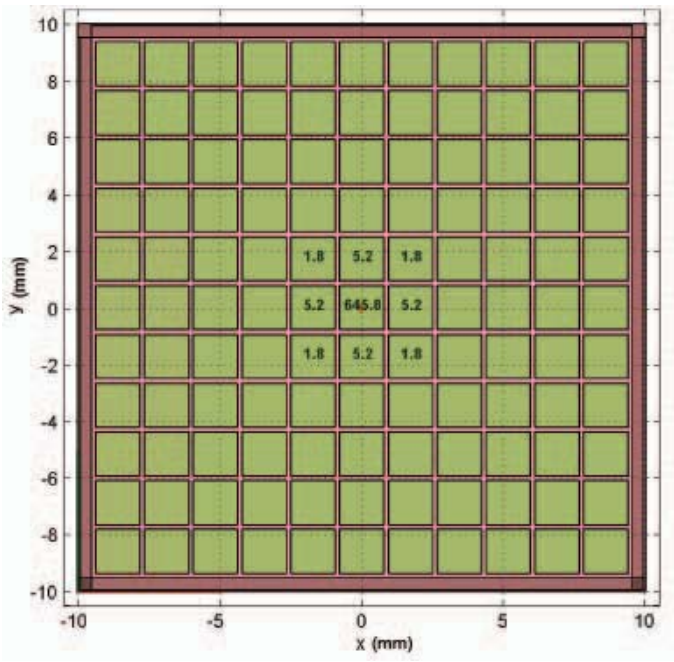

Figure 2.4: Simulation results for a 662 keV interaction in the center of a pixel. The anode design in this simulation is simple pixel; there is no common steering grid.

holes is given by

$$Q = -nq[\psi(\mathbf{x_f}) - \psi(\mathbf{x_i})] \tag{2.10}$$

where n is the number of electrons or holes, q is the charge, ψ is the pixel weighting potential function, and $\mathbf{x}_f$ and $\mathbf{x}_i$ are the final and initial position of the charge cloud with respect to the pixel anode. In the example of figure 2.4, the initial position is the center of the pixel at a depth of 10 mm (spatial coordinates: x=0.0, y=0.0, z=10.0). The final position is determined by the path of the calculated electric field. In this case, the final position would be the center of the pixel at a depth corresponding to the surface of the pixel (x=0.0, y=0.0, z=15.0). The total charge Q_C induced on a collecting pixel after collection due to electrons is

$$Q_C = -ne[1 - \psi(\mathbf{x}_i)] \tag{2.11}$$

because the weighting potential at $\mathbf{x}_f$ for a collecting pixel is 1. The value of the weighting potential at position $\mathbf{x}_i$ is calculated using the method described in section

2.2.3. The value of Q_C can then be calculated as a function of the detector depth. In this simulation, the total charge ne is normalized to the value of the energy deposited. Due to the small pixel effect, $\psi(\mathbf{x}_i)$ is nearly zero except near the anode surface, where the ratio of pixel size to depth (the relative distance from the anode) is closer to one. Holes also induce charge on all the electrodes. However, due to their low mobility in CZT and HgI_2, holes do not induce a large amount of charge in the time-scale of interest.

Figure 2.5 shows a series of simulation results illustrating the effect of the weighting potential on the signal amplitude. In this example, GEANT4 is used to simulate the interaction histories of a 662 keV Cs-137 source. Gaussian noise equivalent to 1.0% FWHM at 662 keV was added to the energy response. The plot on the top left shows the simulated energy spectrum in the detector as a function of interaction depth without the effect of weighting potential or charge trapping. Here, the photopeak energy does not change across the range of depths. The plot on the top right shows the exact same simulated energy deposition data set, but includes the weighting potential effect. Trapping is not included in this example. The maximum amount of charge induced on the anode from electrons occurs when the interaction occurs nearest to the cathode (depth = 0 mm). The minimum amount of charge is induced for electrons when the interaction occurs nearest to the anode (depth = 11 mm). The lower sub-figure in Fig. 2.5 shows how the weighting potential affects the photopeak energy response. Near the anode, the weighting potential changes dramatically. If an interaction occurs near the anode, its $\Delta\psi$ as formalized in Eq. 2.10 is small, resulting in a small induced charge. If the interaction occurs near the cathode, $\Delta\psi$ is maximized resulting in a maximum induced charge.

The weighting potential of neighbor pixels is the same as that of the collecting

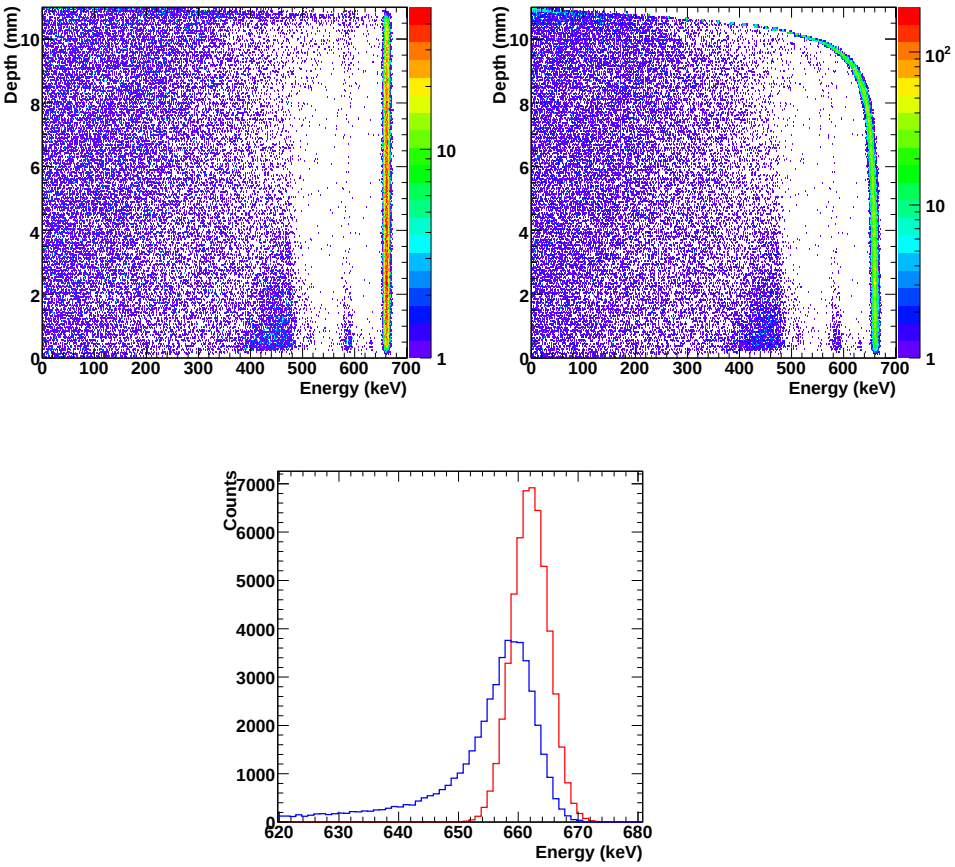

Figure 2.5: Simulation results from a 662 keV gamma-ray source interactions in a single anode pixel of an 11 mm thick HgI_2 detector. The top left figure shows the energy response vs. depth without including the effect of weighting potential or charge trapping. The same interaction series is shown in the top right, however the effect of weighting potential is included. The bottom plot compares the depth-separated photopeak spectrum summed across all depths for the two cases. Data not containing weighting potential information are shown in red. Data without weighting potential calibrations are shown in blue. Calibrations can be applied to normalize the effect of the measured charge induction across the depth of a detector to minimize the effect of weighting potential in a pixelated detector.

pixel until the charge enters the anode region and is collected. While charge is moving within the bulk of the detector, the maximum charge Q_N induced on a non-collecting pixel by electrons is the same as Eq. 2.10,

$$Q_N = -ne[\psi(\mathbf{x_f}) - \psi(\mathbf{x_i})]. \tag{2.12}$$

In this case, $\psi(\mathbf{x}_f)$ is 0 since the neighbor pixel does not collect charge. In Fig. 2.3, there are depths near the anode where the difference between an instantaneous and initial weighting potential is a positive value. Even if the initial and final weighting potential values are zero, there is still a depth range near the anode where positive charge is induced on a neighbor pixel.

These effects can be seen in the simulated waveforms of Fig. 2.6. This figure also includes a detector diagram to indicate the simulated interaction position. In these waveforms, the signal amplitude is normalized to equivalent energy in keV. The signal is converted to a function of time using knowledge of the physical detector thickness, the applied cathode bias, and the mobility of the charge carriers in CZT. The number of charge carriers can also be modified as a function of drift length using a trapping model. The $(\mu\tau)_e$ and $(\mu\tau)_h$ used in this simulation are 3.00×10^{-2} and 1.5×10^{-4} cm^2/V respectively. The blue positive slope waveform in Fig. 2.6 with an amplitude of nearly 662 keV is the simulated preamplifier pulse of the central collecting pixel. The red linear negative slope waveform with an amplitude of roughly -250 keV is the cathode signal. The amplitude of the cathode signal is smaller than the amplitude of the pixel because the signal induced on the planar cathode is not subject to the small pixel effect. The cathode signal also contains a measurable amount of charge due to hole movement between $t = 0.25$ and 1.0 μs. The slope of this hole induction component is smaller than the slope of the electron induction because holes move slower than electrons in CZT. Holes do not contribute to the pixel signal in this

region because the weighting potential difference is small.

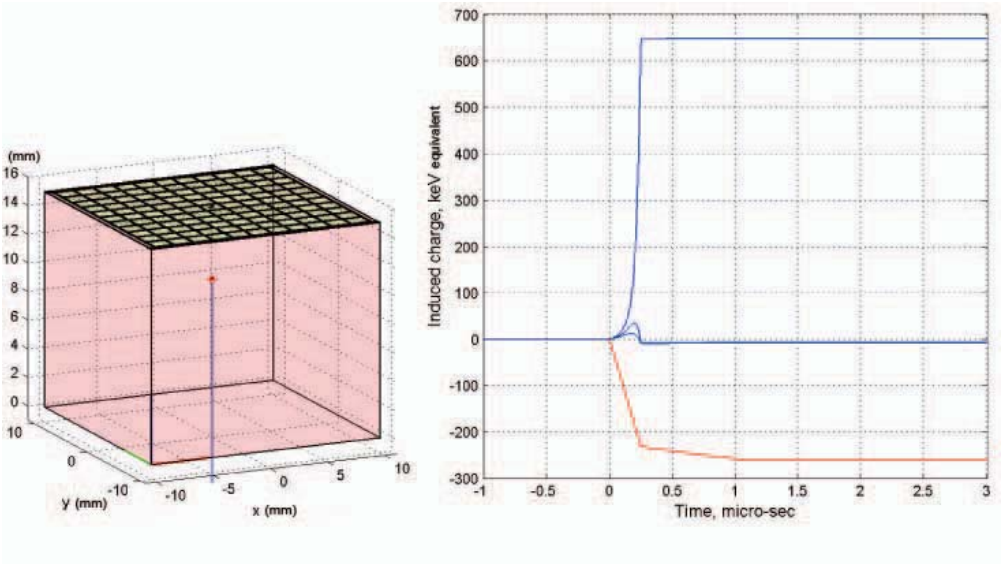

Figure 2.6: Left: A simulated 662 keV single-interaction at depth 10 mm, in the center of a single pixel. Right: Simulated pulse waveforms have been calculated for the cathode, center pixel, and neighboring pixels.

The small, slightly negative amplitude pulses in Fig.2.6 (blue) are from the eight neighbor pixels. In this example, most of the neighbor signals overlap due to symmetry in relation to the interaction location. The signals of all four corner neighbor pixels are identical as are the four edge neighbor pixels. There is a small positive amplitude "bump" in the neighbor pixel waveforms. The neighbor waveform amplitude starts at zero. The signal then rises as the electron cloud passes near the non-collecting neighbor pixel. This is the region where the maximum weighting potential difference occurs. The response in the neighbor pixel in this region is a short "transient peak." When the electron cloud is collected in the center pixel, the charge induced on the neighbor pixels returns to zero. In this example, the signal falls to a level slightly below zero. This region of the waveform will be referred to hereafter as the "negative tail".

Using the calculated weighting potential for a non-collecting pixel (an example is

found in Fig. 2.3) the weighting potential model in Eq. 2.12 can be used to calculate the charge induced on a non-collecting pixel. For an interaction near the anode, $\psi(\mathbf{x}_i)$ is greater than zero and $\psi(\mathbf{x}_f)$ is zero resulting in a negative value for Q_N when the electron cloud is collected. If the interaction occurs very near the cathode surface, both $\psi(\mathbf{x}_i)$ and $\psi(\mathbf{x}_f)$ are equal to zero, so the final induced charge will be zero. Another way to understand this effect is to remember the presence of holes at position $\mathbf{x}_i$. During the motion of the electrons, the holes are effectively "trapped" at position $\mathbf{x}_i$. When the electrons are collected, the final charge induced on the neighbor (and in fact the collecting pixel) is reduced by the difference in weighting potential due to the holes at position $\mathbf{x}_i$.

Figure 2.7 shows another view of the same event. In this display, 3 keV equivalent FWHM Gaussian noise has been added to the waveform. Also calculated are various shaped signals including a fast shaping filter designed to measure timing features and a slow shaper to measure pulse amplitude. All of the waveforms can be saved for later analysis. This technique is used to design and test the event classification algorithms developed in this study.

Before exploring how simulated waveforms can help define waveform-based event signatures for event classification, it is useful to study a few more simulation examples. Figure 2.8 helps understand how charge sharing is modeled. An accurate charge sharing model requires an accurate representation of the electron cloud. In this version of the software, the electron cloud is modeled as a two dimensional circular surface in the lateral plane of the electrodes.

The size of the electron cloud and the effect of diffusion are based on the simulation and calculations described in section 2.2.1. The anode schematic (lower left corner of Fig. 2.8) illustrates the charge cloud model. In this example, it is clear how charge

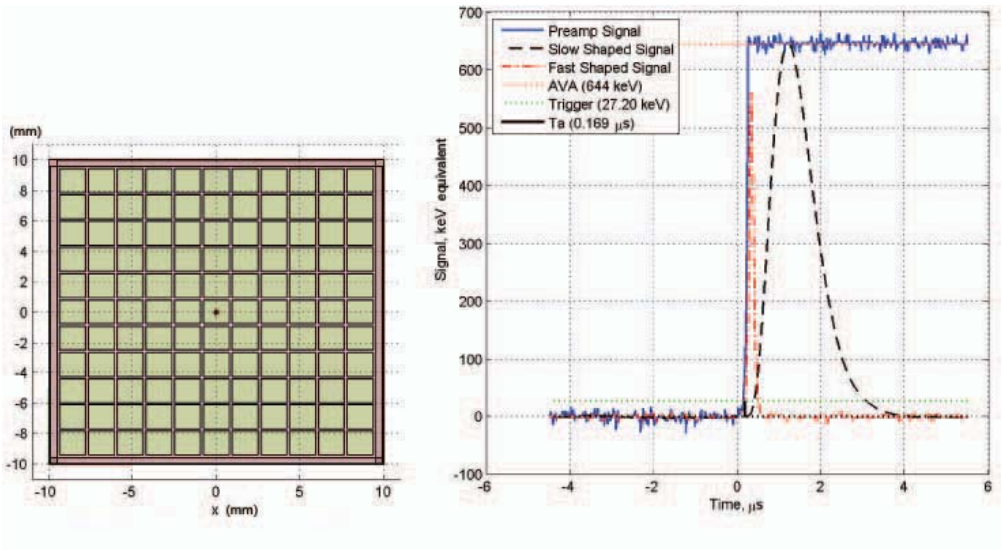

Figure 2.7: Left: A simulated 662 keV single-interaction at depth 10 mm, in the center of a single pixel. Right: Noise, as well as shaped signals can be calculated for the pulse waveforms.

is shared between two pixels. The corresponding waveforms are shown to the right. Figure 2.9 shows the same situation but charge is shared between four neighboring pixels.

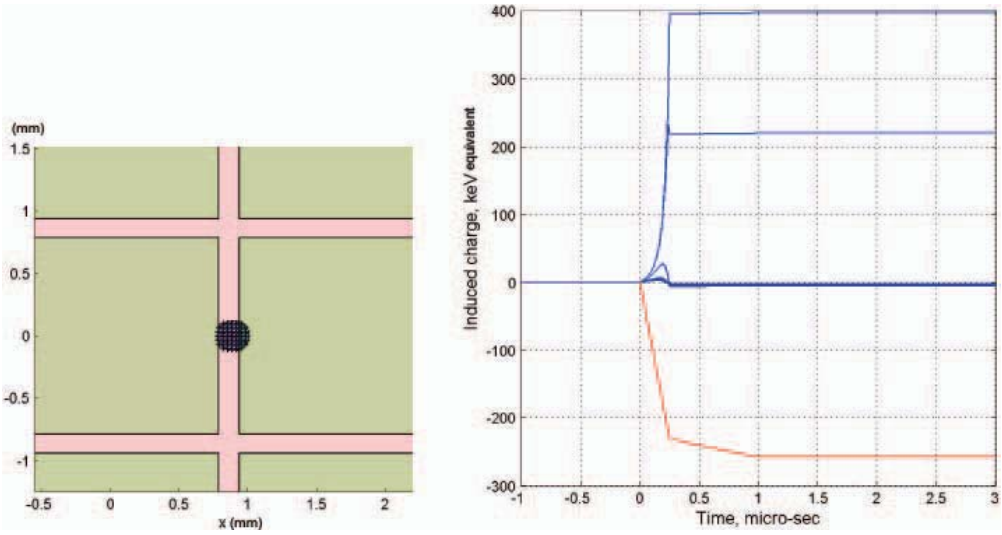

Figure 2.8: Left: A simulated 662 keV single-interaction at depth 10 mm, in the gap between two pixels. Right: The pulse waveforms demonstrate the effect of charge sharing. Two neighboring pixels collect charge from a single photon interaction.

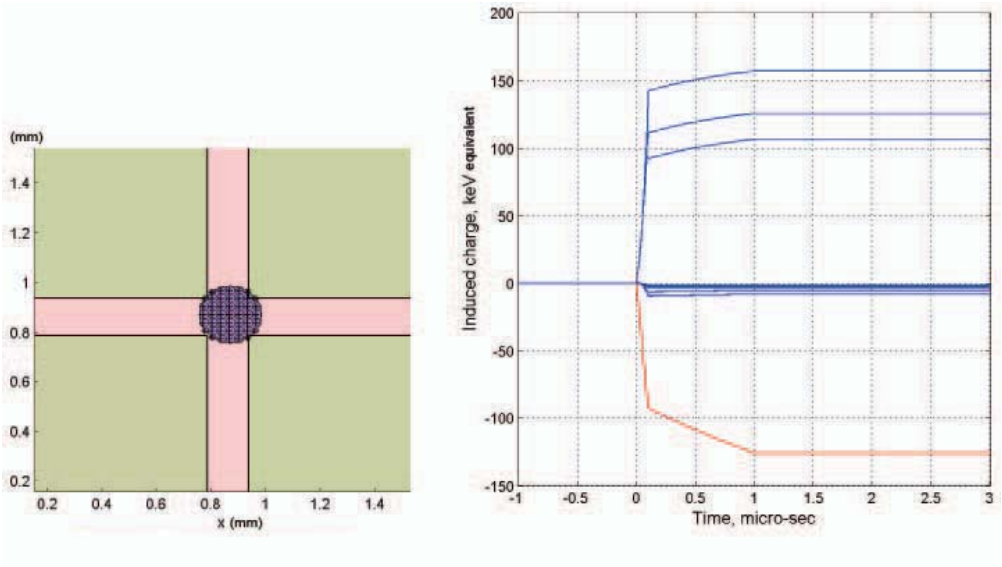

Figure 2.9: Left: A simulated 662 keV single-interaction at depth 13 mm, in the gap between four pixels. Right: The pulse waveforms demonstrate the effect of charge sharing in four neighboring pixels. The effect of charge induction due to holes can be seen on both cathode and pixel waveforms.

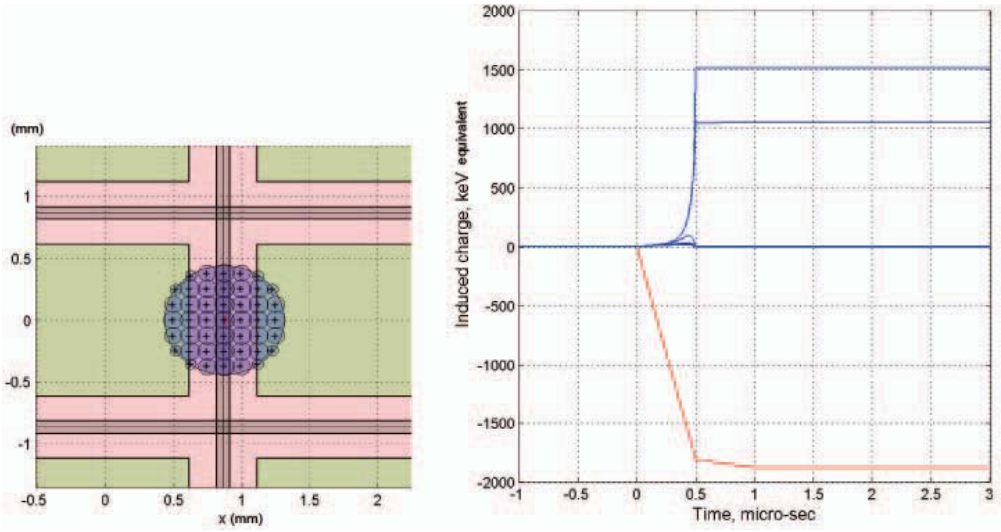

Figure 2.10: Left: A simulated 2.614 MeV single-interaction at depth 5 mm, in the gap between two pixels. In this example a steering grid is also modeled. Right: The pulse waveforms from the event simulated in the figure to the left.

Figure 2.10 shows a charge cloud resulting from a 2.614 MeV energy deposition. As explained in section 2.1, simulated electron cloud size is assumed to vary linearly with respect to energy. Here, the charge cloud is noticeably larger than in Fig. 2.8 resulting in a higher degree of charge sharing. Figure 2.10 also demonstrates the use of a common anode grid. This can be seen in the anode schematic in the lower left corner. This inter-pixel grid is biased at a negative potential (here, -100V) to steer electrons away from the gap toward pixels. This technique improves charge collection for events occurring below or near the gap [68]. The addition of a steering grid requires a more advanced electric field model. Electrons can then move laterally with respect to the electrode plane as the cloud drifts through the detector. The weighting potential is calculated along this track.

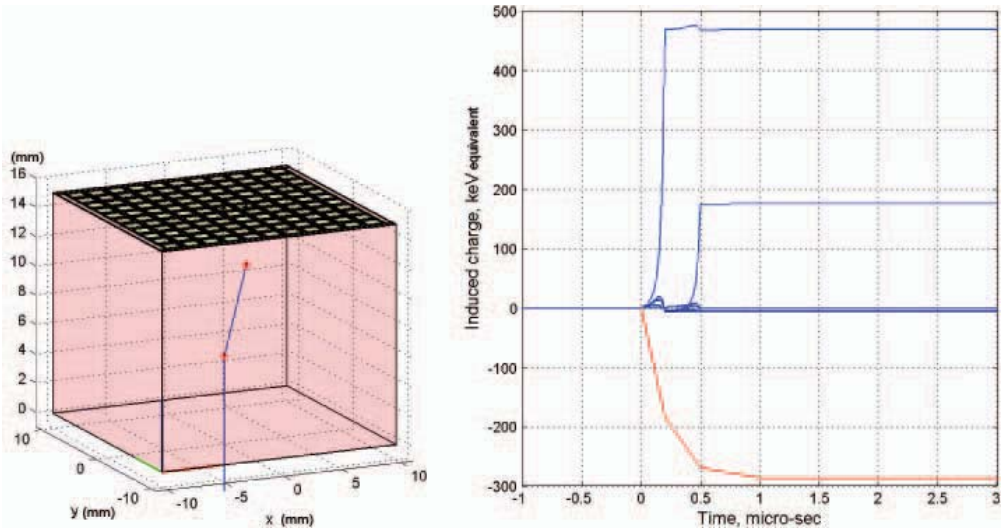

Figure 2.11: Left: A simulated 662 keV Compton scatter event. In this illustration, the scatter occurs at depth 11 in one pixel, and the final photoelectric absorption occurs at depth 5 in a neighbor pixel. Right: The pulse waveforms demonstrate the effect of two separate charge clouds interacting at two different depths.

As seen in Fig. 2.11 shows that the simulation is not limited to a one-interaction event history. In this example, a Compton scatter event is modeled. The diagram in the lower left is a cross section across the detector depths and shows two interaction positions. The pulse waveform response is seen on the right. As expected, there are two pixels that collect charge. The pulses are separated by a time proportional to the difference in depth between the two interactions. Since these interactions occur in neighboring pixels, the charge moving in the neighbor pixel can be seen in the signal of the other pixel. As the cloud in the neighbor pixel volume gets close to the other pixel, it induces charge on the other pixel. When the cloud is collected by the neighbor pixel, the signal falls in the other pixel as shown at t = 0.5 μs in Fig.2.11. Non-collecting neighbor pixels also contain features of the two interactions that can be seen in the transient signals located between $t = 0$ and 0.5 μs.

2.4 Waveform Signatures

Section 2.3 introduced how pulse waveforms of different interactions can be simulated. The goal of this section is to understand how these waveforms will be used to develop event classification algorithms. A unique signature can be identified for each type of interaction. These signatures are a combination of the interaction physics as well as the detector response to those interactions. The preceding sections discussed these two components in detail. The remaining chapters will describe how this task is accomplished using experimental data.

The following subsections introduce classification signatures for the most common photon interactions. A signature is based on a "waveform set." A waveform set is defined as the series of pulse waveforms from a specific detector available to characterize a single event history. The waveforms that are assigned to a set include the cathode signal, the signals from pixels that collect charge, and the signals of pixels that neighbor collecting pixels. If one pixel collects charge, the recorded pulse waveforms of the cathode and 9 pixels compose the set. If two pixels collect charge the cathode signal plus as many as 18 pixel waveforms compose the set. A waveform set is an extremely rich source of information for a single detector event.

2.4.1 Photoelectric Absorption Signatures

Figure 2.12 shows an illustration of a typical single-pixel 662 keV photoelectric absorption event in a pixelated semiconductor detector. The figure also includes the simulated waveform responses (without noise) of the collecting pixel, side-neighbor pixel, and the cathode. During a photoelectric absorption interaction, the incident photon transfers all of its energy to a bound atomic electron in the detector material. An electron cloud is formed as the resulting photoelectron loses energy, ionizing atoms

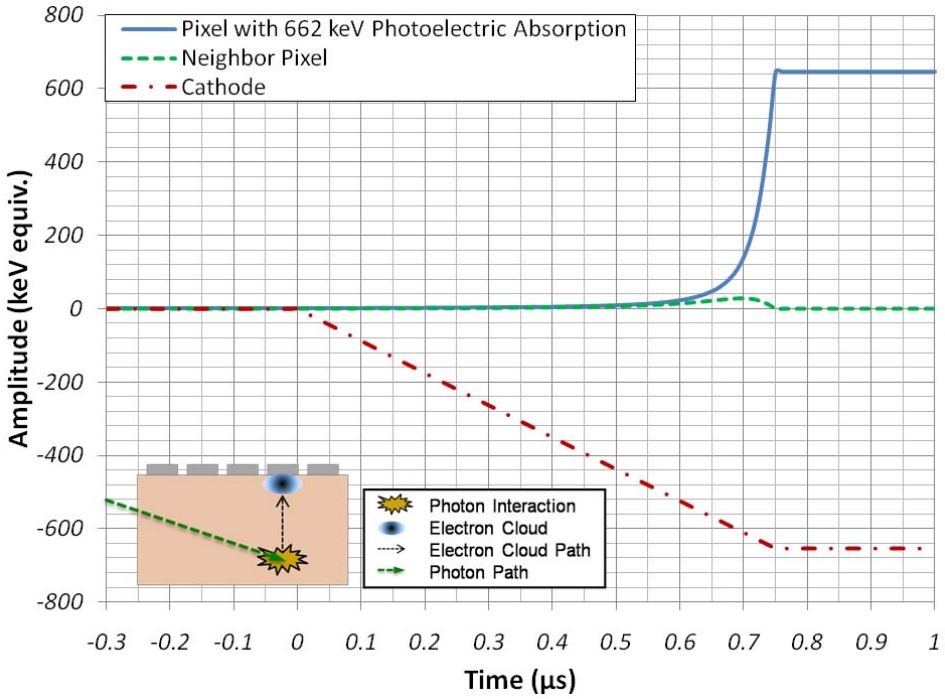

Figure 2.12: A simulated single pixel photoelectric absorption event in a 3-D CZT detector.

along its path. This electron cloud is transported through the semiconductor along electric field lines toward an anode pixel. As the electrons move, they induce signals on all the electrodes. The magnitude of induction depends on the amount of charge created and the weighting potential along the charge transport track.

This particular interaction occurs on the cathode side of the detector in the center of a single pixel column. The signals in Fig. 2.12 are formed as the electron cloud moves toward the anode. Three different electrode signals are plotted. The cathode signal has a linear slope which corresponds to the linear weighting potential of the planar cathode. The rise time of the cathode represents the electron charge drift time in the detector. The non-linear shape of the collecting anode pixel is due to the weighting potential of a single collecting pixel. A substantial amount of charge is not induced on the pixel until the electron cloud gets near the anode. Because the interaction occurs in the exact center of the pixel, the waveforms of the four edge

neighbor pixels and four corner neighbor pixels are identical. A small transient peak is evident in the neighbor pixels. The transient peak of the corner neighbor pixels would have a smaller amplitude than the transient peak of the corner pixels.

If the energy of the incident photon is not known, it is difficult to have a confirming signature of photoelectric absorption. A single interaction in a pixel may be a Compton scatter out of the detector. One signature of a photoelectric absorption event is the emission of a characteristic X-ray which can be emitted as the atom returns to its ground state. As described in section 2.1.1, the energy of the characteristic X-ray depends on which orbital shell the photoelectron originated from as well as the elements that make up the detector crystal. Table 2.1 lists the K_α and K_β energies for the elements that make up the detectors used in this study. Interactions with bound electrons in other shells are possible; however, they are less likely and yield lower energy X-rays. Higher energy X-rays are of primary interest in this study because they have a higher probability of escaping the original interaction voxel. If this X-ray energy can be detected, the interaction can be classified as a photoelectric absorption interaction. This technique can be used to eliminate Compton continuum events in a spectrum and improves Compton sequence estimates for imaging applications by confirming the final interaction position.

A photoelectric absorption event signature requires detection of a characteristic X-ray. This is accomplished by detecting a pulse with a measured amplitude corresponding to an expected X-ray energy. If this X-ray is absorbed very close to the site of the photoelectric absorption, it cannot be distinguished from the original energy deposition and the signature is lost. This is also the case of Auger electron emission. If the X-ray is absorbed at a different depth in the same pixel as the photoelectric absorption site, then the X-ray can be distinguished based on an accurate measure-

ment of the X-ray signal. If the X-ray is absorbed in a neighbor pixel, the amplitude of that pixel signal can be measured and compared with expected X-ray energies.

Even if a characteristic X-ray energy is measured, there is a chance that the event is actually a Compton scatter. To quantify this possibility, calculations can be made to assign a likelihood that the event is either a photoelectric absorption or a Compton scatter. This likelihood is a function of the measured energies and the interaction locations. If the position of the source is known, the incident direction of the interacting photons provides even greater accuracy in assigning a likelihood. Probabilities for potential Compton sequences can be calculated using the Compton edge test via the Compton scatter equation as well as the Klein-Nishina formula. Details of Compton sequence reconstruction methods for the detectors used in this study can be found in reference [62].

2.4.2 Compton Scattering Signatures

During a Compton scatter interaction, a photon scatters off a free atomic electron. An electron cloud is formed as the recoil electron ionizes atoms as it loses energy. Subsequent Compton scatters or photoelectric absorption interactions may follow. When more than one interaction occurs at different depths, the resulting electron clouds are collected by a pixel at different times. Figure 2.13 demonstrates a Compton scatter within a single pixel. Detection of non-coincident pixel pulses resulting from interactions at different depths provides a signature of Compton scatter events. If one of these non-coincident pulse energies corresponds to a characteristic X-ray energy, then it is possible that the interaction is a characteristic X-ray escape into a different detector voxel. Detection of a Compton scatter as well as a characteristic X-ray is evidence of a complete scatter-absorption sequence in a detector. Compton scatter into a neighbor pixel is shown in Fig. 2.14. Compton scatter into a non-

neighbor pixel is similar, except the charge induced on each pixel from the other interaction would be less due to the greater distance between the interactions.

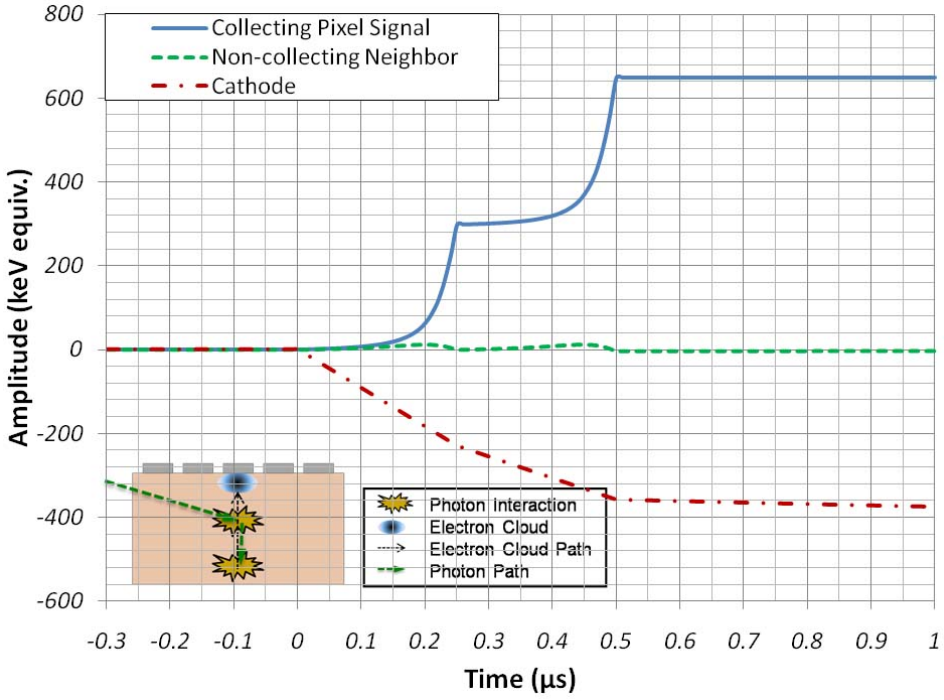

Figure 2.13: A Compton scatter interaction in a single pixel. The energy deposited distinguishes a Compton scatter from a characteristic X-ray.

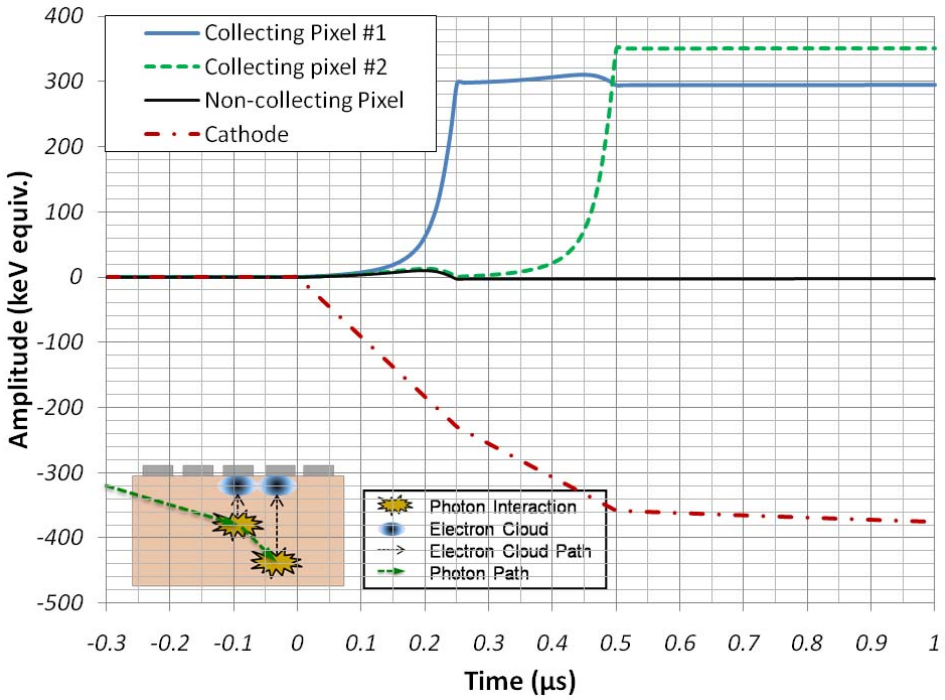

Figure 2.14: A Compton scatter to an interaction at a different depth in a neighbor pixel. This results in a measurable time difference between rise times

2.4.3 Pair Production Signatures

Above 1.022 MeV, photons that interact with a nucleus can create an electron and positron which share the kinetic energy remaining after production of the pair. When the positron annihilates, two 511 keV photons are created. Detection of a 511 keV photon and a second charge cloud from the kinetic energy lost by the electron and positron provide a signature of pair production. The waveform signature would be similar to Fig. 2.13 or Fig. 2.14 except at least one energy response would be 511 keV. If both annihilation photons are detected, the position of the interaction locations of the annihilation photons relative to the position of the initial electron/positron energy deposition site provide a further degree of confidence. During the annihilation process, the two 511 keV photons are emitted in opposite directions. Assuming that the positron annihilates near the initial charge cloud (formed from the energy loss of the original pair), and both annihilation photons interact in the detector, the three interaction locations will lie on the same line in the detector's 3-D space.

If an electron cloud follows electric field lines near the gap between pixels, fractions of the electron cloud can be shared between pixels. This phenomenon depends on the pixel dimensions, spacing, and presence of a steering grid. The likelihood of charge sharing increases with cloud size (energy). Figure 2.15 demonstrates how a single electron cloud can result in a multiple pixel event. As the electron cloud moves toward the anode, a fraction of the cloud is collected by two different pixels. In this waveform set, it is evident that charge is collected in two pixels. The non-collecting opposite neighbor signal also includes a smaller transient signal formed by charge induction from the electron cloud fraction collected by the center pixel.

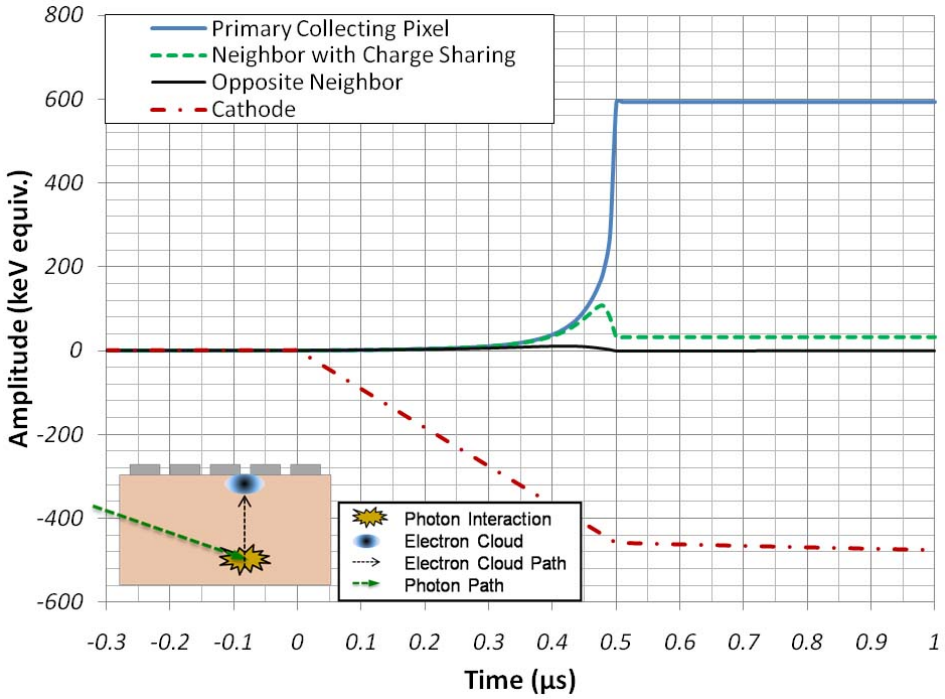

Figure 2.15: A waveform response to a simulated charge sharing event between the Center and North pixels.

2.4.4 System-Response Signatures

A transient signal is not seen in the center pixel because as detailed in section 2.3, the induction of a large amount of charge in the center pixel signal washes-out the relatively small transient signal coming from the charge collected in the neighbor pixel. From the perspective of the neighbor pixel, the large amount of charge collected in the center pixel induces a large transient signal on the neighbor. Events that approach this turning point can be seen in the collecting neighbor pixels in Figs. 2.16 and 2.17. In both figures, the transient signal due to charge in the central pixel can be seen in the neighbor. However, if the event occurred slightly closer to the neighbor pixel, no transient could be detected. In Fig. 2.16, the transient peak can be seen at an amplitude of 100 keV. In Fig. 2.17, the transient amplitude is just below 100 keV which is almost identical to the charge collected in this neighbor pixel.

In reality, the transient pulse height of the last two examples would be difficult to measure in CZT because of noise and the short pulse time. These types of transient signals have been observed experimentally in slower HgI_2 pulse waveforms.

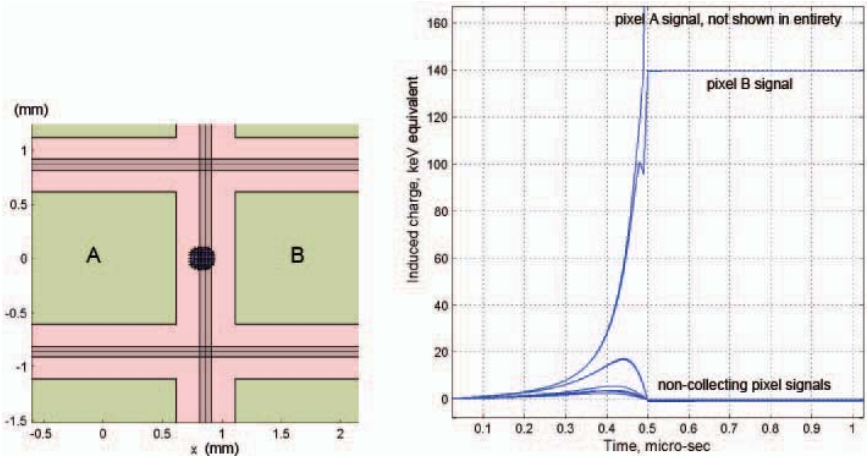

Figure 2.16: A simulated charge sharing event with a transient signal with an amplitude less than the charge collected by the neighbor pixel.

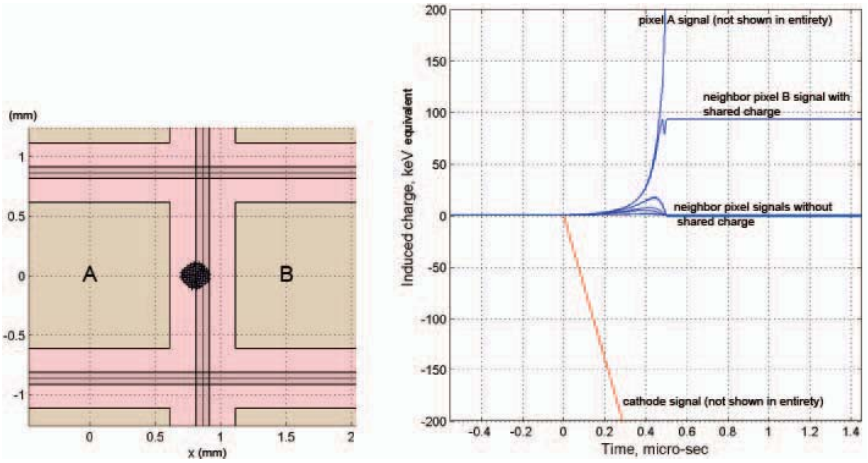

Figure 2.17: A simulated charge sharing event with a transient signal with an amplitude equal to the charge collected by the neighbor pixel.

The signature of a charge sharing event is coincident collection of charge on two neighboring pixels with an observable transient peak. It is possible that a charge sharing event will not have a transient if the charge shared is greater than the induced transient height. It is also possible that a same-depth Compton scatter into a neighbor produces a set of waveforms identical to that of a charge sharing event. Such

a same-depth Compton scatter is relatively rare and can be treated using the formalism discussed for characteristic X-rays in section 2.4.1. Calculations of the sub-pixel interaction position also provide information concerning charge sharing classification. If the result of the position estimate shows that there are two separate charge clouds in two separate pixels, then Compton scattering or another multiple-particle event has occurred. Details of the sub-pixel method are provided in chapter V.

2.5 Summary

It is easy to develop event classification algorithms using noiseless simulated waveforms. If the magnitude of full energy depositions and interaction locations are known exactly, the uncertainty remains only when signatures overlap or there is insufficient information. The simulation results described in this chapter are used later in chapter VI as a comparison to experimental event classification results.

The next chapter introduces the experimental systems used in this thesis study. There are a number of detector response complications that affect the uncertainty of an experimental event classification algorithm. The inherent energy uncertainty limits the accuracy and efficiency of any detection system. Charge generation statistics, material non-uniformity, front-end electronic noise, and leakage current all affect the final measureable quantity of the original energy deposition. Depth dependent pulse height is another detector specific response complication. Because only the electron signal component is used (single polarity charge sensing), same-energy interactions at different depths result in different pulse heights. Electron trapping and weighting potential contribute to this non-uniformity. Since the depth of interaction can be calculated event-by event, this phenomenon can be corrected within the resolution of the depth sensing methods. This and other calibration routines are detailed in

chapter V. Readout electronics and analysis algorithms also introduce complications. Analog readout methods traditionally rely on shaping electronics to filter noise, estimate pulse height, and generate triggers. During the shaping process, the detailed charge motion history is lost. Digital readout preserves the preamplifier signal which contains the best available representation of charge motion in the detector. Sampling frequency and electronic noise affect the quality of waveform data.

CHAPTER III

Experimental 3-D Detector Systems

As introduced in chapters I and II, the detectors used in this study are large volume room temperature semiconductor detectors with pixelated anodes. The purpose of this chapter is to present the design of the specific detectors and associated electronics used in the development of pulse waveform-based event classification methods. An understanding of these system components is critical to the next three chapters that focus on the concepts of: waveform processing, system calibrations, and event classification. The first section of this chapter introduces the HgI_2 and CZT detectors used in this study. The second section describes the prototype readout electronics constructed for these detectors. Section three provides details about the digitization hardware and control software that has been developed to collect data from the detection system. Finally, section four concludes the discussion and highlights the key concepts relevant to the research presented in the following chapters.

3.1 Three-Dimensional Semiconductor Detector Design

3.1.1 Design Motivation

All of the detectors used in this thesis are designed with the capability of Three-Dimensional position-sensitivity and excellent room temperature energy resolution. A detector capable of accurate interaction position measurements is inherently good

for applications such as Compton and coded aperture imaging. Given an accurate interaction position measurement, energy resolution can also be improved by calibrating and then correcting 3-D detector response non-uniformities.

The detectors used in this study have a pixelated anode and planar cathode. Because anode pixels provide measurements of lateral interaction position, segmentation of the cathode is not necessary. A planar cathode reduces further readout complexity. This design has demonstrated accurate measurements of the location of the primary and secondary gamma ray interactions in a semiconductor volume. The 3-D method was first reported by He, et al. [26]. The pixelated anode is used to measure lateral interaction position (i.e. x and y dimensions). The signal of the planar cathode helps provide the third dimension, depth (z). As described in section 2.3, the pulse height of a planar cathode is proportional to the depth of interaction. The depth sensing methods used in this study are discussed further in chapter V.

Another advantage of a pixelated anode is lower shot noise compared to other readout options such as coplanar and cross-strip electrodes. Because pixels have a relatively high degree of electrical isolation from each other, leakage current within the detector bulk is effectively divided between the individual pixels. In contrast, this is not the case of the planar cathode which is affected by the entire bulk leakage current. For example, the cathode noise for one of the HgI_2 detectors studied was nearly three times higher than the pixel noise. The detector designs also include a guard ring that reduces the effect of leakage current on and near the surface of the detector. The guard ring also maintains the effectiveness of the small pixel effect for pixels on the anode periphery. As described in section 2.3, some of the CZT detectors used in this study have a steering grid electrode between pixels to steer electrons away from the inter-pixel gap.

3.1.2 Experimental 3-D Detectors

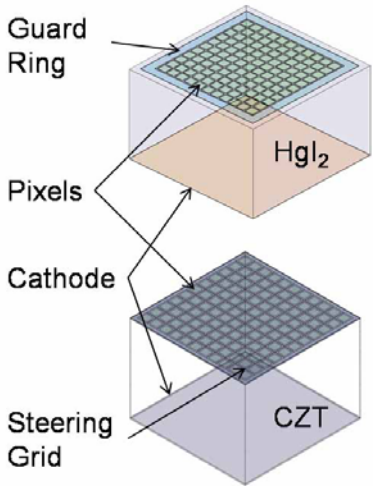

Figure 3.1: Top: A schematic view of the detector design used for the HgI_2 detectors. Bottom: The anode design of the CZT detectors includes pixels and a steering grid surrounding all pixel anodes.

Figure 3.1 illustrates the detectors used in this study. The detector on top is an $18 \times 18 \times 11$ mm^3 HgI_2 crystal. The anode, located on the top of the detector in the figure, is an 11×11 pixel array. The anode pixels are 1.1×1.1 mm^2 with a 170 μm gap. A 1.1 mm wide guard ring surrounds the pixels. The cathode is planar. The electrode contacts are made of palladium. The HgI_2 detectors used in this study were manufactured by Constellation Technology Corporation. [1]

The detector on the bottom of Fig. 3.1 is a $20 \times 20 \times 15$ mm^3 CZT crystal with an 11×11 pixel array. The area of the anode pixels is 1.22×1.22 mm^2. An inter-pixel charge steering grid separates the pixels. The grid is 100 μm wide with a 200 μm gap between the grid and pixel. The cathode is planar. All the electrodes are made of gold. The CZT detectors used in this study were manufactured by eV Products (now eV Microelectronics[2]) and Redlen Technologies[3].

[1] Constellation Technology Corporation, 7887 Bryan Dairy Road, Suite 100 Largo, Florida 33777-1452. `http://www.contech.com/`

[2] eV Microelectronics,373 Saxonburg Blvd. Saxonburg, PA 16056, `http://www.evmicroelectronics.com`

[3] Redlen Technologies, 9865 West Saanich Rd, Suite #107 Sidney, B.C. Canada V8L 5Y8, `http://www.redlen.com`

3.2 Readout Electronics

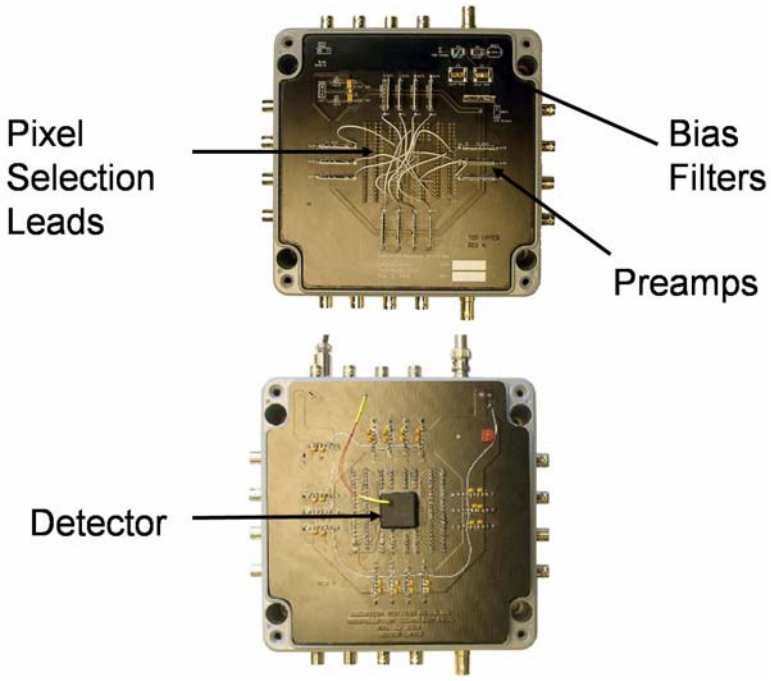

Figure 3.2: Top: The top side of the discrete readout board includes the cathode bias network, preamplifiers, and pixel selection leads. Bottom: The detector is mounted on the bottom of the board.

Figure 3.2 is a view of one of the two prototype test boxes built to study digitized preamplifier waveforms of pixelated CZT and HgI_2 detectors. The lower photograph shows how the detector is mounted to the readout circuitry. This detector is a HgI_2 detector covered by a black plastic cover. The anode surface of the standard CZT and HgI_2 detectors are mounted to a ceramic substrate containing pins that connect to the anode electrodes. The detector surface facing the viewer in the lower photograph of Fig. 3.2 is the planar cathode.

The upper photograph in Fig. 3.2 shows the top side of the printed circuit board. The board contains 15 discrete signal channels. The user can choose to connect any of the 121 pixels using this board. Figure 3.3 shows the general design of the readout electronics for detectors without a common grid. The cathode is biased

using an AC coupled arrangement. Pixel signals are DC coupled. The guard ring surrounding the pixel array is grounded. The second test box (not pictured) includes the capability to apply a bias to the grid in a common-grid detector. Bias is applied to the grid using AC coupling. The charge sensitive preamplifiers used are model eV-5093 manufactured by eV Microelectronics. Rise time of the preamplifier is 20 ns, and the fall time is 1030 μs. The sensitivity of the preamplifier measured using HgI_2 and CZT is roughly 110 mV/MeV.

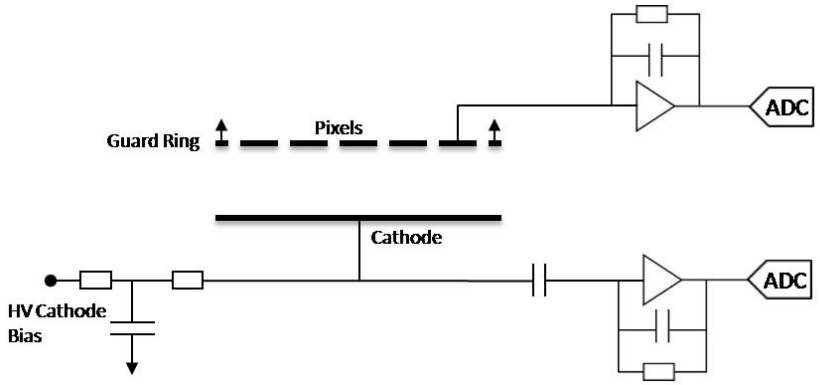

Figure 3.3: A diagram of the discrete readout system. The cathode is biased and read out through an AC coupling circuit. Each pixel is DC coupled to a preamplifier. Only one pixel circuit is shown in this figure. The guard ring is grounded.

3.3 Waveform Digitizer System

The preamplifier signals from the test box described in section 3.2 are digitized using two Gage Applied Technologies Octopus CompuScopes, model CS8389: OCT-838-009. The two cards are wired to share a common clock and trigger signals. Customized control software was developed to facilitate the acquisition of waveforms from all 15 connected detector channels. Each of the two digitizer cards has eight channels and is connected to a computer via a PCI bus connection. Connected to the readout box, the system is capable of digitizing 15 electrode signals simultaneously event by event. When an interaction triggers the system, waveforms of the triggering

pixel, neighbor pixel, and cathode are saved.

The ADC resolution of the system is 14 bits. The resolution of the system's ADC is important because a quantization error is introduced as an analog sample is binned into an ADC channel. This depth of resolution is dependent on the number of ADC bits as well as the ADC voltage range. Quantization error, ϵ, is the difference between the ADC channel value and the analog signal's instantaneous amplitude. The wider the ADC channel, the greater the quantization error. Given an ADC bin of width w, the position within the bin where ϵ is a minimum is near $w/2$, the midpoint of the bin. To the right of this midpoint, the difference is positive; to the left it is negative. If the difference is squared, the value is symmetric about the midpoint and the root mean square of the quantization error can be calculated as

$$\langle \epsilon^2 \rangle = 2 \int_0^{w/2} x^2 \, dx = \frac{w^3}{12} \tag{3.1}$$

where the x is the fractional channel width [33]. Quantization error is then given by

$$\epsilon = \sqrt{\frac{w^3}{12}} \tag{3.2}$$

If the number of bits, n, and voltage range V is known, then

$$\epsilon = \sqrt{\frac{\frac{V^3}{8^n}}{12}}. \tag{3.3}$$

Several voltage ranges were used to collect waveforms from the experimental system. The highest energy photons measured are 2.614 MeV. If all of this energy is deposited in a CZT or HgI_2 detector, the pulse height is roughly 300 mV. To accommodate these signals, a 1 V range ($\pm$ 500 mV) is required. The digitizer system includes a 500 mV range option; however it could not be used because low frequency noise and signal pileup can influence the signal resulting in a larger amplitude pulse that must be corrected.

The maximum sampling rate of the system is 125 MSa/s with a bandwidth of 100 MHz. In order to accurately reconstruct a pulse and avoid aliasing effects, the minimum sampling rate must exceed the Nyquist rate,

$$f_N \equiv 2f_M \tag{3.4}$$

where the f_N is the Nyquist sampling rate, and f_M is the rate of the fastest signal component. The signals from the semiconductor detectors studied in this thesis are relatively slow compared to the sampling frequency of the digitizer. In CZT, electron drift through the detector is on the order of hundreds of nanoseconds. The fastest features of interest are the transient pulses which occur when an electron cloud travels through the region close to the anode surface. Charge mobilities in HgI_2 are an order of magnitude lower than for CZT. All the waveforms collected in this study were sampled at 100 MSa/s, i.e. one sample every 10 ns.

3.4 Summary

The prototype discrete digital readout system is not optimized for real time spectroscopic or imaging measurements. During a typical experiment, pulse waveforms are collected and saved for future analysis. One benefit of this data form is that a single measurement can be analyzed again using different processing or calibration techniques. The method minimizes sources of systematic error including time-dependent detector response non-uniformities, and environmental effects.

This chapter did not include information regarding shaping circuitry for amplitude and timing measurements. The purpose of the readout electronics described in this chapter is to preserve the signal for digital signal processing. Chapter II explained the characteristics and value of signal features as they apply to event classification. One of the challenges of analyzing detector signals is that features are diverse in

terms of their shape and amplitude. A transient peak is a fast signal compared to charge-collection signal. Signals are also complicated due to the presence of electronic noise. The next chapter explains how these challenges can be minimized using digital signal processing methods customized for CZT and HgI_2 event pulse waveforms.

CHAPTER IV

Digital Waveform Processing Methods

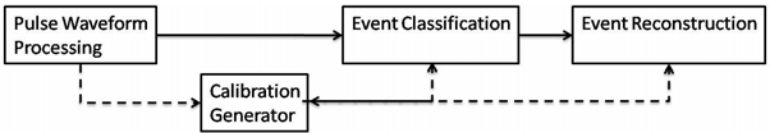

Figure 4.1: The event classification software suite consists of four modules: pulse waveform processing, detector/channel calibrations, event classification, and event reconstruction. The topic of this chapter is the first module: Pulse Waveform Processing

This chapter introduces the methods that have been developed to process pulse waveforms collected by the experimental digital readout system. The software can also be used to process waveforms generated by detector system simulations. All the waveform examples used in this chapter are from experiment. Figure 4.1 is a schematic overview of the different software modules used to process pulse waveform data and apply the subsequent signal measurements. The first step in this flowchart is pulse waveform processing. In this step, amplitude and timing information for the waveform features of interest are measured. Next, if a calibration has not yet been conducted for a particular detector, a calibration routine is run which uses single pixel photopeak events of various energies to obtain a series of calibration parameters. Once calibration parameters have been calculated, they can be used by the event classification and reconstruction routines. After events have been classified, they are passed to the event reconstruction module where calibration and event identity

information are used to reconstruct energies and generate spectra. The details of the first stage, pulse waveform processing, is the subject of this chapter. The calibration module is covered in chapter V Event classification and reconstruction are covered in chapter VI.

In the pulse waveform processing module, digital filters and other algorithm-based methods to analyze detector waveforms are optimized to obtain signal features critical to event classification and sub-pixel position algorithms, including:

- pixel pulse height,
- pixel pulse timing,
- pixel transient pulse height,
- pixel residual tail pulse height,
- cathode pulse height,
- cathode pulse timing, and
- cathode pulse shape,

As described in chapter III, the raw data coming from the digital readout system is in the form of digitally sampled preamplifier pulse waveforms. For each individual radiation interaction history that occurs in the detector, there is a set of discreet digital pulse waveforms that is collected. As described in chapter II, this waveform set includes separate pulse waveforms from three categories of signals: pixels that collect charge, pixels that neighbor collecting pixels, and the cathode waveform. Each category contains different expected signal shapes based on electrode type and whether or not charge is collected. Because of this shape difference, customized waveform processing algorithms are used for each category. Sections 4.2 and 4.3 explain the details of these processes and section 4.4 presents initial efforts that have been made to optimize the process for each category. For each category, there are specific signal features in the waveforms that need to be measured for subsequent

processes including depth of interaction estimates, energy deposition calculations, sub-pixel position estimation, and event classification.

4.1 Waveform Processing Overview

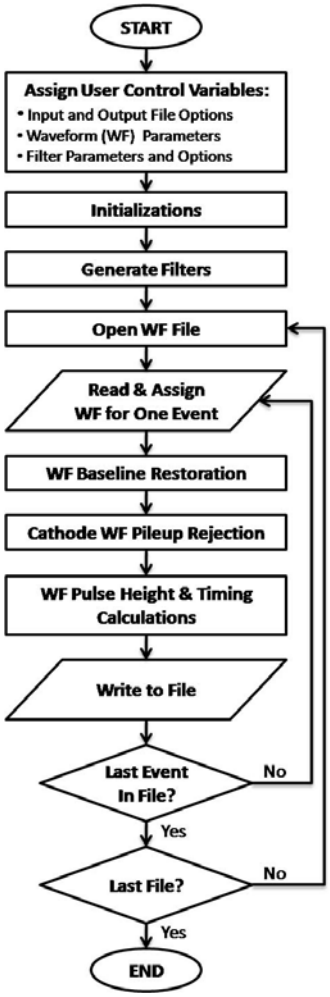

Figure 4.2: The flowchart for the pulse waveform processor module.

Figure 4.2 is a flowchart of the pulse waveform processing code. The first step allows the user to control file options, data specifications, and filtering parameters. Next, initializations are made. Third, shaping filters are calculated based on the user's input. Fourth, files are opened and waveforms are read into memory. Because analysis proceeds event by event, loops iterate through all the events in a file and all

files in a folder. The software has controls that allow the user to select the number of events and files to process. The steps inside the inner loop are the core of the software. The following sections present the details of each step of this inner.

4.2 Pre-Shaping Waveform Processes

There are currently two steps in the pre-shaping processing, baseline restoration and cathode signal pulse pile-up rejection. Baseline restoration is important because the waveforms sampled from a detector signal are discrete in time. The response of a filter to this relatively narrow signal window is different than if the waveform included the entire time domain. For the detectors used in this study, this effect can be dramatic due to the presence of low frequency noise and signal pile-up. Baseline restoration must be applied to all signals in a waveform set. Cathode pile-up rejection is important because waveforms containing signals from multiple incident photon interactions need to be identified so that summation effects do not degrade measurements. Pile-up in the cathode signal is much more common than pile-up in individual pixels. A pixel effectively acts as a separate detector within the limits of the small pixel effect, whereas charge generated anywhere in the detector can induce a significant signal on the cathode.

4.2.1 Baseline Restoration

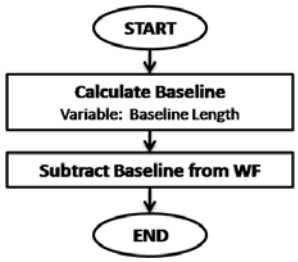

Figure 4.3: The baseline restoration algorithm relies on an estimate of the pre-trigger signal baseline.

Figure 4.3 shows the baseline restoration process for a CZT pulse waveform collected during one of the experiments. The method relies on an accurate estimate of the signal baseline which is calculated by taking the average of the pre-trigger region of the waveform. This region can be varied based on the user's knowledge of the waveform and digitizer waveform acquisition settings. Other methods could be applied to calculate the baseline, including shaping options, but this software does not include such an option because of the significant processing time it would add. Figure 4.4 (a) and 4.4 (b) show an example of a waveform before and after baseline restoration. If the subtraction process was not used, the uncorrected baseline would appear, from the perspective of the filter, as step impulse at the start of the signal. In this example, without the restoration process, the measured cathode amplitude is 20 % larger than it should be.

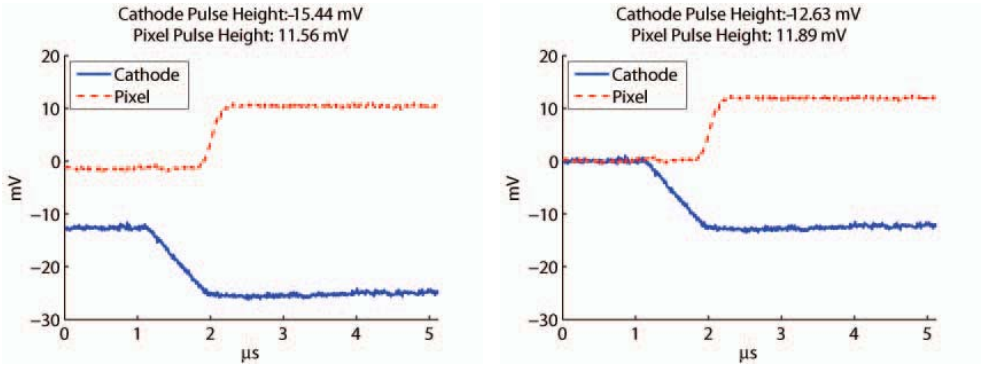

(a) Before Restoration (b) After Restoration

Figure 4.4: A demonstration of the baseline restoration process for pixel and cathode waveforms. The baseline for all signals is restored to zero using the mean value of the pre-trigger pulse waveform.

4.2.2 Cathode Pulse Pile-Up Rejection

The next step in pulse waveform processing module (see Fig. 4.2) is cathode pulse pile-up rejection. In this context, pile-up refers to the presence of signals from multiple interactions of separate photons that originated outside the detector.

In order for pile-up to be detected, evidence of multiple source-photons must be identified within the recorded pulse waveform. Pile-up outside the recorded waveform can influence a recorded waveform; however this case is accounted in the previous section with the baseline subtraction process. In this context, pile-up does not include the multiple photon interactions in a detector from a single photon such as Compton scattering or pair production.

Compton scatter, pair production, and X-ray escape can look like pile-up of multiple-source photons, however they are constrained by when they can occur relative to a pulse trigger time. For these interactions, the electron pulse response of a multiple-site interaction in a single detector must fall within a time window equal to the maximum electron drift time, the time it takes an electron to drift from the cathode surface to the anode surface. When a triggering pulse is detected, there is a window of time within a waveform that other interactions associated with the triggering source-photon are expected to occur. This time window is related to the known time for electrons to drift the length of the detector. The pile-up rejection processes used in this study only look for pile-up outside of this time window.

Cathode pile-up rejection is important because the cathode signal experiences significant charge induction for interactions throughout the detector. For low count rate experiments, this is not a significant concern. If the detector is to be used in a high count rate environment, multiple interaction signals in a waveform can be extracted using a deconvolution process. Figure 4.5 illustrates the pile-up rejection processes. The current software has two different options for pile-up rejection.

The first method is illustrated in Figs. 4.6 (a) and 4.6 (b). This method relies on a calculation of the average signal for two relatively flat regions of the waveform. The method is based on the assumption that the only region that should experience

significant changes in amplitude over the waveform time window is the electron drift region. Since a captured pulse always includes a known amount pre-trigger waveform data, this electron drift region is always centered with respect to time in a recorded waveform. The first region is the "baseline" which is the recorded pulse before charge starts to move in the detector. In reality this region may have a slope due to pileup of the relatively long preamplifier tail or low frequency noise; however, it does not change significantly in the time used to determine the baseline. The second region is the tail region, the relatively flat region in the recorded pulse waveform after the electrons are collected on the anode. This region also has a slope which has components of hole induction and preamplifier signal decay. In this time range, neither component has a significant effect relative to the user-defined threshold level.

If the difference between two baseline region averages is greater than a user-defined threshold, then a pile-up flag is triggered. The threshold used in this study is set at a multiple of the standard deviation of the measured noise fluctuation. Figure 4.6 (a) shows a pile-up event in the pre-trigger time window of a pulse waveform. Figure 4.6 (b) shows a pile-up event in the post-trigger time window. The advantage of the averaging method is that it is fast compared to the second method which relies on a fast shaper. The downside is that the averaging method only analyzes the baseline and tail region. If cathode pile-up occurs in the "electron drift time window," then the pile-up will not be detected.

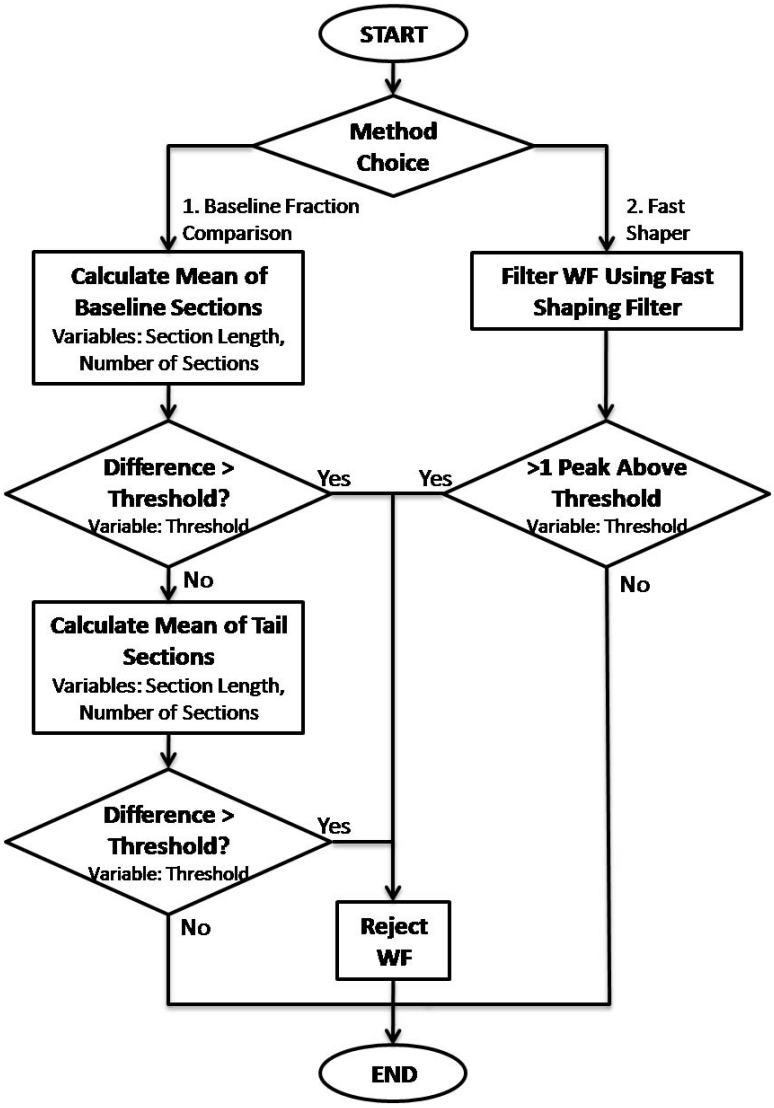

Figure 4.5: The cathode pulse pile-up rejection used in this study has two method options: baseline fraction comparison and fast shaper. Pulse pile-up on the cathode signal is detected to eliminate multiple source-photon interaction events.

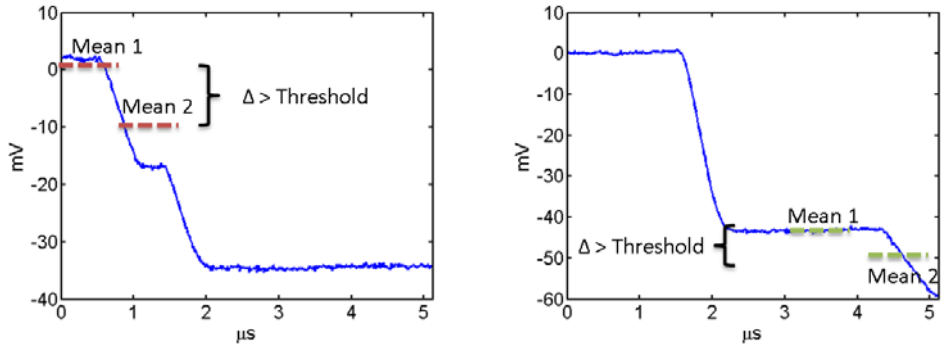

(a) Mean Values for Two Baseline Region Windows (b) Mean Values for Two Tail Region Windows

Figure 4.6: The baseline and tail-average comparison method for cathode pile-up rejection relies on averages of selected pre-trigger and post-trigger waveform time regions. If the difference between the averages is greater than a threshold, the waveform is rejected.

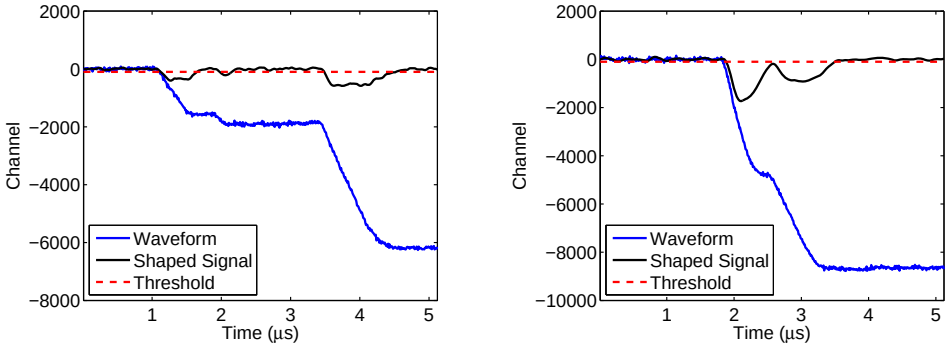

(a) Multiple pile-up Example (b) Pile-up In Electron Drift Region Example

Figure 4.7: The second cathode pile-up rejection uses a fast shaper to detect the features in a pulse waveform associated with additional photon interactions. If the filtered signal contains a greater than expected number of pulses above a threshold, the waveform is discarded.

The second method for cathode pile-up rejection uses a fast shaping filter. Examples of this method are shown in Figs. 4.7 (a) and 4.7 (b). A threshold is used to detect shaped peaks corresponding to the time features associated with pile-up. The figure on the left illustrates how the method can detect three different events. The threshold is set at a level above the expected noise level. The figure on the right shows how the method overcomes the shortcoming of the averaging method for pile-up in the electron drift range.

4.3 Digital Filters

This section covers the techniques developed to measure the signal features of pulse waveforms. One of the advantages of digital signal processing is its inherent flexibility. Filters and filter variables can easily be changed in computer code. Still, a filter-based measurement is limited by the quality of the incoming data. Algorithms to analyze digital signals can be as advanced as computing resources allow. The goal of digital signal processing is the same as analog systems, to extract desired information from a signal obscured by noise. This chapter looks at different digital filters and filter variables such as peaking time for the separate but related applications of energy, timing, and sub-pixel position estimation.

4.3.1 Cathode Waveform Measurements

Figure 4.8 outlines the process for measuring cathode waveform signal features. Features of interest are signal amplitude and the start and stop time of the pulse rise region (time range of electron movement). Each step in this flowchart includes the associated user-defined variables and the signal feature measurements or calculations made in that step. In the first step, the user can chose between CR-RC or triangular shaping filters and can vary shaping time. The cathode signal is processed before

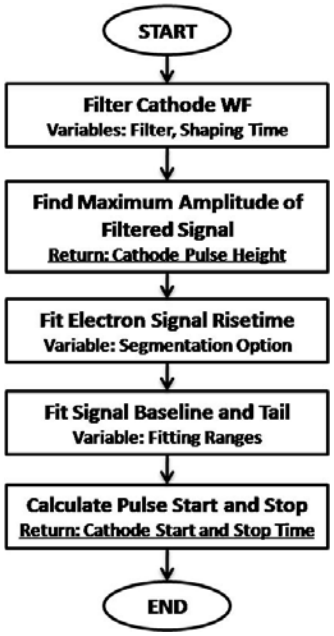

Figure 4.8: The cathode waveform pulse height and timing process.

other signals because it defines the electron drift range, which enables more efficient and accurate measurements of pixel signal features.

First, cathode waveforms are passed into an analysis routine that uses a shaping filter to obtain pulse height. Figure 4.9 (a) demonstrates the method to estimate pulse height. In this example, a CR-RC filter is used. A linear fit method is used to obtain pulse start and stop time of single-interaction cathode signals. Figure 4.9 (b) shows the linear fit method. The cathode rise start and stop time is found by calculating where the fit line crosses the baseline and tail estimates.

The linear fit time pickoff method is used because it exhibits virtually no time amplitude-walk. A discrimination threshold is not used, and the accuracy of the method depends on how well the baseline and leading edge of the cathode signal can be fit. At first, below a cathode amplitude of roughly 80 keV, the accuracy of this method suffers due to difficulties in fitting the cathode slope. Figure 4.10 (a) demonstrates the reason (here the cathode waveform polarity has been inverted).

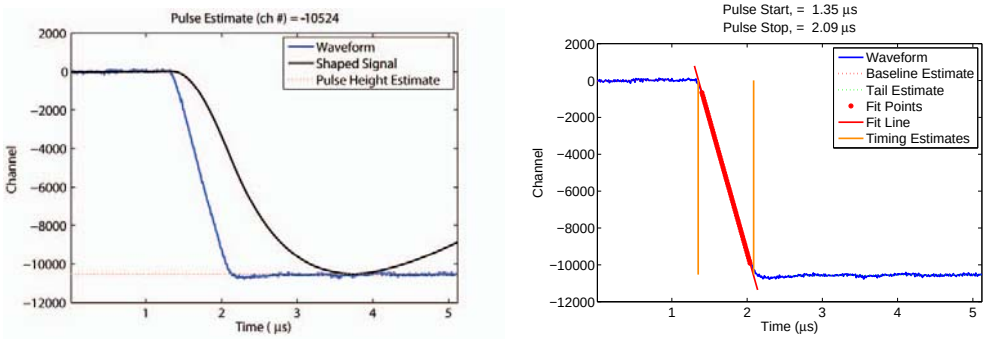

(a) Pulse Height Calculation

(b) Timing Calculation

Figure 4.9: A shaping filter is used to estimate the cathode waveform pulse height. A linear fit of the cathode electron drift pulse, and estimates of the signal baseline and tail are used to estimate pulse timing features.

In this example, the algorithm could not find the leading edge of the electron motion. The amplitude of the cathode signal was too low. This problem is corrected using a step that checks that the fit of the cathode slope is accurate. For low amplitude events, if the calculated start and stop time are wrong, the range of the fit is reduced to include fewer points in the rise time region. Further iterations assign the best number of points to be included in the fit. Figure 4.10 (b) shows corrected result for the same waveform. This correction is important because cathode amplitudes can have low amplitudes regardless of energy. A large energy interaction can have a low amplitude cathode pulse if the interaction occurs near the anode.

One assumption of the cathode slope fit method is that the electric field (or electron mobility) is constant throughout the entire detector thickness. For most detectors this is a valid assumption; however, some HgI_2 detectors in this study had non-linear cathode slopes. When the shape of the cathode pulse is known to be nonlinear, a higher order polynomial fit can be used to measure timing features.

The cathode slope also contains information of multiple pixel events. Figure 4.11 (a) shows waveforms from a multiple pixel event. There is a noticeable change in the cathode slope at 2 μs due to two separate charge clouds at different detector depths.

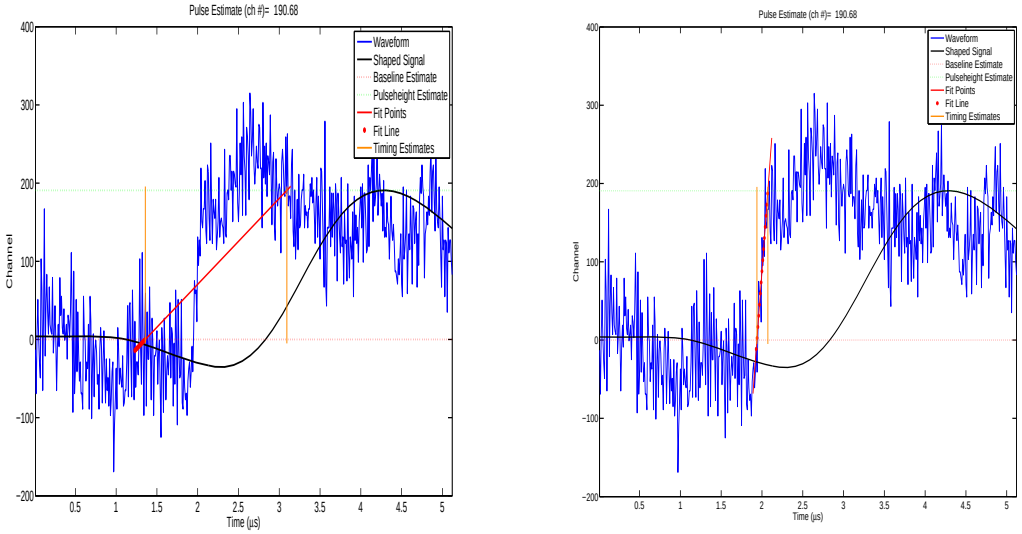

(a) Before Fit Correction

(b) After Fit Correction

Figure 4.10: The relatively high level of noise in the cathode signal makes a fit of the leading edge difficult for low amplitude pulses. If a bad fit is detected, the fitting process is repeating using different regions of the rise time to obtain a best fit.

If a multiple pixel event is detected, based on measurement of more than one pixel signal above an energy threshold, then the cathode waveform is passed to a routine that uses the charge collection time of the pixel signals to break up the cathode waveform into regions. A fit is applied to the first cathode region to determine the cathode pulse start time. This process is illustrated in Fig. 4.11 (b).

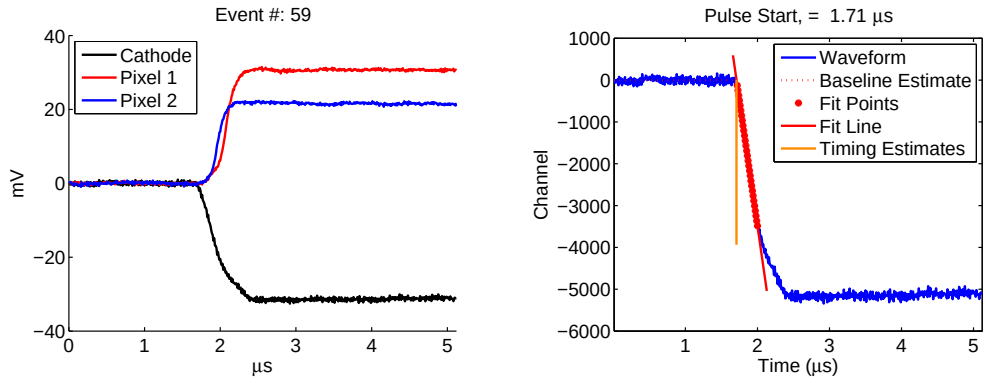

(a) A multiple pixel event.

(b) Corrected cathode slope fit.

Figure 4.11: Multiple pixel events require different time pickoff methods for the cathode waveform. When interactions occur at multiple depths, the cathode signal rise time has different slopes.

Figures 4.12 (a) and 4.12 (b) show two alternate time pickoff methods that have been implemented in the software. The first alternate method uses a linear fit to find the rise time, but the baseline and tail are not fit. Instead, the baseline is assumed to be zero and the tail is assumed to be the filtered pulse height value. The advantage of this method is that no averaging is needed which saves computation time. The second alternative shown in Fig. 4.12 (b) is to use more advanced fitting methods to determine the electron drift start and stop time. In this example, a least squares polynomial fit is used to fit the area near the corners of the waveform.

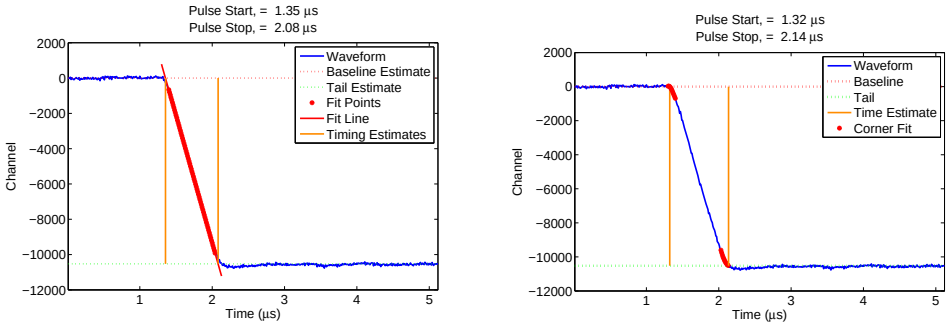

(a) Linear Fit Method With No Baseline or Tail Fit

(b) Pulse Fit Method

Figure 4.12: Two examples of alternate timing methods include the linear fit without baseline or tail fit, and the pulse fit method.

4.3.2 Pixel Waveform Measurements

Measurements of pixel waveforms are slightly different than that of cathode waveforms because the shape of the waveform for collecting and non-collecting pixels is different than the cathode waveform. Figure 4.13 illustrates the steps associated with the pixel waveform process. The details of these steps are provided with examples later in this subsection. A waveform is first passed into an shaping routine designed to obtain the pulse height estimate. This routine is identical to the cathode filtering step described in the previous subsection, however the user can define filters and filter variables that have been optimized for the pixel signal.

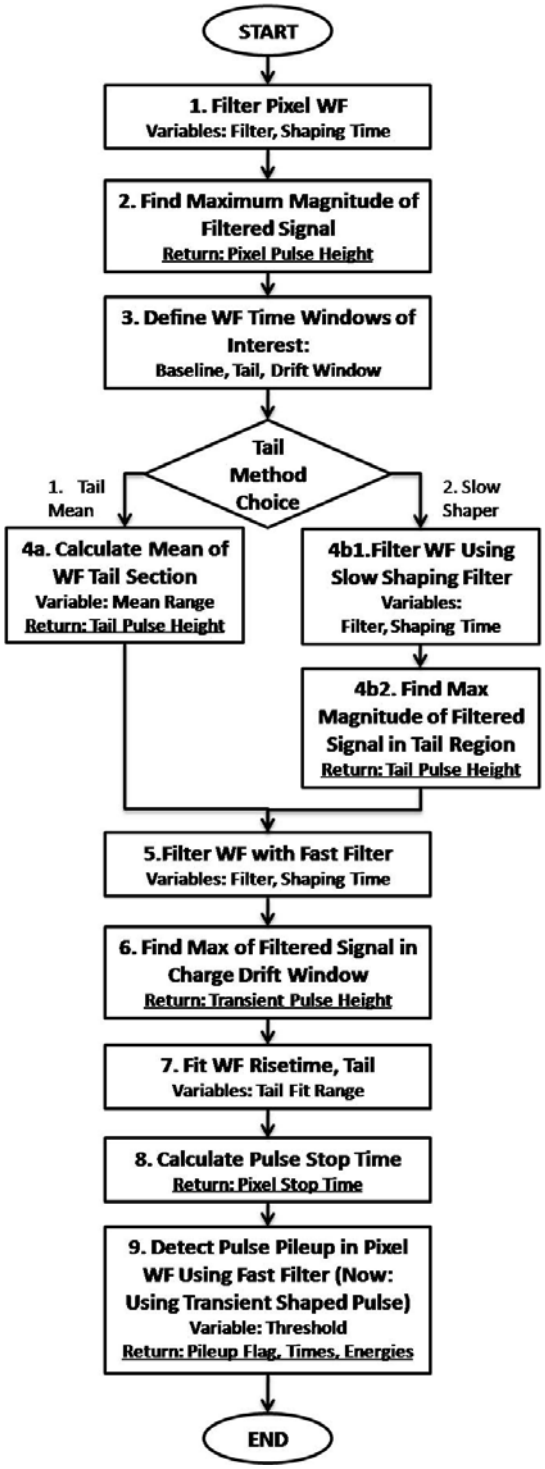

Figure 4.13: The process to determine pixel features including: pulse height, timing, tail, transient, and pile-up.

In step 2, the maximum amplitude of the shaped signal from step 1 is calculated. This serves as the pixel pulse height measurement. In step 3, different regions of the waveform are defined for further analysis. Again, this is identical to the regions defined in the cathode signal discussion (baseline, electron drift, and tail regions), however the charge drift time calculations made in the cathode signal analysis are used in this routine to define these regions of time. For example, if charge is calculated to drift between $t = 1.5$ and $t = 2.5$ μs using the cathode pulse, then this time range is used to limit where pixel signal baselines, tails, and electron pulses will be expected.

Step 4 is the calculation of the pulse tail amplitude. An independent measurement of the tail pulse amplitude allows for verification that charge is collected in a pixel. There are two options for this measurement. The first method (left path), is a calculation of the mean amplitude of the tail signal region. The second method (right path) relies on a slow shaping filter to estimate tail height. After tail height is measured, the next step is to find the transient peak amplitude. A fast filter is used. Again, users can define filters and filter variables as appropriate to the particular detector being used. In step 5, transient amplitude is calculated by measuring the maximum amplitude of the filtered signal in the electron drift region of the filtered signal. Excluding the signal outside of the electron drift region helps minimize misidentification of the transient peak due to its small amplitude.

The next step is designed to calculate the end of the electron drift time in the pixel signal. Like the cathode time pick-off method, a fit is applied to the rise time portion of the pixel signal. The user can define the range of this fit, however, as described in the cathode section, an iterative process ensures that an appropriate fit is used. Step 9 analyzes the pixel signal for any pile-up. Pile up in the pixel signal within the electron drift time region indicates the presence of a scattered photon, characteristic

X-ray, or annihilation photon interaction in the same pixel. The method is the same as the fast shaper method described in the cathode pulse pile-up rejection method described in section 4.2.2. In order to save computation time, the shaped signal from the transient pulse measurement in step 5 is used as the fast shaped signal for pileup detection. If pileup is detected, a special flag is issued for the event classification algorithms used later in the analysis. The energy and time of the pile up features are also recorded.

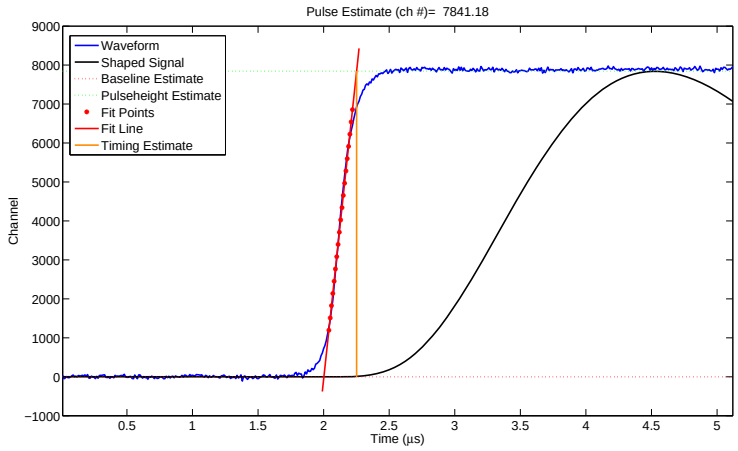

Figure 4.14: The waveform of a pixel that collects charge is analyzed for pulse height and timing.

Figure 4.14 demonstrates the measurement of the pulse amplitude and charge collection time for a pixel where charge collection has been detected (a triggered pixel). The pulse amplitude is the first step of the flow chart in Fig. 4.13. The electron collection time measurement is the third to last step in Fig. 4.13, however it discussed here to consolidate the figures for this particular pulse being analyzed. In this example, a CR-RC filter is used to measure the energy-proportional signal amplitude. Like the cathode time pick-off method, a fit is applied to the pulse to provide an estimate of the charge collection time. Due to the non-linear shape of the pixel pulse, a linear fit results in an underestimate of the charge collection time. If a

more accurate estimate is needed, a higher order polynomial fit can be used for the fit. The software also offers the option to adjust which points in the pulse are used for the fit.

Figures 4.15 (a) and 4.15 (b) demonstrate how the signals of non-collecting pixels are measured. There are two important features in non-collecting neighbor pixels: the amplitude of the signal tail and the transient peak. The waveform in Fig. 4.15 (a) has a well defined transient peak and tail. A fast shaping filter is used to measure the transient peak and a slow shaper or averaging process is used to measure the tail. Figure 4.15 (b) is an example of a neighbor pixel waveform with a low amplitude transient and tail. Amplitude measurements are still possible, but they are limited by system noise.

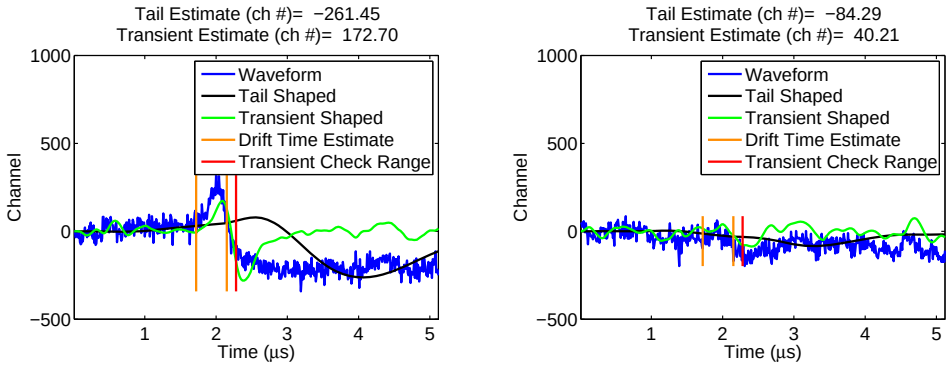

(a) A Relatively Large Transient Signal

(b) A Relatively Small Transient Signal

Figure 4.15: A comparison of shaping processes for two non-collecting pixel signals. Transient signals require shorter shaping times than the pulse height estimate shapers. The pulse waveform tail requires a relatively long peaking time. Knowledge of the electron drift window from the cathode waveform analysis provides a time range to look for transient and tail features.

The measurement of the tail amplitude serves as a double check on the original determination of how many pixels collect charge which is originally based on a trigger discrimination threshold. It is not uncommon that the charge collected in a neighbor pixel is lower than the system trigger threshold. Often, this charge is a result of charge sharing. It is even possible that the measurement of a negative tail on a

neighbor corresponds to charge collection. As explained in section 2.3, an interaction near the anode will result in a negative signal on a neighbor pixel. If a fraction of charge is collected in this neighbor, the amplitude of the tail may still be negative if the difference between the negative component and the positive component due to collected electrons is less than the negative component. This small amount of charge can be measured if the tail amplitude is compared to the expected tail in the other neighbor pixel tails. Ultimately, the tail amplitude measurement is limited by noise.

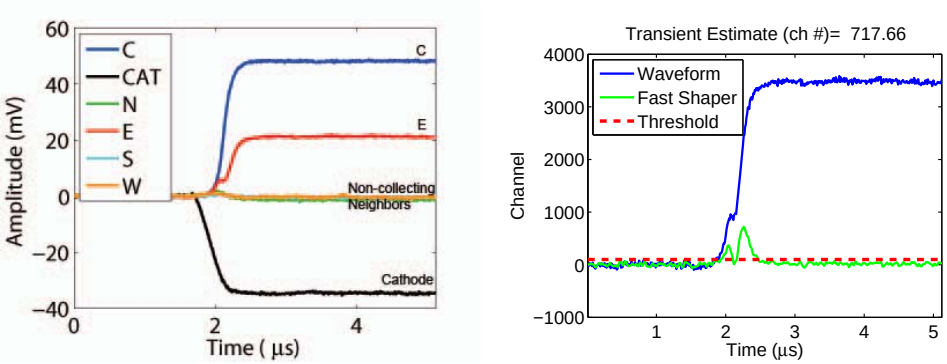

(a) Original Waveform Set

(b) Pixel Pulse Pile-up Detection

Figure 4.16: Pulse pile-up detection in pixel signals. Pile-up detection is critical because it allows for the detection of Compton, X-ray, and pair production annihilation radiation in a single pixel.

If the tail amplitude is above a user defined threshold, the waveform is passed to the pulse pile-up detection routine (using the fast shaper method mentioned earlier for the cathode signal) which detects the presence and pulse height of a Compton or characteristic X-ray interaction in the waveform response of a single pixel. Figures 4.16 (a) and 4.16 (b) show an example of the pulse pile-up detection method. Currently, the pulse pile-up fast shaper does not require any additional processing because the same shaped signal that was used in the transient pulse height measurement can be used. Pile-up from more than one source photon should already be eliminated from the cathode pulse pile-up rejection routine. Ideally all pile-up events in the pixel would be due to Compton scattering, X-ray escape, or pair production.

If pile-up is observed, timing and amplitude of the separate pulse are measured. Figures 4.17 (a) and 4.17 (b) show timing measurements before and after pile-up is detected. Comparing the figures, the rise time fit in Fig. 4.17 (b) is better than the fit in Fig. 4.17 (a). Pile-up can also affect the shaped signal. In this example, a longer shaping time is needed to avoid the ballistic deficit that can be observed in Fig. 4.17 (a).

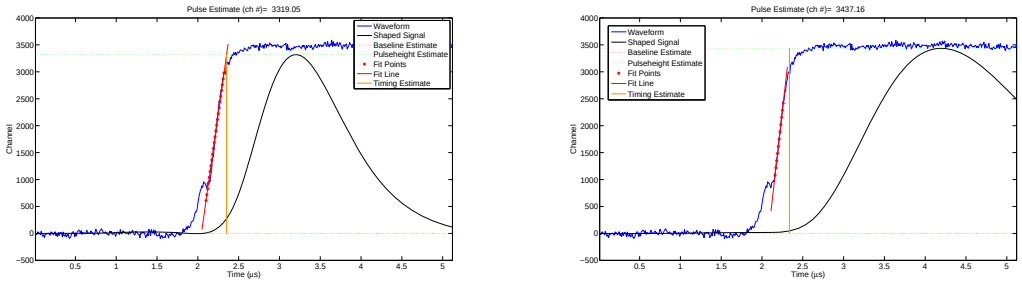

(a) Before

(b) After

Figure 4.17: Necessary additional processing steps for single-pixel multiple-site events. When pixel pulse pile-up is detected, additional analysis must be conducted to correct for ballistic deficit and improper timing.

4.4 Digital Filter Optimization

There are countless ways to estimate the pulse heights of a digitized pulse waveform, including methods such as simple and weighted averages as well as more advanced methods based on filters carefully optimized for an expected signal. The goal for filter optimization in this study was to maximize signal-to-noise ratio (SNR) without excessive computation. Digital filters based on the approximation of a Gaussian shape are useful in spectroscopic applications because of its high SNR. In analog systems, this is achieved through application of a CR differentiation circuit followed by a number of RC integration stages. The output amplitude A_{out} is related to the input amplitude, A_{in} by

$$A_{out} = A_{in}\frac{\left(\frac{t}{\tau}\right)^n e^{\frac{-t}{\tau}}}{n!} \tag{4.1}$$

where n is the number of integrators and τ is the time constant. The number of integrators can be set according to the user's specifications; however, it has been shown that four stages of integration are sufficient to model a Gaussian shape for most practical applications [33]. In this example, $n = 1$, and $\tau = 4\ \mu s$. Figure 4.18 compares resolution results achieved in one of the HgI_2 detectors using approximate Gaussian filters with n=1 and n=6 using the experimentally determined optimal peaking time for each filter.

4.4.1 Filter Optimization for CZT Detectors

A detailed study was conducted by Yuefeng Zhu that used experimental CZT waveforms collected by the system described in chapter III to compare CR-RC^n, triangular, and the theoretically optimal filter [69]. The results of this experiment showed that the filter that yielded results closest to the theoretical best filter was

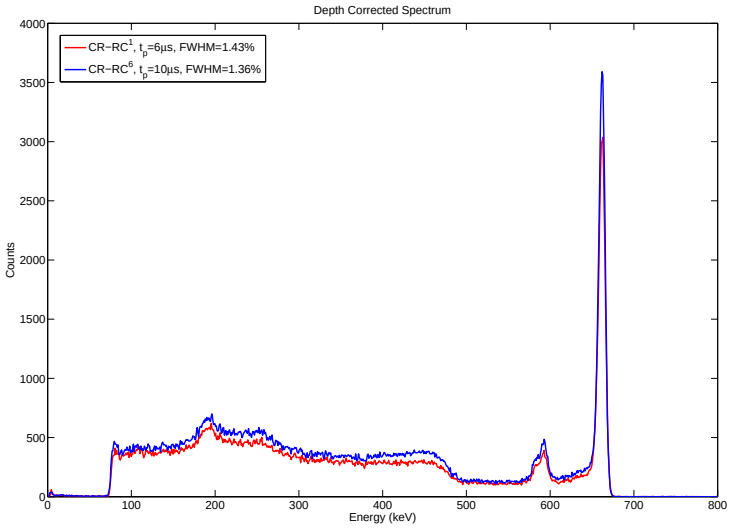

Figure 4.18: HgI_2 energy spectra for Cs-137 from same set of data using two different digital filters.

CR-RC^4 with a shaping time of 200 ns. To measure transient peaks, the optimal filter is CR-RC with a 200 ns shaping time for the -3000V bias used in the experiment.

To further study filter optimization, waveform data sets were collected using a signal pulse generator and a Cs-137 source. In both cases, the cathode was biased at -3000 V and the steering grid was biased at -40 V. Figure 4.19 (a) summarizes the results from the test pulse experiment in CZT using a digital CR-RC filter. Thirteen pixels were tested. The FWHM of the test pulse peak for each pixel is shown as a function of shaping time. The optimal shaping time for this filter is approximately 1.0 μs. Figure 4.19 (b) plots the test pulse peak area for each of the FWHM measurements in Fig. 4.19 (a). This ensures the consistency of the measurements by making sure that no peak events are discarded, which may bias the results. Figure 4.19 (c) shows the results for the cathode signal. These results also indicate the electronic noise level in the detector system. For pixels, the electronic noise is between 2.5 and 3.5 keV. The electronic noise on the cathode is just above 4 keV.

These CR-RC results can be compared to the results of the CR-RC^4 and triangular filters shown in Figs. 4.20 and 4.21. The filter that performed the best in the pulser test is the triangular filter. The best FWHM for pixels was measured to be approximately 1.65 keV using a shaping time of 4 μs. The best cathode FWHM is just above 3.6 keV.

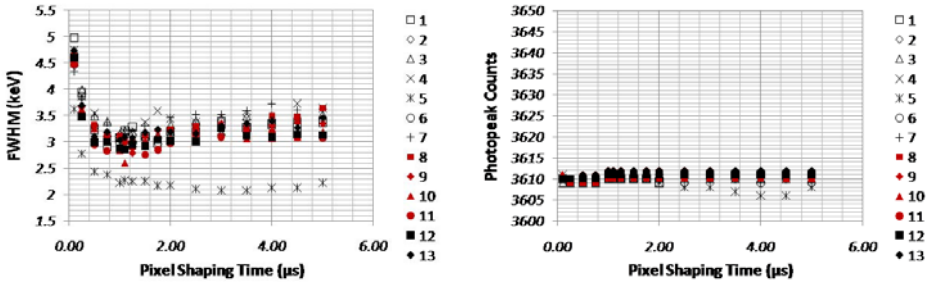

(a) Pixel FWHM

(b) Pixel Pulser Peak Area

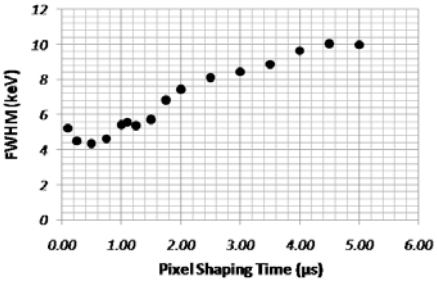

(c) Cathode FWHM

Figure 4.19: The FWHM (keV) of a test pulse signal for 13 pixels and the cathode using a digital CR-RC filter with various shaping times in CZT. Each pixel is represented by a different shaped marker. Since the same data set is used in each measurement, the peak area should be the same in each case. To demonstrate this consistency, the peak area is also reported in (b).

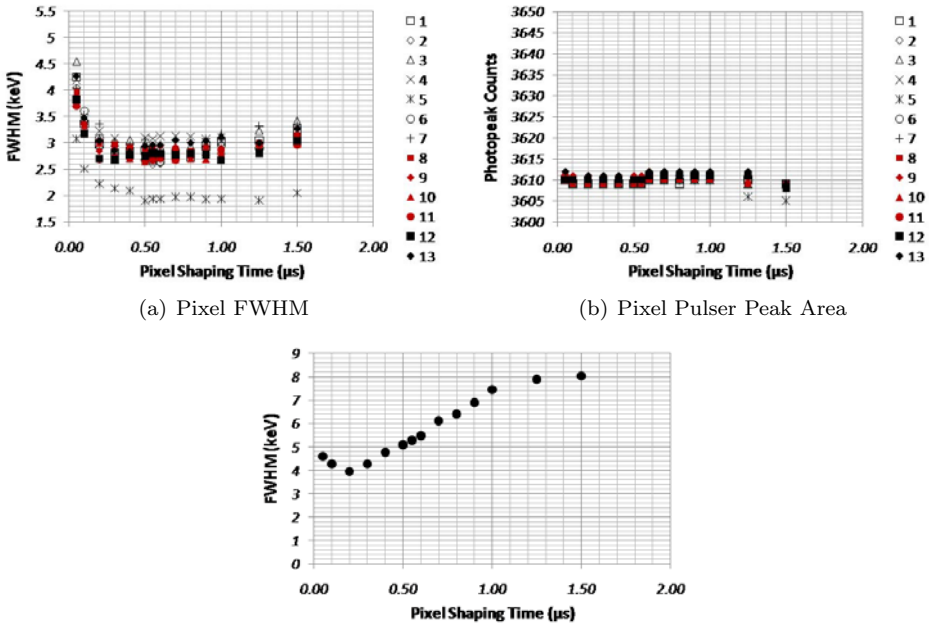

(a) Pixel FWHM

(b) Pixel Pulser Peak Area

(c) Cathode FWHM

Figure 4.20: The FWHM (keV) of a test pulse signal for 13 pixels and the cathode using a digital CR-RC^4 filter with various shaping times in CZT. Each pixel is represented by a different shaped marker. Since the same data set is used in each measurement, the peak area should be the same in each case. To demonstrate this consistency, the peak area is also reported in (b).

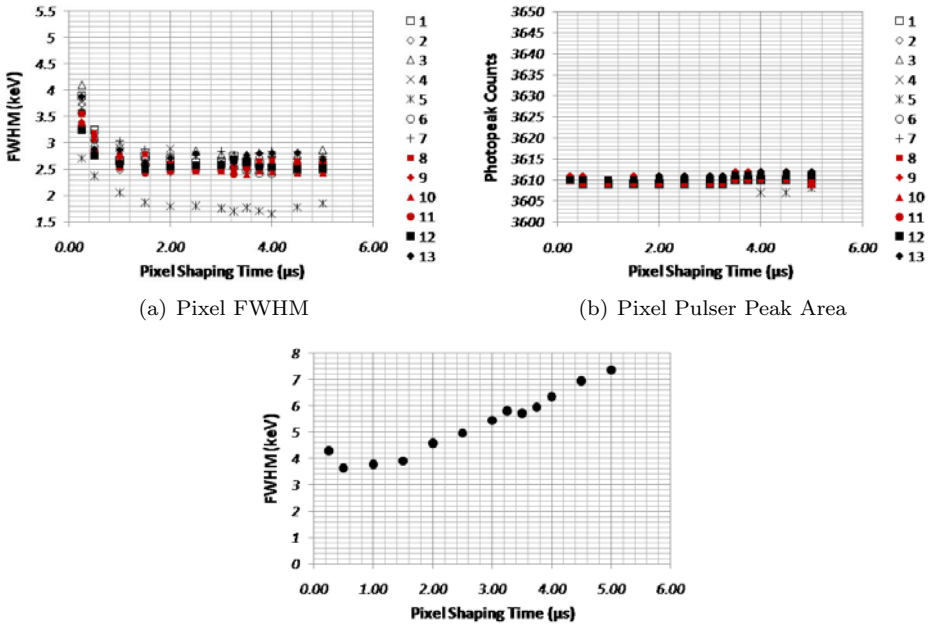

(a) Pixel FWHM

(b) Pixel Pulser Peak Area

(c) Cathode FWHM

Figure 4.21: The FWHM (keV) of a test pulse signal for 13 pixels and the cathode using a digital triangle filter with various shaping times in CZT. Each pixel is represented by a different shaped marker. Since the same data set is used in each measurement, the peak area should be the same in each case. To demonstrate this consistency, the peak area is also reported in (b).

Figure 4.22 compares the FWHM of a 662 keV photopeak using the same three filters. Again, care is taken to make sure the same number of photopeak events is used. The photopeak area should be the same in each measurement because the same waveforms were used for each trial. The slight difference in photopeak area is due to the filter response in neighbor pixels. Fast shaping times are effective at picking up the amplitude of the transient pulse in neighbor signals. When this happens, the system thinks the neighbor actually collected charge and classifies the event as a multiple pixel interaction. The result is that the event is removed from the set of single pixel photopeak events which are the only events used in this noise study.

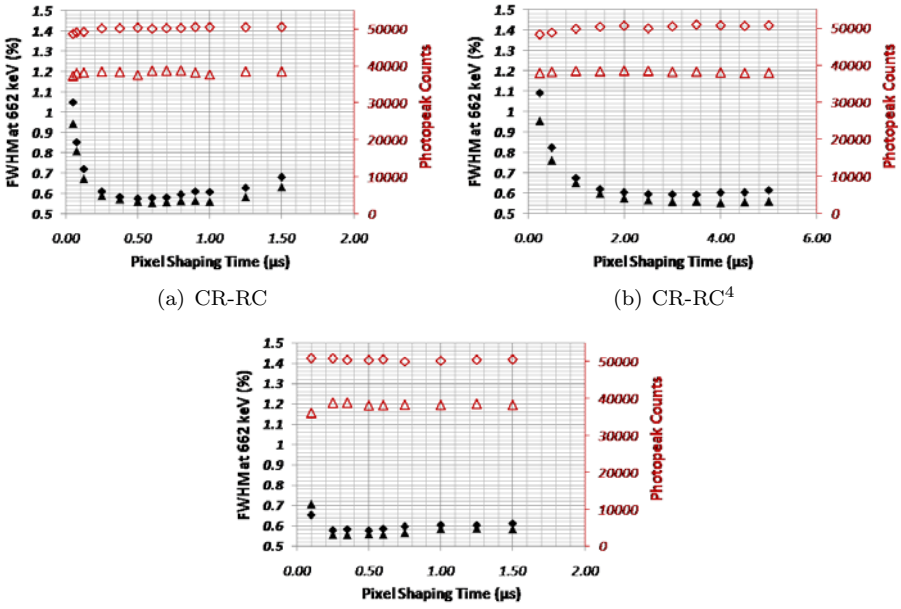

(a) CR-RC

(b) CR-RC^4

(c) Triangle

Figure 4.22: A comparison of the resolution (FWHM at 662 keV) of CZT pixels for various shaping options. Each pixel is represented by a different shaped marker. The second axis (red, to the right) shows photopeak counts for each shaping option.

4.4.2 Filter Optimization for HgI_2 Detectors

Optimal shaping was also studied for HgI_2 detectors. Figure 4.23 compares filter options for pixel signals in a HgI_2 detector. Figure 4.24 shows the FWHM of a pulser peak as a function of shaping time for a CR-RC filter. The FWHM for pixel number one was measured to be 3.06 keV using a shaping time of 2.5 μs. Figure 4.25 shows the results for 662 keV photopeak events. Using a CR-RC^4 filter and a shaping time of 1.75 μs, the FWHM was measured to be 1.07%. The main reason that optimal shaping time for HgI_2 is longer than that of CZT is because electron drift time in HgI_2 is longer.

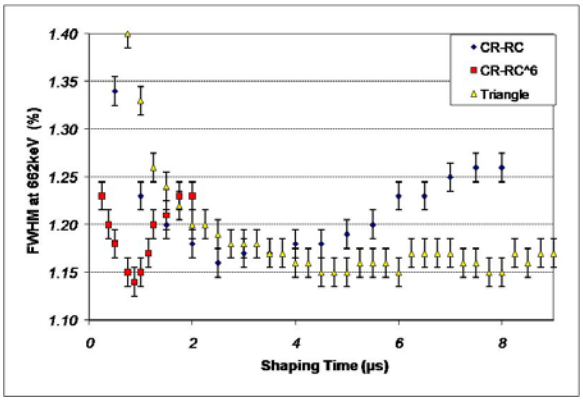

Figure 4.23: Comparison of filter choices for HgI_2 pixels.

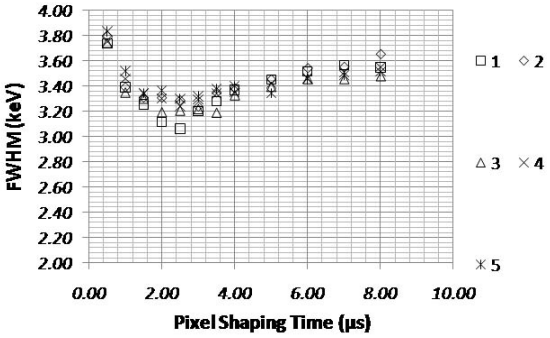

Figure 4.24: The FWHM (keV) of a test pulse signal for 5 HgI_2 pixels using a digital CR-RC filter with various shaping times.

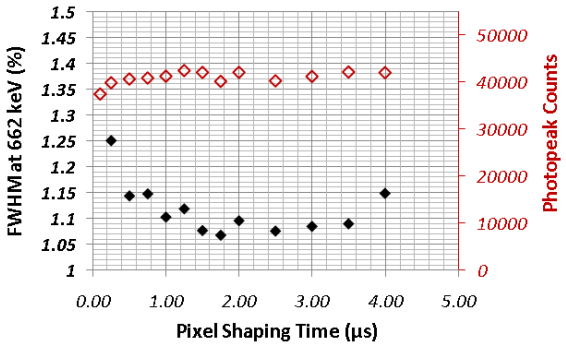

Figure 4.25: Energy resolution of HgI_2 pixels for various shaping times for a digital CR-RC^4 filter.

4.5 Waveform Processing Summary

This chapter explained how different waveform signal features are measured. Optimized filters allow for more accurate measurements of these signals. The final output of the waveform processing steps described in this chapter is an event list. Each event in the list contains the uncalibrated values from the amplitude and time feature measurements for the cathode and each pixel in the event. An example of this output for two events is shown below in Fig. 4.26.

For each event, measurements of pulse waveform features for the cathode and all relevant pixels are included in the event output file. For each pulse waveform measurement, the electrode number is recorded for reference. The cathode channel has an electrode number of 1. The cathode measurement is always the last measurement set included for a single event. Next, the pulse height amplitude is reported. The third column is the pulse trigger time. For the pixel signals, this time is the electron collection time. If no charge is collected in a pixel, trigger time is not calculated and a flag value of -1 is reported. For the cathode, the time reported is the start of the electron motion. Column 4 lists the tail amplitude for the pixel signals only. Column 5 lists the transient amplitude, and the last column is the pulse pileup field for pixel signals. If pulse pileup has been detected in the electron motion region of the pixel

signal, then the features of the pileup are included. If no pileup is detected, a flag value of -1 is reported.

The first event in Fig. 4.26 is a single pixel energy deposition. Measurements of the cathode signal as well as ten pixel signals are included. Pixel number 24 is the triggering pixel in this event. The amplitude of this pulse is 856 channels and the electron collection occurred at 4.7 μs. Since a large amount of charge was collected in this pixel, the measurement of tail height and transient height are roughly equal to the pulse height measurement. This does not mean that the transient height was 864 channels. Logic must be included in the event classification routine to account for this type of measurement. Columns 4 and 5 compare the often significant difference between the tail amplitude and the transient amplitude. For example, the tail amplitude in pixel 32 is 2 channels whereas the transient amplitude is 92 channels, which is equivalent to a charge collection pulse height of roughly 45 keV. The usefulness of the transient and tail amplitudes will become evident in the next chapters.

The second event in Fig. 4.26 is a three pixel event. Since three pixels collect charge, the electron collection time is calculated for each separate collection. The cathode trigger time gives when the electron motion started. Next, electrons were collected in pixel 24, followed by collection in pixel 20, and finally pixel 32. The next chapter analyzes how these measured values are used to calibrate the detector response function for interactions occurring anywhere in the detector. Chapter VI describes the event classification routine which also uses these event lists as input.

Electrode Number	Pulse Amplitude (chn)	Trigger Time (µs)	Tail Amplitude (chn)	Transient Amplitude (chn)	Pileup Field (flag or chn, µs)
32	11.77	-1	2.14	91.58	-1
24	855.96	4.7088	859.65	864.07	-1
59	-12.7	-1	-11.57	14.68	-1
63	-4.07	-1	-2.24	8.63	-1
71	6.58	-1	0.06	2.53	-1
75	-7.09	-1	-6.34	6.25	-1
28	-14.04	-1	-5.5	60.64	-1
20	6.25	-1	2.94	20.2	-1
64	-5.75	-1	-3.79	4.26	-1
79	-7.07	-1	-5.24	3.37	-1
1	852.71	4.3382			
32	327.02	4.8214	327.63	318.43	-1
24	123.02	4.5989	123.62	143.48	-1
59	-4.1	-1	-1.24	10.66	-1
63	5.33	-1	6.6	9.39	-1
71	-6.3	-1	-6.03	-2.3	-1
75	-3.23	-1	-1.09	10.96	-1
28	-9.95	-1	-9.51	20.05	-1
20	357.77	4.6365	359.37	362.33	-1
64	5.59	-1	3.15	6.75	-1
79	4.81	-1	1.48	3.57	-1
1	518.79	4.131			

Figure 4.26: A two-event sample of the output file generated by the waveform processing routine. Both events contain waveform measurements from the cathode and same 10 pixels.

CHAPTER V

System Calibration Methods

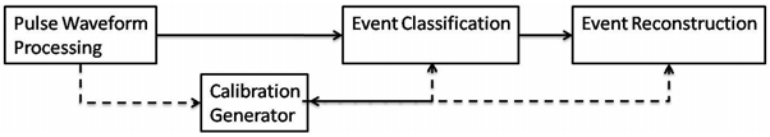

Figure 5.1: After pulse waveform have been processed, they can be passed to a calibration routine that uses single pixel events to generate calibration parameters that will be used in subsequent analysis routines.

As seen in Fig. 5.1, after the waveform processing step and before the event classification module, is a calibration routine. The purpose of the calibration generator is to calculate calibration functions and look-up tables that provide a 3-D normalization of the detector response for interactions occurring anywhere within the detector. The justification for these corrections is based on the detector response theory presented in section 2.2. Response complications that are treated include pulse height deficits due to trapping and weighting potential, electronic gain differences between channels, weighting potential cross-talk for multiple pixel events, and tail/transient peak induction non-uniformities. Another calibration parameter that is calculated is the distribution of sub-pixel events in each pixel as a function of interaction depth and energy deposition.

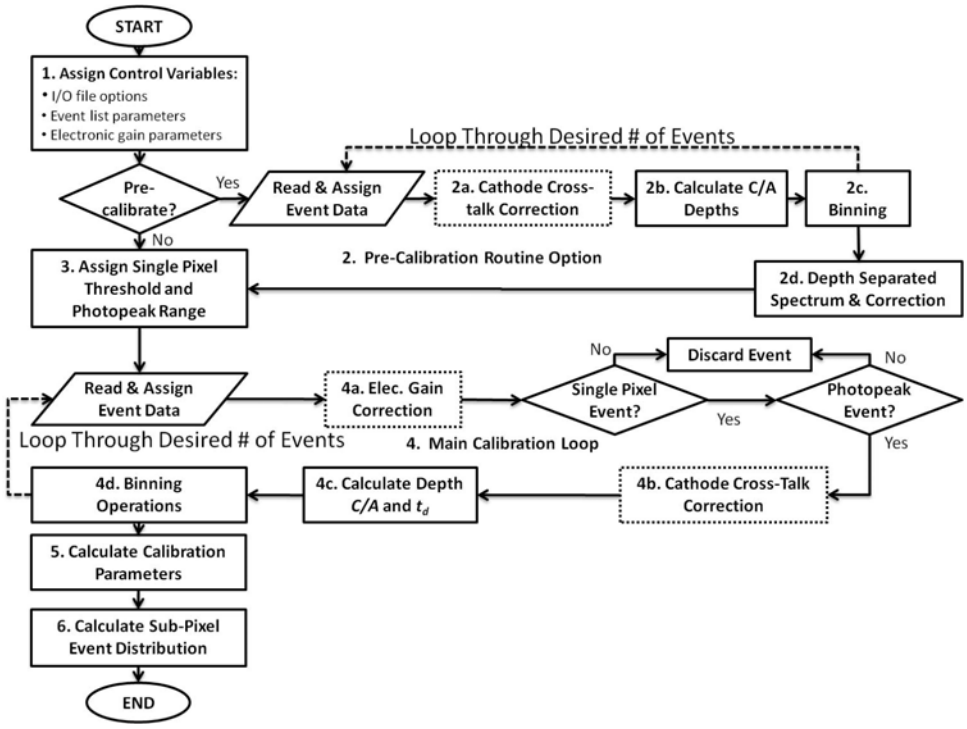

Figure 5.2: The calibration sub-routine is separated into two components, a precalibration loop and the main calibration loop. The main calibration loop analyzes interactions event by event and aggregates various waveform measurements from the signal processing sub-routine and calculates calibration parameters based on depth of interaction and sub-pixel position. The precalibration step must be run if little information is known about the detector response to a particular source.

5.1 Calibration Process

Figure 5.2 is a flowchart that describes the processes of the calibration software for the CZT and HgI−2 detectors used in this study. In the first step, the user is required to set basic input and output file parameters, characteristics of the input data, and optional electronic gain parameters if they have been measured. The next step is an optional pre-calibration sub-routine. If little is known about the measured detector response function to a source, then this step needs to be used. The reason is that the main calibration sub-routine is based on single pixel photopeak events, which requires knowledge of an appropriate multiple pixel energy threshold and photopeak range.

Inside the precalibration sub-routine (step 2), the list of radiation interactions that were measured using the pulse waveform processing routine described in the previous chapter is analyzed event by event. After a single event is opened, an optional step to correct the cathode pulse height amplitude is applied (step 2a). This option must be used when data from the first generation digital readout circuitry is used. This first generation circuitry exhibited a signal cross talk on the cathode signal when charge was collected on specific pixel channels. Certain channels in this circuitry suffer from cross-talk due to improperly shielded signal paths. The phenomenon has been studied in detail and a correction has been developed. The cathode signal cross-talk correction measures this effect and calculates the appropriate correction terms as a function of energy.

Once the cathode signal has been corrected, the depth of interaction can be estimated using the cathode to anode ratio (step 2b), this step is detailed later in section 5.2. Next, in step 2c, the current event being analyzed is binned into a spectrum

with respect to energy and interaction depth. If more events are to be analyzed (as is controlled by the user input in step 1), another event in the list is analyzed and binned accordingly. After a statistically significant number of events have been processed, the events can be corrected using the now calculated depth-dependant energy response (step 2d).

Step 3 is the assignment of the calibration single pixel energy threshold and the photopeak range. The purpose of the single pixel threshold is to filter out events where more than one energy deposition is present. If more than one pixel collects an amount of charge proportional to this threshold energy, the event is not categorized as a single pixel event. Single pixel events are crucial to the general calibration routine because they are the least complex type of interaction. Single pixel events are not corrupted by other iterations in the detector, nor should they experience significant charge sharing. The photopeak range allows for events of a known energy to be used in the calibration.

If the precalibration sub-routine has been run, the single pixel threshold and photopeak range is calculated; however the user is prompted to check the calculations via inspection of a spectrum. The user can then adjust the settings as necessary. The units of these values are not keV, it is channel number which is the unit of the incoming data. If the precalibration routine is not used, then the user must assign these values based on previous knowledge of the processed waveform data.

Step 4 is the main calibration sub-routine. Like the pre-calibration sub-routine, events from the data files generated by the waveform processing module are read one after another. As detailed in section 4.3, the data for a single radiation interaction event contains measurements of the cathode signal, collection pixel signals, and signals from pixels that neighbor a collecting pixel. Pulse amplitude, collection time,

transient pulse height, and tail pulse height are recorded for each waveform. There is also a flag value that is set to 1 if more than one interaction is detected in a single pixel. When this is the case, timing and pulse height information of the interaction are also recorded.

After an event is opened, the step 4a is an optional electronic gain correction. Here, if the gain difference between channels has been measured using a pulser, it can be corrected. Following the initial gain correction, multiple pixel events are discarded using the threshold defined by either the user, pre-calibration step, or the flag value described in the previous paragraph. If an event is not within the photopeak energy range it is also discarded. If a cathode cross-talk calibration is required, it is applied in step 4b. Next, depth is calculated (step 4c). Both cathode to anode ratio and electron drift time are calculated. The details are provided in the next section (5.2). Finally, events are binned by pulse heights and other signal features into various histograms including:

- cathode pulse height,
- cathode to anode ratio vs. electron drift time,
- photopeak energy vs. depth,
- tail amplitude vs. depth,
- transient amplitude vs. depth, and
- transient-tail difference vs.depth.

In step 5, these 3-D histograms are then used to calculate calibration parameters for this particular energy. Details and examples of these functions will be described in section 5.2 and section 5.3. Finally, the sub-pixel position of the interaction is estimated and used to generate a sub-pixel response calibration in step 5. Figure 5.2 does not include the details of these steps. However, the following sections explain

how interaction locations are calculated and how these positions are used to generate calibration functions.

5.2 Interaction Depth Calculations

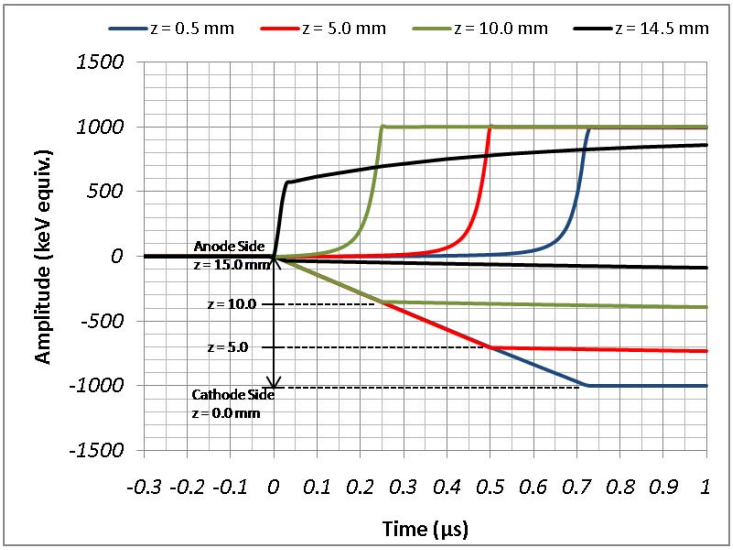

Figure 5.3: Simulated pulse waveforms for the same energy deposition at four different depths in a pixelated CZT detector. The cathode signal is highly dependent on interaction depth (z). The anode signal amplitude only changes significantly near the anode as seen in the pulse from z=14.5 mm.

In this study, there are two methods used to calculate interaction depth. Figure 5.3 compares simulated waveforms of a 1 MeV photon interacting at four different detector depths. In this example, the cathode surface is located at depth $z = 0.0$ mm and the anode surface is at $z = 15.0$ mm. As discussed in chapter II, the charge induced on both cathode and pixel are a function of interaction position. Due to the small pixel effect, the pixel amplitude is nearly constant until an interaction occurs very close to the anode region (black waveform) where the weighting potential changes dramatically. Because the cathode is planar, the cathode signal is highly depth-dependent as can be seen in the difference in amplitude of the four cathode signals. This difference can be exploited to make depth of interaction estimates. An

interaction depth calculation, known as the cathode to anode ratio (CAR), is defined as the ratio

$$CAR = \frac{A_C}{A_P}, \tag{5.1}$$

where A_C is the cathode signal amplitude and A_P is the pixel signal amplitude. For single pixel events, CAR ranges from 0 near the anode to 1 near the cathode.

Another method of measuring depth is to calculate the drift time (t_d) of the electron cloud. In Fig. 5.3, all four cathode-pixel waveform sets start at $t = 0$. However, the time when each electron cloud is collected occurs at $t = 0.03$, 0.25, 0.50, and 0.73 μs respectively. These four times represent t_d. In reality, t_d is calculated as the difference between the pixel waveform collection time and the cathode waveform pulse start time. Figure 5.4 shows an example from experiment. The time pick-off methods described in chapter IV were used to measure the time features. The validity of both methods has recently been demonstrated experimentally using a collimator that forced interactions at known depths [29].

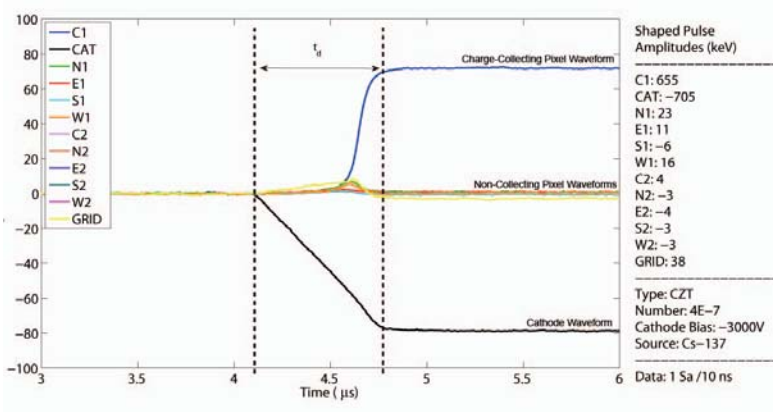

Figure 5.4: An example of how t_d is calculated in experimental waveforms.

Accurate depth estimates allow the detector response to interactions at different depths to be normalized. Figure 5.5 shows the distribution of a 662 keV photopeak centroid (single pixel) as a function of interaction depth. Low depth channels cor-

respond to depths near the anode. In this figure, the pulse height deficit across the detector thickness is caused by two factors. The first factor is the shape of the collecting pixel weighting potential (Sec. 2.2.3). The second factor is charge trapping. An event near the cathode experiences the minimum deficit due to weighting potential but experiences the maximum effect of charge trapping because the charge cloud has to travel the entire thickness of the detector. Events closer to the anode experience less trapping; however, the weighting potential changes rapidly in this region. This effect can be seen for the entire detector response to a Cs-137 source in Fig. 5.6.

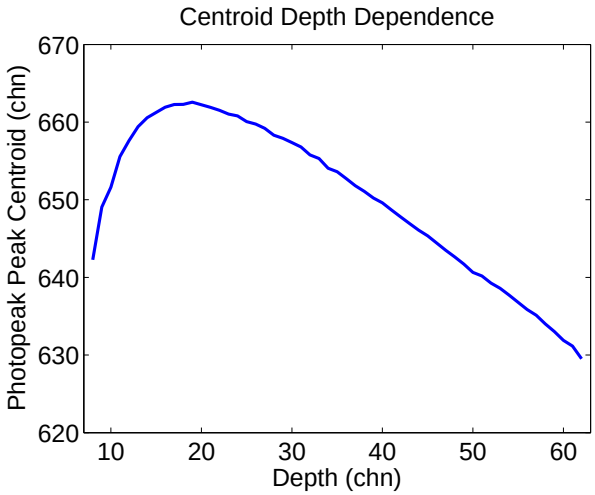

Figure 5.5: The photopeak centroid amplitude as a function of interaction depth in CZT. Low depth numbers correspond to depths near the anode. Large depth numbers correspond to depths near the cathode.

Measurements of weighting potential and trapping-based detector responses can be used to correct the detector response function. Initial measurements of the pulse height deficit as a function of depth serve as a basis for depth calibrations. Later, when events occur at a certain depth, the measured pulse height is corrected using the calibration data. Figure 5.7 is a comparison of the detector response before and after depth correction. The contrast between the cathode and pixel spectra demonstrates the difference between use of planar and pixelated electrodes for a detector that relies

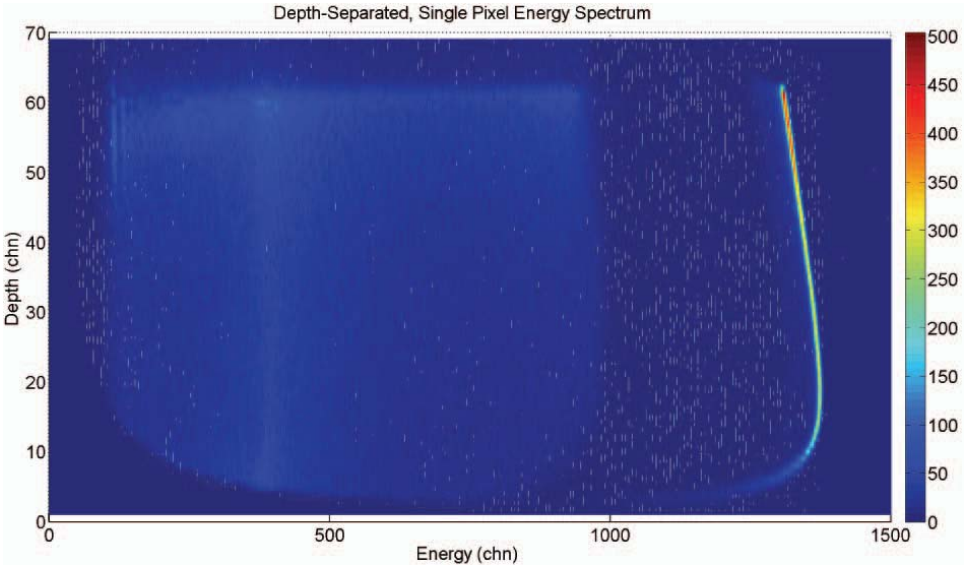

Figure 5.6: A depth separated Cs-137 spectrum for a 15 mm thick CZT detector. Low depth channel numbers correspond to depths near the anode. Large depth channel numbers correspond to depths near the cathode.

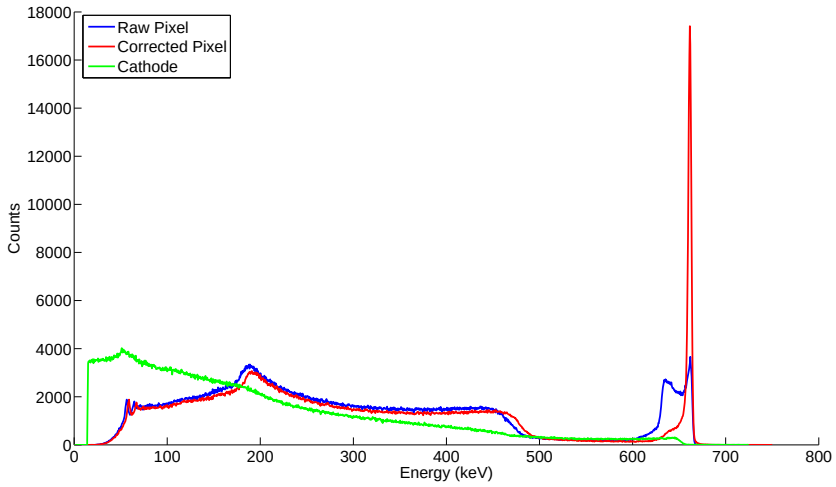

Figure 5.7: A comparison of cathode, raw pixel, and depth-corrected pixel CZT spectra.

on single pixel charge sensing.

5.2.1 Depth Calibrations for Multiple Pixel Events

Currently, the depth of multiple pixel events can only be accurately estimated using the electron drift time method. If one tried to use the cathode to anode ratio, the ratio for individual pixels would be overestimated because the cathode amplitude is larger due to charge induced in multiple locations. This is because the cathode signal amplitude contains charge induced by all the interactions that likely happen at different depths. Using digital signal processing methods, it is possible to deconvolve the cathode waveform using the slight changes in slope that occur at times proportional to the different interaction depths. In this case, depth of interaction could also be estimated by measuring when in time this slope change occurs. Figure 5.8 shows two examples. In both waveform sets there is only one pixel that collects charge, however the change in cathode slope indicates that another interaction occurred elsewhere in the detector. Due to the limited pixel readout in the prototype system this charge deposition was not measured. The change in cathode slope is determined using the method described in sections 4.3.1 and 4.3.2.

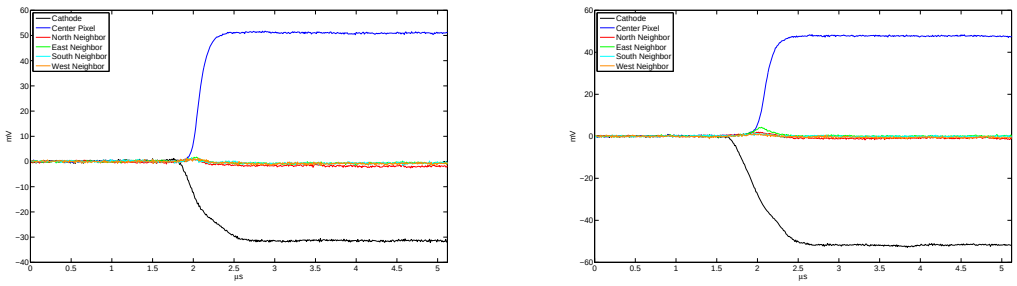

(a) One Slope Change

(b) Two Slope Changes

Figure 5.8: Two examples of discernable slope changes in a cathode waveform.

It is possible to calibrate t_d to CAR. Figure 5.9 shows the results of this calibration sequence for a CZT detector. Single-pixel 662 keV photopeak events from a Cs-137

source were used for the calibrations. Higher depth and time channels correspond to interactions nearer to the cathode surface. The color bar on the right of the figure is an indication of how many events are in each histogram bin.

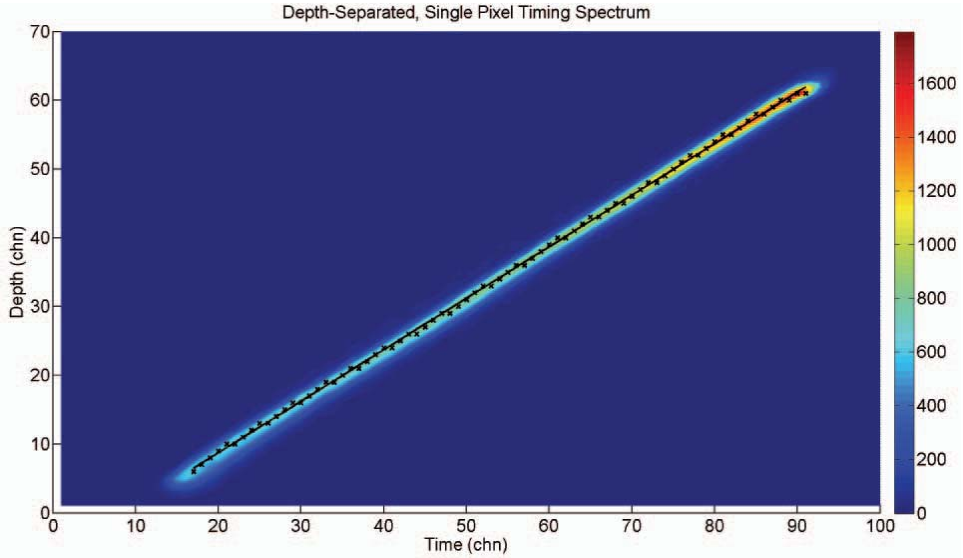

Figure 5.9: A calibration between electron drift time and CAR. In this figure, 100 time channels equals one microsecond. The depth channels correspond to a CAR of 1 scaled by 60. The detector is 15 mm thick CZT.

Since the cathode to anode ratio cannot be used to estimate depths for multiple pixel events, the electron drift time method is used. Figure 5.10 illustrates how the drift time method works for a multiple pixel event. In this simulation example, there are two interactions in the detector. One interaction is located 10 mm from the anode surface and the other is 5 mm from the anode surface. At $t = 0$, the amplitude of the cathode signal starts to fall as charge ionized by the two interactions starts to move. When the first electron cloud is collected by the anode, at $t = 0.25$ μs there is a change in the cathode slope. This collection also corresponds to the end of the electron pulse in the blue pixel signal. As described in the previous section, the difference in time between the blue pixel signal and the cathode start time is proportional to the depth of interaction for one of the events in the multiple-pixel

series. At $t = 0.5$ μs, the second electron cloud is collected. Since this event had a longer electron drift time, the depth of interaction is greater relative to the anode surface. If an interaction occurred on the anode surface, the pulse would occur at $t = 0$. If the interaction occurred on the cathode surface, the pixel pulse would occur at $t = 0.75$ μs. These cases are shown in gray in Fig 5.10. Once the depth of interaction is known for each interaction in a multiple pixel event, the appropriate depth-calibration correction can be applied.

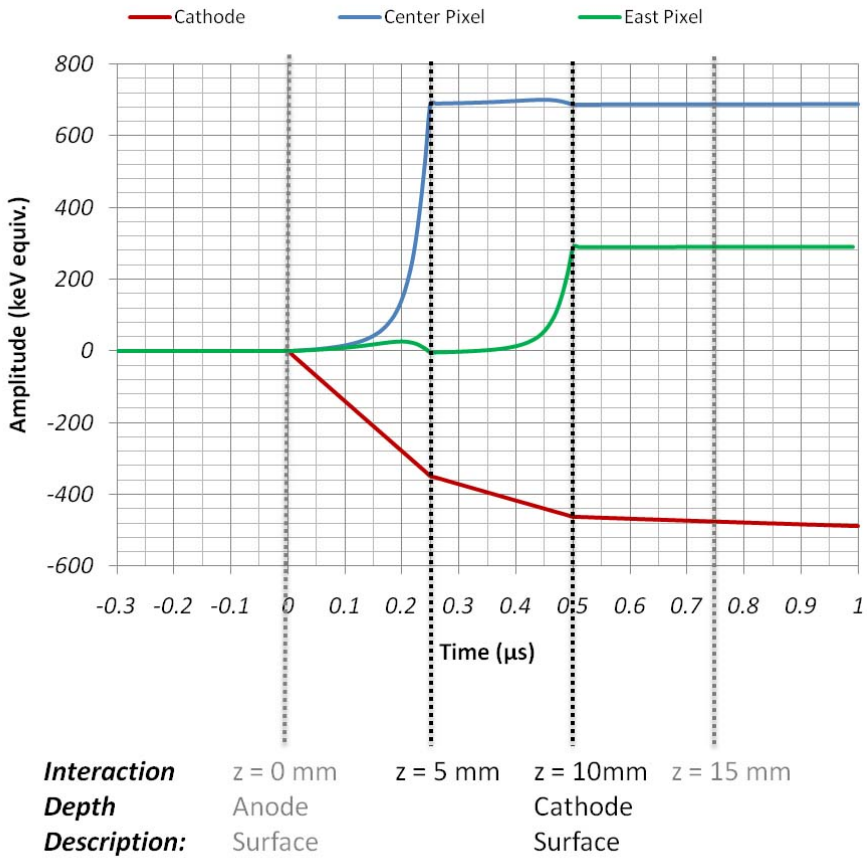

Figure 5.10: The depth of each interaction location in a multiple pixel event can be calculated by measuring the start of the cathode signal and the end of the electron motion in pixel signals. Longer electron drift is proportional to greater interaction depths relative to the anode surface.

5.3 Weighting Potential Cross-Talk Correction

Chapter II described how charge collection in a single pixel affects the waveform of non-collecting pixels. When an interaction occurs near the anode and is collected, a negative amplitude pulse can be observed on non-collecting pixels. The magnitude of this negative pulse for a single energy is related to the pixels proximity to other collecting pixels. During a multiple pixel event, the signal amplitude of all collecting pixels is also affected by the negative amplitude cross-talk signal from all the other collecting pixels. Multiple pixel events that are farther apart in the lateral dimensions of the detector (not the depth dimension), will suffer less cross-talk than events that occur close together.

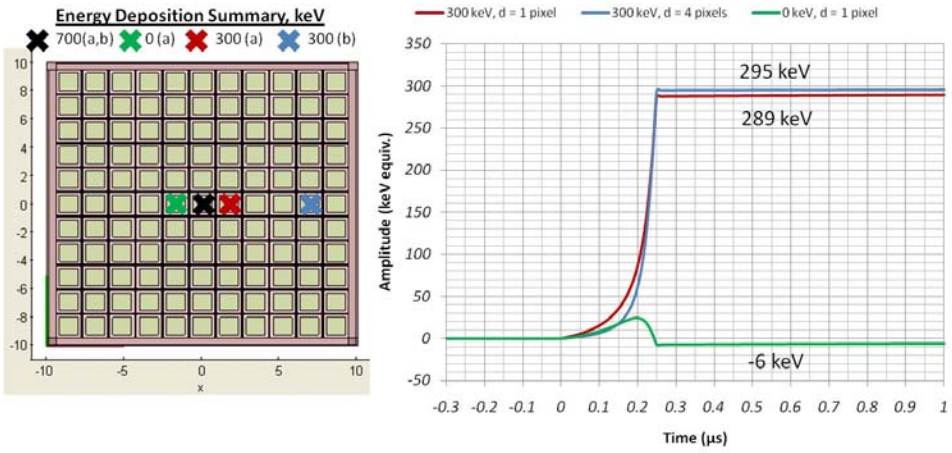

Figure 5.11: A comparison of the effect of weighting potential cross talk on a multiple pixel (black (700 keV) and red (300 keV) X mark locations) event signal for a neighboring pixel interaction and an interaction separated by four pixels (in CZT). The energies and interaction locations are shown in the pixel map on the left for the pixel signals plotted on the right.

Figure 5.11 shows an example of the effect of weighting potential cross-talk for two simulated events. In this example, all interactions occur at a depth 5 mm from the anode surface. The illustration on the left shows where interactions occur in a detector and what the energies are. The first event (a.) includes a 700 keV energy

deposition at the center of the pixel marked by the black X and a 300 keV energy deposition in a neighbor pixel marked with the red X. The second event (b.) has the same energy deposition in the black X pixel, however the 300 keV is deposited four pixels away in the center of the pixel marked by the blue X. The neighbor pixel marked with a green X does not collect charge in either example.

The plot on the left in Fig. 5.11 compares the signals of the amplitude of the 300 keV energy deposition and non-collecting pixel for case a. and b. When the 300 keV is deposited in the pixel that neighbors the 700 keV, the pulse height of the 300 keV interaction is measured as 289 keV. When 300 keV is deposited four pixels away, the measured pulse height of the 300 keV interaction is 295 keV. The amplitude of the neighbor 300 keV deposition is smaller because it is closer to the 700 keV interaction location. The negative amplitude cross talk reduces the neighbor amplitude more than that of the non-neighbor amplitude. For comparison, the cross talk of a non collecting neighbor pixel can be viewed in the -6 keV amplitude green waveform. Cross-talk from the 300 keV energy depositions also affect the amplitude of the 700 keV interaction, but are not included to maintain the simplicity of this plot.

In order to generate a calibration for weighting potential cross talk, the cross-talk amplitude must be calculated as a function of energy, interaction depth, and separation distance. Then, when a certain amount of energy is deposited in any pixel at a certain depth, the expected weighting potential cross-talk on other pixels can be used to correct energy deposition measurements in other pixels. In this study, the task was simplified by analyzing and correcting weighting potential cross talk in 5 neighboring pixels or two non-neighbor pixels and at energies between 30 and 662 keV. Because of this simplification, it was possible to calculate an energy and depth dependant cross-talk correction function for each pixel. If all detector pixels are to

be used, a more general cross talk function based on energy, depth, and interaction spacing distance can be used. When a multiple pixel interaction takes place, the two separate charge clouds induce charge on all the other pixels, including the pixels where the other charge cloud is located. If the effect of the charge induction from the other charge clouds is not included, the final calculated energy of the separate charge depositions will be smaller. If the proper correction is applied, the separate charge depositions can be added together without significant losses in energy resolution.

Measurements of the amplitude of the tail signal induced on non-collecting pixels is used for the weighting potential cross-talk correction. To make this calibration, the charge induced on non-collecting pixels is measured as a function of the energy deposition and depth of the interaction in the collecting pixel. Figure 5.12 is a collection of induced charge distributions (waveform tail amplitude after electron collection) for different pixels relative to a collecting pixel. Tail amplitude was calculated using the method described in chapter IV. In reality, the amplitude of most tail signals is negative; however, they are plotted as positive amplitudes in this figure. To produce this data, an experiment was conducted in which waveforms from non-collecting pixels were analyzed when 662 keV photopeak events were detected in the collecting pixel.

Figure 5.12 shows the tail amplitude distribution integrated across all interaction depths for neighbor and non-neighbor pixels according to the color coded pixel diagram. According to the induced charge theory for non-collecting pixels in chapter II, neighbor pixels experience a higher degree of charge induction. For pixels located farther away from a collecting pixel (i.e. the interaction position) the amount of charge induced decreases. The magnitude of the final charge induced on a non-collecting pixel is the key weighting potential cross-talk calibration parameter and is necessary

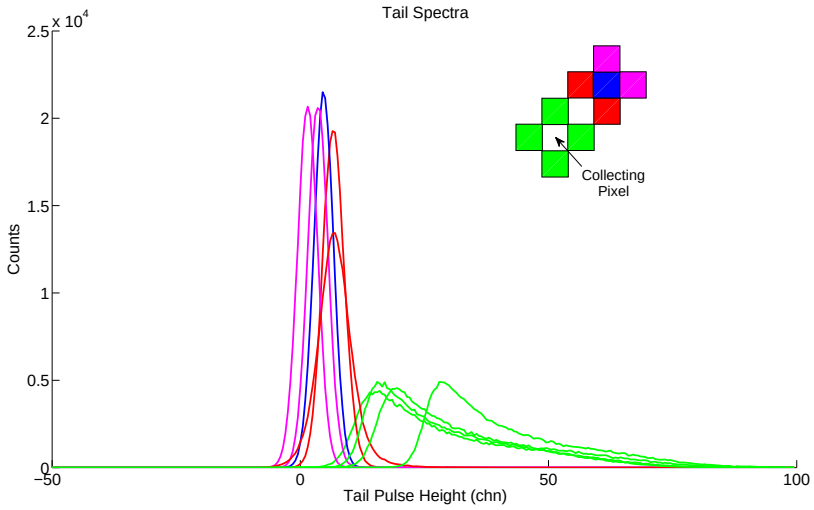

Figure 5.12: The distribution of charge induced in the tail region of a pulse waveform for neighbor and non-neighbor pixels relative to a collecting pixel. Events in the collecting pixel were from a 662 keV photopeak in CZT.

for the calculation of the total energy deposited during an event.

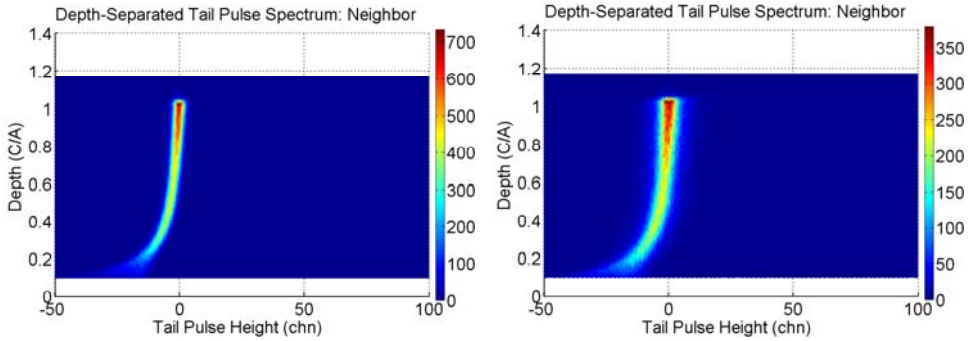

(a) (b)

Figure 5.13: Tail amplitude vs. depth for neighbor pixels. Events in the collecting pixel were from a 662 keV photopeak in CZT.

Figure 5.13 shows the amplitude of the tail pulse as a function of depth for two of the four neighbor pixels indicated. The magnitude of the tail amplitude increases as events occur closer to the anode. Figure 5.14 shows the depth distribution of two non-neighbor pixels. The magnitude of the tail amplitude is smaller for non-neighbor pixels because the non-neighbor pixels are farther away from the charge motion. The difference is most significant at depths near to the anode (a low C/A).

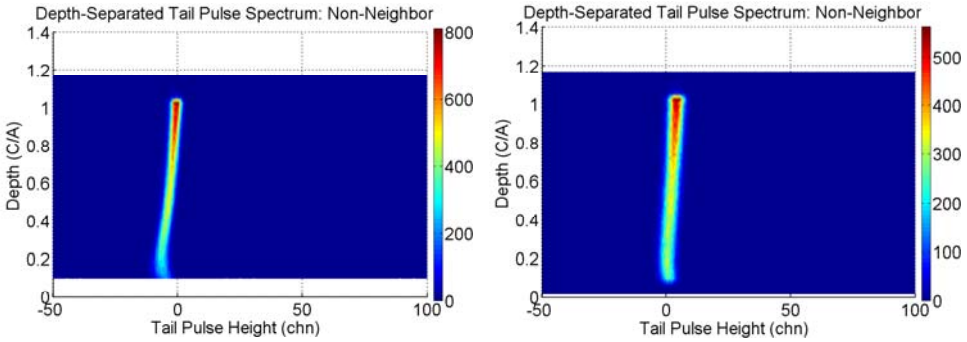

(a) (b)

Figure 5.14: Tail amplitude vs. depth for non-neighbor pixels. Events in the collecting pixel were from a 662 keV photopeak in CZT.

5.4 Sub-Pixel Position Calculation

5.4.1 Transient Signal Calibrations

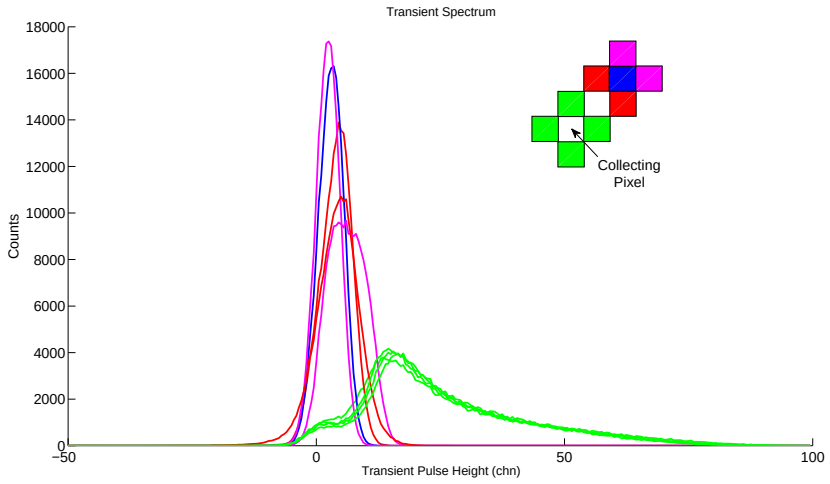

Figure 5.15: The distribution of the transient peak amplitude for various pixels relative to a collecting pixel.

Chapter II described how "transient signals" are formed in a pixelated detector. These short, positive amplitude pulses are formed when charge passes near neighboring pixels, but is not collected by one of the pixels. Figure 5.15 shows the distribution of transient peak amplitude according to the color code in the pixel diagram. The transient amplitude is defined as the maximum amplitude of the filtered transient signal. Figures 5.16 and 5.17 show the depth dependence of these distributions.

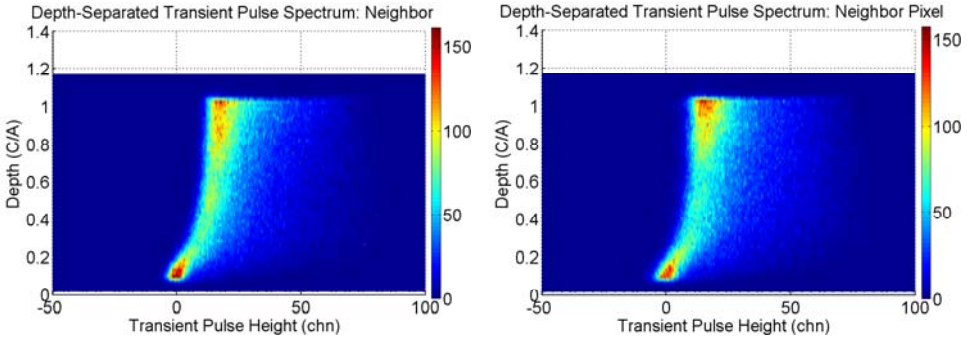

(a) (b)

Figure 5.16: Transient amplitude vs. depth for neighbor pixels.

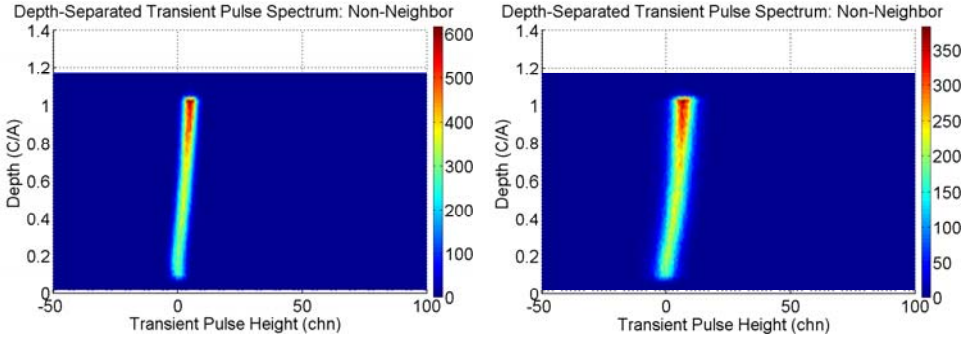

(a) (b)

Figure 5.17: Transient amplitude vs. depth for non-neighbor pixels.

For events near the anode, the transient amplitudes can have a negative amplitude due to the same reason the tail is more negative near the anode (section 2.3). This effect can be canceled out if the tail value is subtracted from the transient peak amplitude event by event. Figure 5.18 shows the corrected transient amplitude depth distribution of a neighbor and non-neighbor pixel. Given an interaction distribution under a single pixel, the transient-tail difference distribution for each neighbor needs to be normalized so that sub-pixel position estimates can be calculated easily.

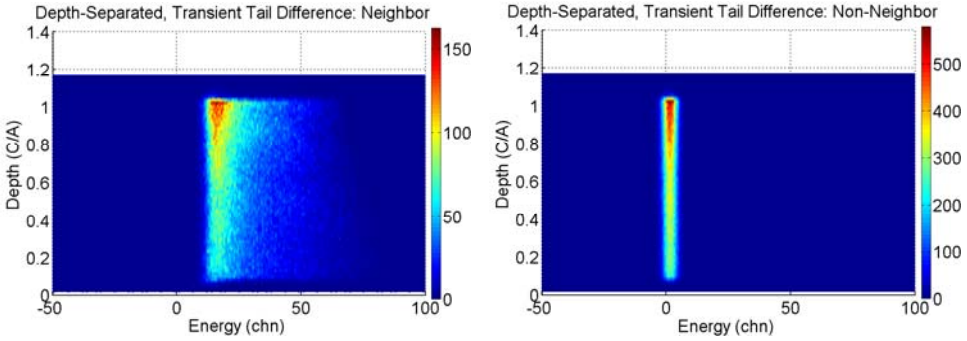

(a) Neighbor Pixel

(b) Non-Neighbor Pixel

Figure 5.18: The calculated difference between transient and tail amplitudes as a function of depth. This new value can then be used as a depth-independent measure of the transient peak amplitude. One channel is equal to roughly 0.5 keV.

5.4.2 Sub Pixel Position Estimation Method

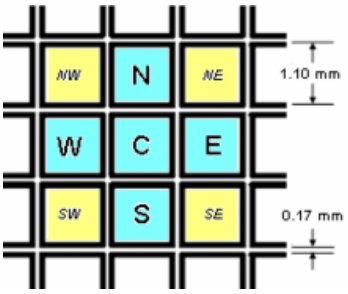

Figure 5.19: The purpose of this figure is to explain how pixels are labeled in this study. The center pixel that collects charge is surrounded by neighbor pixels labeled according to their relative position. This figure also shows the pixelated anode design of 3D HgI_2 detectors uses a pixel area of 1.1x1.1 mm^2 with 0.17 mm spacing. The layout of a CZT anode is similar. Details are given in chapter III.

As described in chapter II, the amplitude of a neighbor transient signal depends on where the interaction takes place in the collecting pixel. Figure 5.19 serves as a starting point to understand the method of sub-pixel position estimation. The pixel labeled C is assumed to be the collecting pixel. The neighboring pixels are labeled 'north', 'north east', 'east', and so on. If the transient signal from 'north' and 'south' pixels are measured, their relative amplitude can be used in algorithms to estimate the y position of interaction within the center pixel. The signals measured on 'east' and 'west' allow an estimates of x position. The corner pixels contain both x and y position information.

The maximum transient amplitude occurs when an electron cloud is created (and then transported) on the side of the collecting pixel that is closest to this particular neighbor. An example of this phenomenon is seen in the west neighbor signal in Fig 5.20. The minimum transient amplitude occurs when the interaction occurs on the opposite side of collecting pixel as seen in the east neighbor signal in Fig 5.20. A uniform electron cloud with a centroid in the middle of a pixel would induce identical transient signals on its four cardinal neighbors. When the centroid of the electron

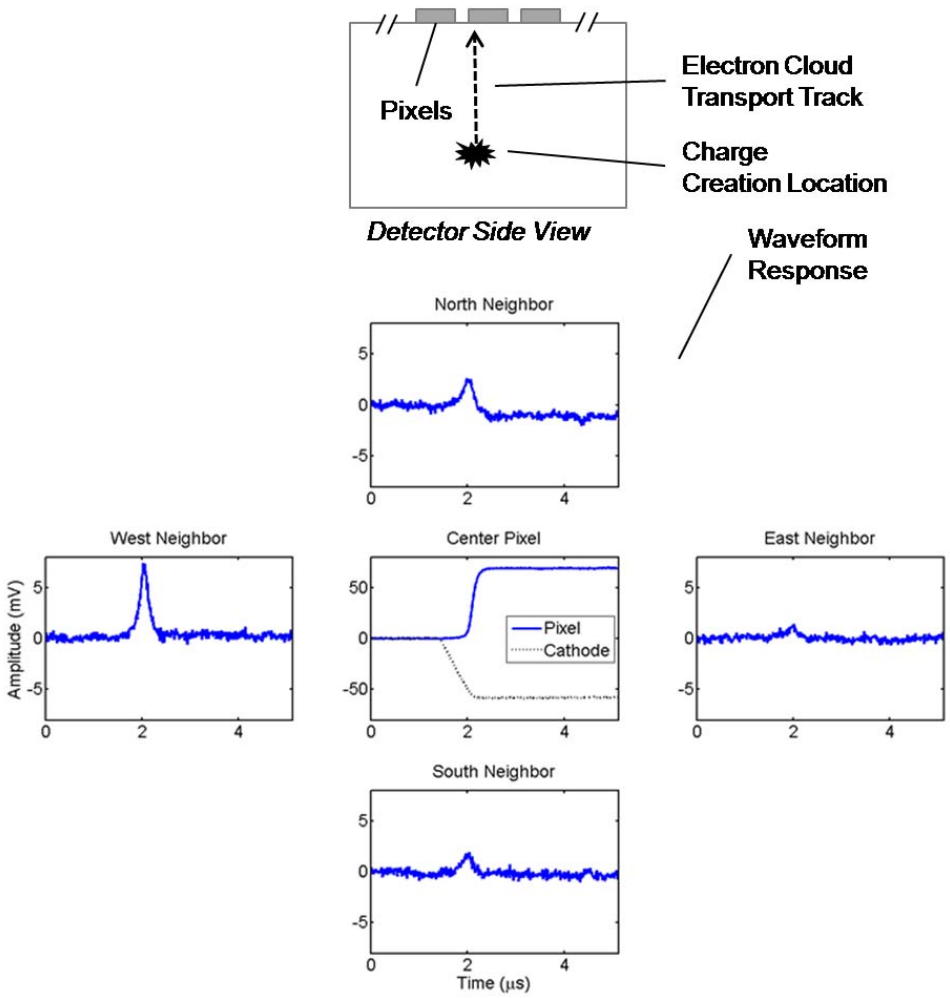

Figure 5.20: The signals on pixels that neighbor a collecting pixel contain lateral interaction position information. The data is from a CZT detector.

cloud is not in the center of the pixel, the transient signals from neighbors nearest the centroid will have larger amplitudes than their opposing neighbors.

The difference in relative transient signal height is used to reconstruct sub-pixel position from the acquired waveforms. There are different ways to use these transient pulse heights, the details of which can be found in Ref. [69]. The method used in this study is the side neighbor ratio method. For example, the sub pixel position ratio for the x lateral dimension R_x is defined as

$$R_x = \frac{s_E - s_W}{s_E + s_W}, \tag{5.2}$$

where s_E and s_W are the corrected transient pulse height amplitudes from the east and west neighbor. Likewise, using the north and south pixels, the ratio for the y lateral dimension R_y is defined as

$$R_y = \frac{s_N - s_S}{s_N + s_S}. \tag{5.3}$$

This algorithm is useful because it distributes all ratio calculations within the range of -1 to 1. The linearity of this model has been demonstrated using simulation and experimental results in Ref. [69]. Figure 5.21 shows the distribution of photopeak events under a single pixel distribution. Figures 5.21 (a) and 5.21 (b) illustrate two different methods to bin sub-pixel interaction positions. The dashed line in Fig. 5.21 (b) represents the estimate of the pixel boundary and is calculated using the distribution in Fig. 5.21 (a). The binning in Fig. 5.21 (b) is a result of the measured position resolution of 260 μm FWHM at 662 keV [69].

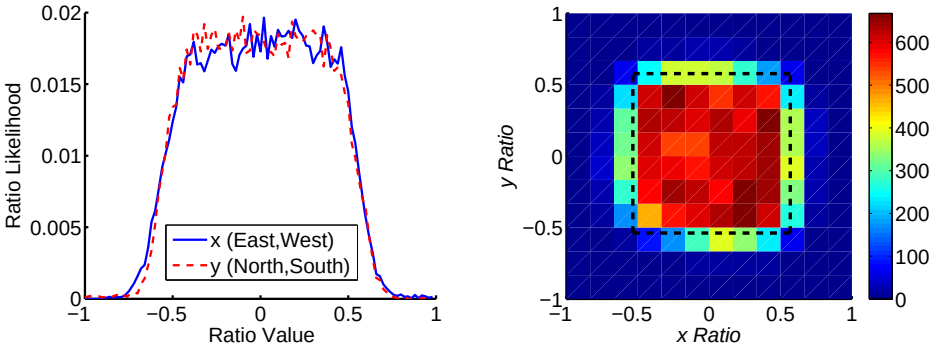

Figure 5.21: Sub pixel position resolution in CZT detectors using a Cs-137 source. Two methods of plotting the sub-pixel interaction in a single pixel. The dashed line in (b) represents the pixel boundary. The color bar in (b) represents the number of interactions in that specific sub-pixel region.

5.4.3 Sub Pixel Calibrations

The detector response can now be measured for different depths and sub-pixel positions. This enables corrections of the detector response with sub-pixel precision.

In this way, weighting potential, charge trapping and loss to gap regions, and material non-uniformities can all be calibrated just as the depth-dependent response was calibrated in the past. Figure 5.22 shows the 662 keV photopeak amplitude for the sub-pixel distribution shown in Fig. 5.21. Events that occur in the middle of the pixel have a higher amplitude than events near the edge. Events near the pixel edge have a higher chance of losing a fraction of its electron cloud. Events near the edge also are affected by a slightly smaller weighting potential than events near the center of the pixel. The channel numbers representing energy in this figure (color coded) are equal to roughly one half keV.

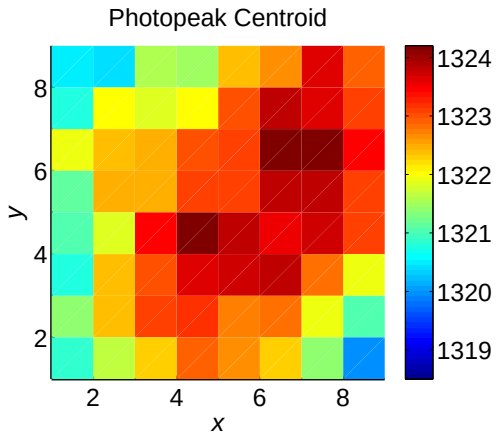

Figure 5.22: Photopeak amplitude for different sub-pixel positions in CZT using 662 keV photopeak events.

Figure 5.23 shows FWHM in % at 662 keV for the sub-pixel distribution bins. This distribution is significant because it is rather consistent throughout the entire pixel. This demonstrates that while the detector response may not be uniform throughout a pixel, the response of each non-uniform discrete region still exhibits excellent energy resolution.

This result can also be seen in Fig. 5.24 which compares the photopeak spectrum for three cases: no sub-pixel information (red), events calculated to be in the center of the pixel (green), and sub-pixel position calibration (blue). The best resolution

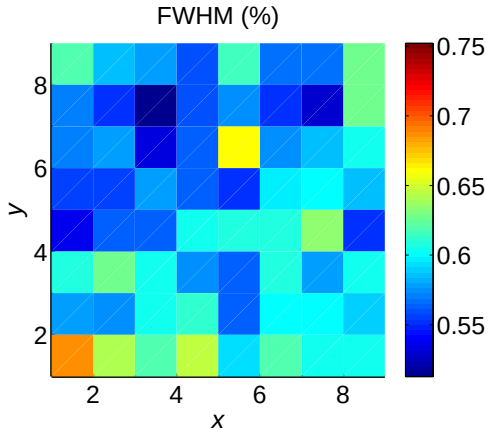

Figure 5.23: Photopeak resolution (% FWHM at 662 keV) for different sub-pixel positions in CZT.

(FWHM at 662 keV), from the events in the center of the pixel, is 0.58%. The resolution of the sub-pixel position corrected spectrum is 0.62 %. Both spectra that take advantage of sub-pixel information have better resolution than the spectrum without any correction (0.65%).

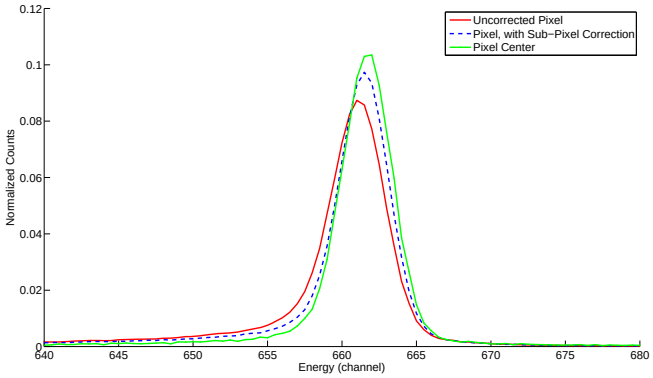

Figure 5.24: A comparison of 662 keV photopeaks for methods that rely on sub-pixel position resolution. In this example, the best resolution occurs for event occurring in the central sub-pixel region. If all the sub-pixel regions of the single pixel are calibrated the resolution is better than the raw, uncalibrated photopeak.

CHAPTER VI

Event Classification and Reconstruction

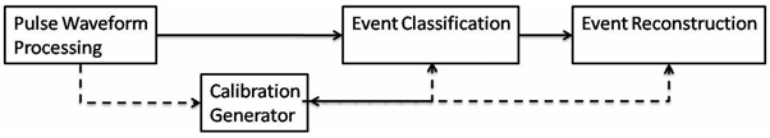

Figure 6.1: Chapter VI covers the final two components of the event classification suite: event classification and event reconstruction.

The final two stages of the event processing procedure are event classification and event reconstruction. The main focus of this chapter is event classification. Event reconstruction is straightforward once events are properly calibrated and classified. Therefore, this subroutine is briefly discussed in this chapter.

Assuming appropriate calibration parameters have been calculated, the event classification module analyzes data from the waveform processing routine resulting in a final data-form from which accurate reconstructions can be made. The data-form that is output by the event classification routine includes an event class code as well as the energy and in most cases, sub-pixel positions of each energy deposition location. Since detector response and weighting potential cross-talk calibrations have already been applied, multiple interaction events can be summed together and spectra constructed. Position information and energy for multiple interaction events are preserved in the case of Compton scatter for use in Compton imaging algorithms.

This chapter is divided into two sections. The first section explains the general

process of the event classification and how it is implemented in software. Waveform examples are used to demonstrate how the software makes decisions. The second section presents experiments and simulations that have been conducted to validate the event classification algorithms. These verifications were made using three separate methods: waveform simulation, a collimator experiment, and an experiment that uses sub-pixel position information.

6.1 Event Classification Procedure

Before discussing the details of the event classification procedure, it is important to consider the data that is passed into the classification routine. The waveform processor routine described in chapter IV processed "events" from a 3D detector. However, these events were in the form of waveform sets and were caused by anything that triggered the waveform acquisition system. If the cathode pulse-pile up discrimination method described in section 4.2.2 is used, then most of the waveform data entering the event classification module can be assumed to be caused by a single incident photon. It is critical to separate events that contain more than one source photon. Energy thresholds between 20 and 30 keV were used to discriminate noise and low-energy events.

If calibration parameters for a detector have already been calculated, the event classification function can be called by the pulse waveform processing module described in chapter IV. A classification is made as each event is processed. Figure 6.2 is a flowchart that illustrates the event classification procedure. Like the other subroutines, the first step is initialization of the software controls including file options, parameters of the data being transferred (such as calibration source information, number of pixels included), detector specifications, as well as thresholds and other

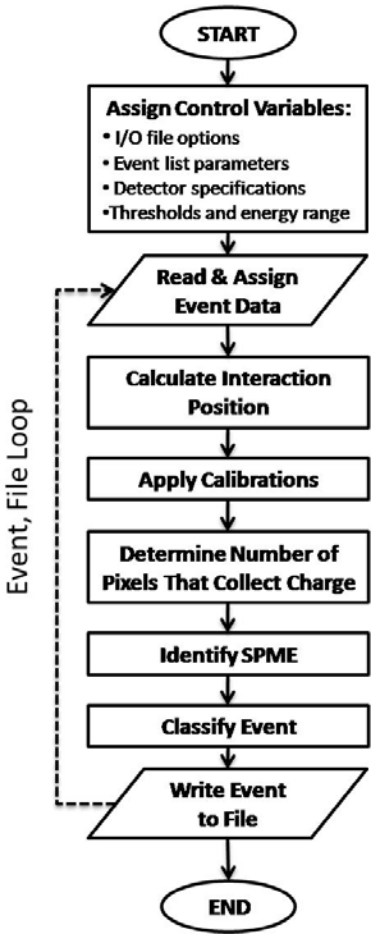

Figure 6.2: The event classification software subroutine consists of four modules. The event classification step applies system calibrations and determines which interaction types are most likely on an event by event basis.

energy-specific decision making variables. The next step includes the loop where data from the waveform processing routine is calibrated and then processed event by event. A single event entering the routine contains information for each signal channel involved in the interaction history, including channels that exhibit charge collection, neighbor pixels, and the cathode channel. The information pertaining to the cathode channel includes measurements of the cathode pulse start time, and the amplitude of the cathode pulse. The information for each pixel is more complex. For each pixel signal, the following measurements are passed to the event classification algorithm:

- pixel number, which is needed for the calibration step,
- pulse amplitude, which is the primary energy deposition measurement,
- electron collection time, which is used to calculate drift time,
- transient peak amplitude, which is used for sub-pixel measurements,
- tail amplitude, which is used to discern charge collection and is needed for sub-pixel measurements, and a
- single-pixel multiple-event (SPME) flag, which alerts the algorithm that a multiple site interaction has occurred in a single pixel.

The first step in the classification process is the calculation of interaction position based on the uncalibrated incoming data. The calculated position is not the physical interaction position because the data has not yet been calibrated. However, the uncalibrated position is still useful in applying the response calibrations that were described in chapter V. Pixels with pulse heights above a threshold charge collection are used as reference "trigger" pixels. Sub-pixel position information is calculated only for these trigger pixels[1]. Sub-pixel calculations can be made for most events with a few exceptions in which the implemented sub-pixel algorithm is not advanced

[1]Though later, subsequent sub-pixel estimates can be made if charge sharing is suspected and charge collection has been sensed (below the original threshold) in the neighbor pixel.

enough to process[2]. These cases include multiple interactions in a single pixel, interactions in neighbor pixels that "wash-out" transient signals, and events on the edge of the detector. If a sub-pixel position cannot be calculated, the event is calibrated without sub-pixel precision.

After calibrations are applied, the event classification process can begin. The first two steps determine how many charge clouds or charge cloud segments have been detected. Identification of SPME is quite easy since it has already been flagged. The details of charge sensing using waveforms is presented in the next section (6.1.1).

To better understand the classification step, it is helpful to summarize the different event possibilities. Figures 6.3 - 6.6 serve as an illustration of the events that need to be classified in both CZT and HgI_2 detectors. These plots were generated using unclassified events occurring in a single depth of a single pixel. Depth estimates were made using the cathode to anode ratio. Analyzing a single depth helps minimize the complexities of depth-dependent energy responses[3]. The source that is measured is Cs-137. These plots show the pulse height distribution of a collecting pixel verses the tail amplitude of one of its neighbor and one of its non-neighbor pixels. Each dot represents an event. The multiple pixel event threshold used in this experiment is 25 keV.

Figure 6.3 compares the pulse height of a neighbor and non-neighbor pixel versus the collecting pixel's pulse height. To simplify the comparison, only events from a single interaction depth are shown. Since only single pixel events have been included, the pulse height on both non-collecting pixels is expected to be low. For the neighbor pixel events (blue dots), pulse height should only be positive when charge is collected

[2]Although, the formalism for these cases is described theoretically in Ref. [69]

[3]Though beyond the scope of this thesis, it is fascinating to look at these types of plots as a function of depth and sub-pixel position. For example, escape peaks are more common near the edge of the detector and the edge of pixels. Backscatter peaks are more common near surfaces. Not surprisingly, charge sharing is more prevalent near the edge of pixels, etc.

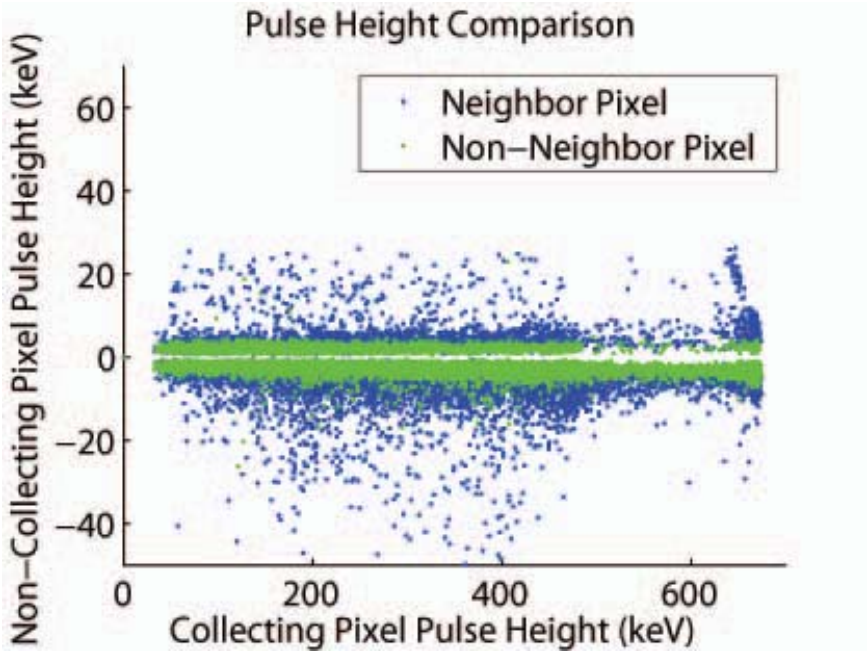

Figure 6.3: The pulse height of a collecting pixel plotted against the pulse height in neighbor and non-neighbor pixel for single pixel events at a single interaction depth in CZT.

on the neighbor (below the multiple pixel event threshold) or the noise level results in a positive amplitude measurement.

Negative amplitude neighbor pulse heights in Fig. 6.3 are common for single pixel events in the collecting pixel that occur near the anode surface. This is the effect of weighting potential cross talk. The negative pulse amplitudes of the non neighbor pixel are smaller in magnitude because the non-neighbor pixel is farther away from the main charge collection pixel than the neighbor pixel. If a weighting potential cross talk calibration was applied to this data, a different correction factor would be added to each pixel according to this specific depth, as well as the energy collected in the other collecting pixels. In this case, the amplitude of the collecting pixel pulse height would not change significantly because the amount of charge collected by the neighbor or non neighbor pixels is below 25 keV.

The events in the photopeak region of Fig. 6.4 correspond to a maximum neighbor

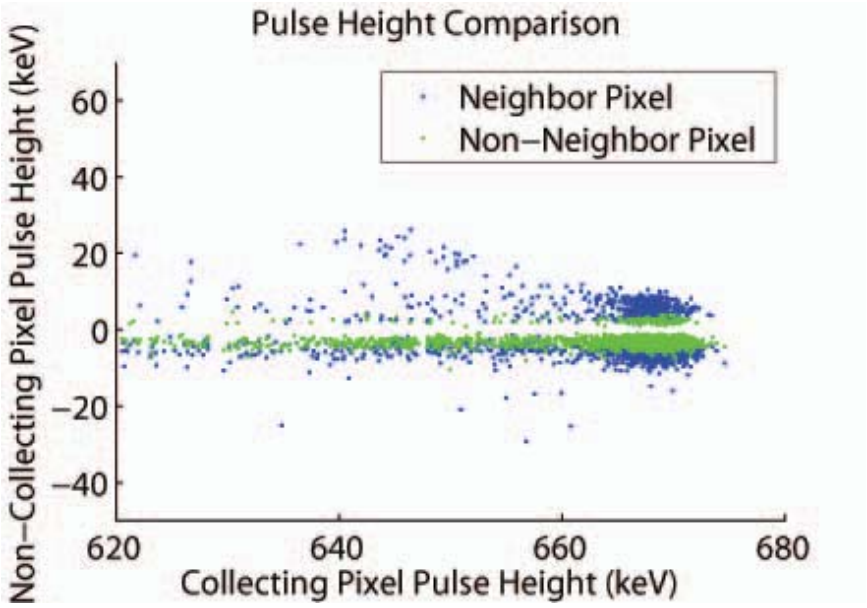

Figure 6.4: A close-up of the photopeak region in Fig. 6.3

pixel pulse height of roughly 12 keV. This amplitude is about 7 keV higher than the maximum[4] amplitude of the non-neighbor pixel (green dots) in Fig. 6.4 which is below 5 keV. Why is the maximum amplitude of a neighbor pixel larger than that of a non-neighbor pixel? First, it is important to recognize the effect of weighting potential cross-talk induced on both the neighbor and non-neighbor pixels. In this figure, weighting potential cross-talk has not been corrected. This is evident in the observation that negative-amplitude neighbor pixel pulse heights in the photopeak region (between 660 and 680 keV) are lower than non-neighbor negative-amplitude pulse heights. This observation leads to the conclusion that the same amount of charge collected in either a collecting or non-collecting pixel would have different pulse heights due to the weighing potential cross talk. Specifically, the neighbor pixel would have a smaller pulse height than the non-neighbor because the cross-talk is more negative for the neighbor pixel. This conclusion is important since the positive amplitude neighbor pixel amplitudes in Fig. 6.4 are still larger than

[4]Not including the few events above 10 keV which are due to Compton scattering.

the non-neighbor positive amplitudes. The difference in measured noise for each of the pixels is not enough to explain this difference. The remaining explanations are charge sharing and characteristic X-ray escape. X-ray escape is unlikely since the most probably X-ray in CZT are closer to 30 keV[5] and lower energy X-rays are less likely to escape the detection volume beneath a single pixel.

Based on the comparison of the *supposed* non-collecting pixels in these two figures, the effect of these unclassified phenomena in the photopeak region is expected to have a maximum amplitude of about 12 keV which is about 7 keV higher than the noise level established in Fig. 6.4. At this depth, the weighting potential cross-talk calibration pushes the difference to about 9 keV. This is not to say that charge sharing (or less likely, X-ray escape) can only contribute 12 keV to a neighbor. Instead, in this example, an event under a single pixel can share as much as 12 keV with a neighbor and still be found in the photopeak region. If one follows the low energy tail of the photopeak from right to left, one can see a trend in the neighbor pixel amplitude that increases in energy (this is easier to see in Fig.6.3. This can be due to two factors, charge sharing and characteristic X-ray escape. Since the energy threshold for single pixel events in this figure is 25 keV, most of the events in this trend are not expected to be due to X-rays.

Instead, X-rays escaping to a neighbor would be expected to be located near the photopeak in Fig. 6.5 (a). The two plots in Fig. 6.5 show the amplitude of neighbor and non-neighbor pixels for two-pixel events. Multiple pixel interactions include Compton scattering out of or into the center pixel volume, followed by absorption of the scattered photon in the opposite pixel. The same is true for scatter-scatter events between neighbors. X-rays can also escape the center pixel volume and be

[5]Table 2.1 lists the possible X-rays for CZT and HgI_2. Even when a weighting potential cross talk calibration is applied, at this energy, most of the x-ray events will be categorized as multiple pixel events since the threshold is 25 keV. Zinc X-rays are close to 9 keV, though the zinc concentration is only 0.05. L shell X-rays are all below 4 keV.

absorbed in a neighbor. This effect of X-ray escape is much more prominent in HgI_2 as seen in figure 6.6. The diagonal trend that bounds the maximum amplitude in either second pixel indicates where the sum of center and second pixel equals the full 662 keV energy deposition.

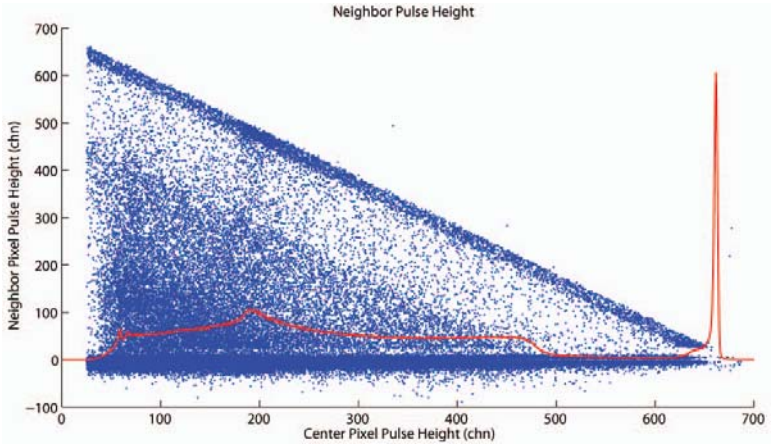

(a) Neighbor Pixel

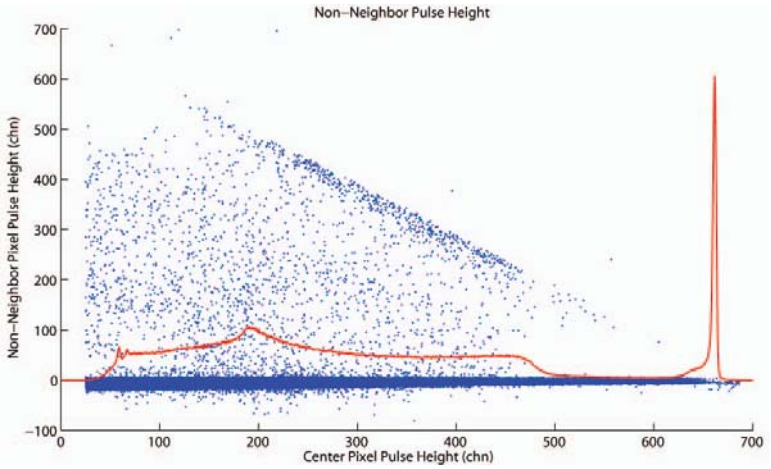

(b) Non-Neighbor Pixel

Figure 6.5: The pulse height of a collecting pixel plotted against the pulse height in neighbor and non-neighbor pixel for multiple pixel events in CZT.

Table 6.7 summarizes classification criteria for full energy deposition photon interactions in the 30 keV to 3 MeV energy range. These criteria are based on the event signatures developed in chapter II. The table also includes criteria for identifying charge sharing. The special energy requirement category is a key parameter in clas-

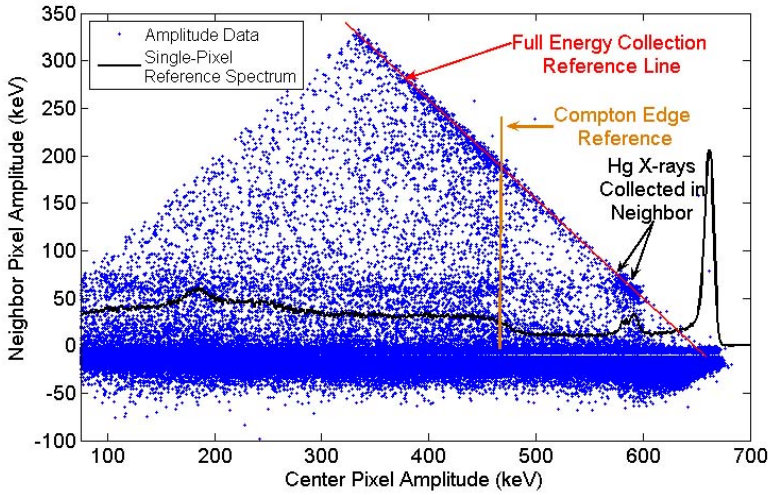

Figure 6.6: The pulse height of a collecting pixel plotted against the pulse height in a neighbor pixel for HgI_2. In this example, events are excluded where the neighbor pixel amplitude are greater than the center pixel amplitude.

Interaction Classification	Minimum Characteristic Energy Detection Requirement		Minimum Interaction Position Requirement		Additional Evidence
	Source Info.	No Source Info.	Source Info.	No Source Info.	
Photoelectric Absorption	full energy deposition	detector material X-ray detected	none	X-ray interacts in distinct position	expected X-ray range in material
Pair Production	one 511 keV deposition (single or multiple site) plus at least one other energy deposition		interactions must occur in distinct positions		two 511 keV depositions aligned with an energy deposition between
Compton Scatter	none				confidence is higher for known source
Charge Sharing	none		multiple charge collections in neighboring pixels		sub-pixel interaction position on common edge

Figure 6.7: A summary of the classification criteria used to separate gamma ray interaction types in pixelated detectors.

sifying photoelectric absorption and pair production events since these interactions are associated with secondary photons with known energies. It is important to note that these "special energy" photons do not need to deposit all of their energy in one location. If the sum of secondary energy deposited equals 511 keV or the energy of a characteristic X-ray, then classification is still possible. However, since the energy of the characteristic X-rays is low, they are unlikely to scatter.

The minimum interaction position requirement considers the case of multiple site

interactions which includes all the possible event types. For photoelectric absorption, the location at which the X-ray is deposited does not provide further evidence of the event type. However, if the X-ray were to escape to a position in the detector that is unlikely due to its low energy, then the likelihood that the event is a scatter would increase. For pair production events, if only two energy depositions are identified, there is no spatial interaction distribution that is of value. However, if both 511 keV annihilation photons deposit their energy, then three of the energy deposition locations should lie on the same axis. Compton scattering requires that energy is deposited in two separate locations; however, this is sometimes difficult to separate from charge sharing events. The distinction between charge sharing events is based on knowledge of the sub-pixel position of the interaction. If events are located on the common edge between two pixels, then charge sharing is the most likely case.

Signatures are listed for the case of known source energy and position, and with not prior source knowledge. The case of known souce energy and position also assumes that the source to backgroudn signal to noise ratio is significantly high. The background signal can be due to same or similar energy photons from background sources or Compton continuum events from higher energy photons in the source or background sources. In scenarios where the source signal to noise ratio is low, the value of source information is limited. This source information known scenario also assumes that the photon has not lost energy before interacting in the detector. If source information is known, the criteria of the unknown source case are still valid and provide additional confidence. The next sections explore the process of event classification using experimental data.

6.1.1 Pixel Electron Collection Detection

The first step of event classification is the determination of how many pixels collect charge. As described in section 5.3, the signature of charge collection is measurement of the tail amplitude above its expected value for a given interaction position. Figure 6.8 compares experimental waveforms in CZT for single pixel interactions near the anode and cathode.

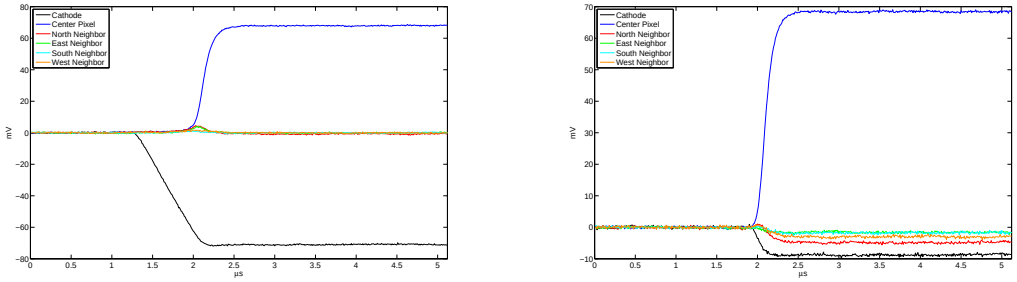

(a) Single Pixel Event Near Cathode

(b) Single Pixel Event Near Anode

Figure 6.8: Single Pixel Event: A 662 keV equivalent single pixel event near the cathode compared to an event near the anode. Charge is only collected in a single pixel.

Accurate identification of charge collection can immediately improve the response function for a particular energy. Figure 6.9 shows a single pixel 662 keV photopeak collected with a CZT detector. The blue line is before the event classification procedure, the red line is after. Resolution improves from 0.81 % FWHM to 0.78 %. Event classification removes events in the low energy tail of the photopeak. These events suffer a signal deficit due to electrons collected in neighbor pixels. Event classification accurately identifies the shared charge even if it below the multiple pixel energy threshold. When these charge sharing events are corrected, a sharper photopeak is observed. Not only is resolution better, but there are 30% more photopeak counts which cannot be seen in this area-normalized figure. These "missing" counts were previously incorrectly identified as multiple-pixel events.

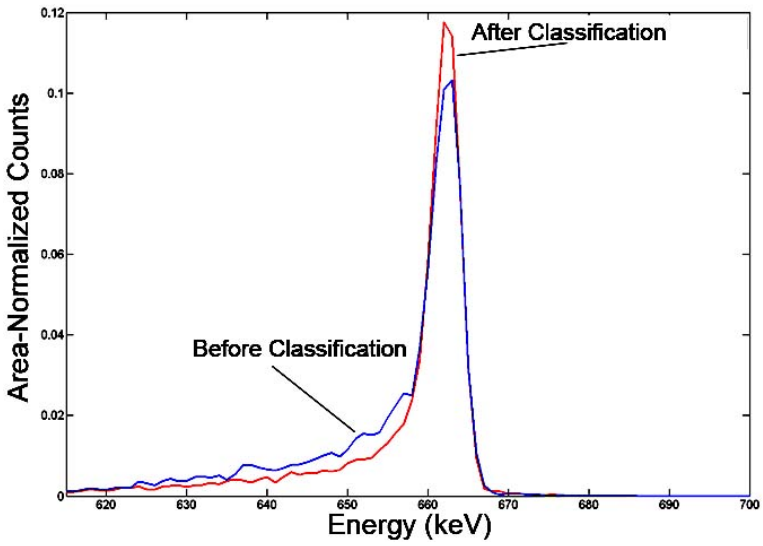

Figure 6.9: A CZT photopeak (662 keV) with and without event classification using pixel signal tail analysis. The favorable loss of low-energy tail counts is due to correct classification of charge sharing.

Once this correction is made, it is possible to study the effect of the energy threshold on the resolution and photopeak area. An appropriate threshold for the pulse tail is one that is set above the noise level. However, as described in section 5.2, the non-collecting pixel tail amplitude is increasingly negative as events occur nearer to the anode. The ideal threshold is set at the expected negative level plus the expected noise level. Then, a small amount of charge collection can be detected even if the measured pulse height is negative. To isolate the depth-effect, Fig. 6.10 shows the result of various threshold levels for events occurring in single depth near the cathode and a single depth near the anode. Near the cathode, the pulse tail is expected to be zero. The threshold settings below 10 keV yield significant resolution improvements, however the number single-pixel events is decreased. In this case, a lower threshold eliminates charge sharing events, so the remaining events are in fact due to interactions in the center of the pixel. This finding is verified using sub-pixel information in section 6.1.4. Near the anode, a lower threshold can be used to separate charge sharing events.

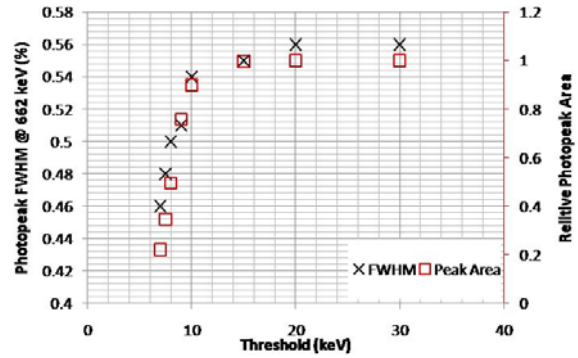

(a) Single Depth Near Cathode

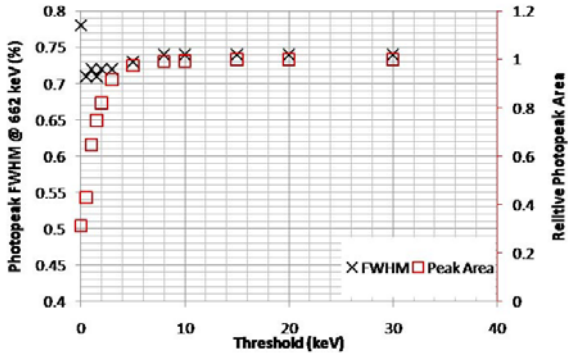

(b) Single Depth Near Anode

Figure 6.10: Resolution (%FWHM at 662 keV) and relative single-pixel photopeak area are plotted as a function of the charge-collection threshold.

Figures 6.11 and 6.12 show single and two-pixel (center and neighbor) spectra for a HgI_2 detector before and after tail analysis. The two pixel spectra are for neighboring pixels. Before event classification, a small peak is observed above the photopeak. This artifact is due to inaccurate identification of charge deposited on a neighbor pixel. Instead of measuring the tail amplitude, the shaping filter used in this example integrated the amplitude of the transient peak. Event classification makes it possible to predict whether or not charge collected on a neighbor even in the presence of a large transient pulse.

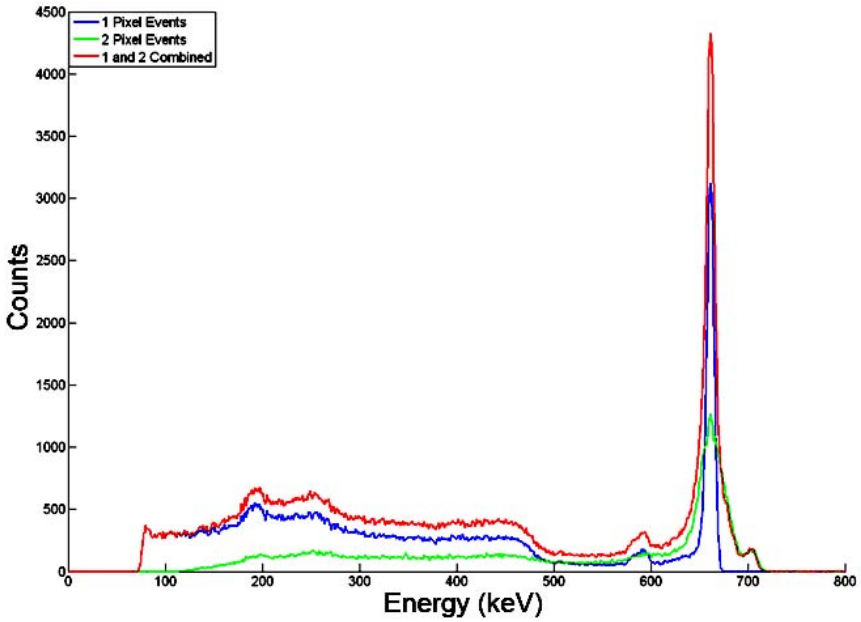

Figure 6.11: This example from HgI_2 shows the effect of improperly classified two-pixel events. A high energy tail and peak occurs as transient peaks are improperly identified as charge collection in a neighbor pixel.

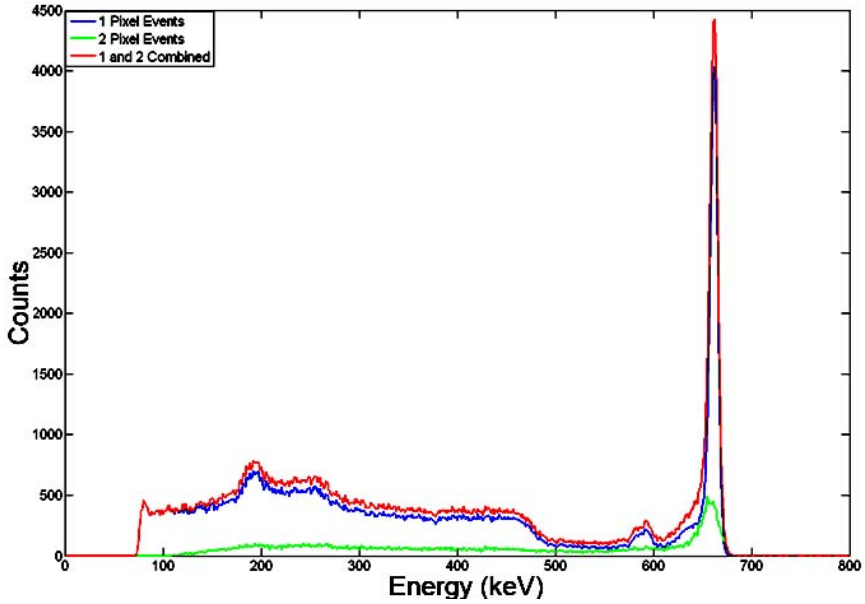

Figure 6.12: Using the same data as Fig. 6.11, proper two-pixel event classification removes this high energy tail resulting in a sharper photopeak.

6.1.2 Photoelectric Absorption

Classification of a photoelectric absorption event requires detection of a characteristic X-ray. Characteristic X-ray detection in CZT is relatively difficult because the energy of Cd and Te K_α and K_β X-rays are relatively low, between 23 and 32 keV. In Fig. 6.13 the south neighbor waveform contains a "step" near t = 2.1 μs with an amplitude proportional to a K X-ray energy. Identification of an X-ray provides classification of a photoelectric absorption, which, given a scatter elsewhere in the detector indicates the final interaction in a full energy Compton scatter sequence. Since this specific example also includes a Compton scatter between neighbor pixels, it is difficult to say whether center pixel or the south pixel is the absorption event. Given the limited range of the low-energy X-ray, it would be more likely that the center pixel is the photoelectric absorption and that the X-ray escaped from the center pixel and interacted in the neighbor pixel (at a depth similar to the center pixel).

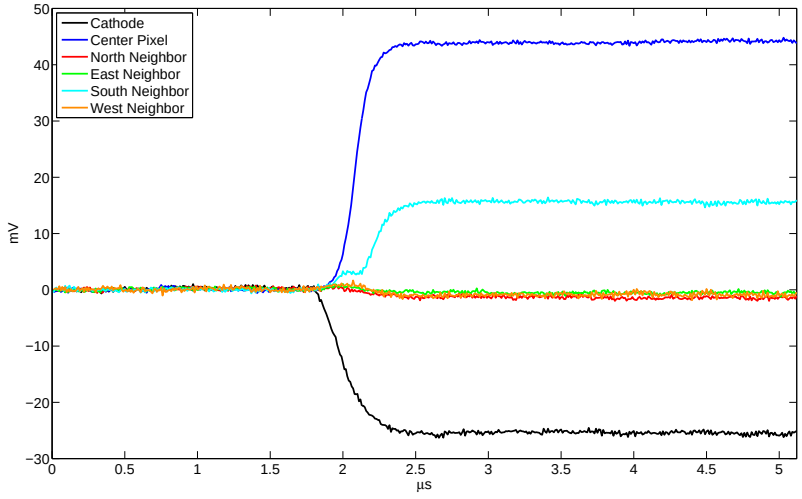

Figure 6.13: A likely characteristic-ray escape in CZT.

Waveforms from a photoelectric absorption event in HgI_2 are shown in fig. 6.14.

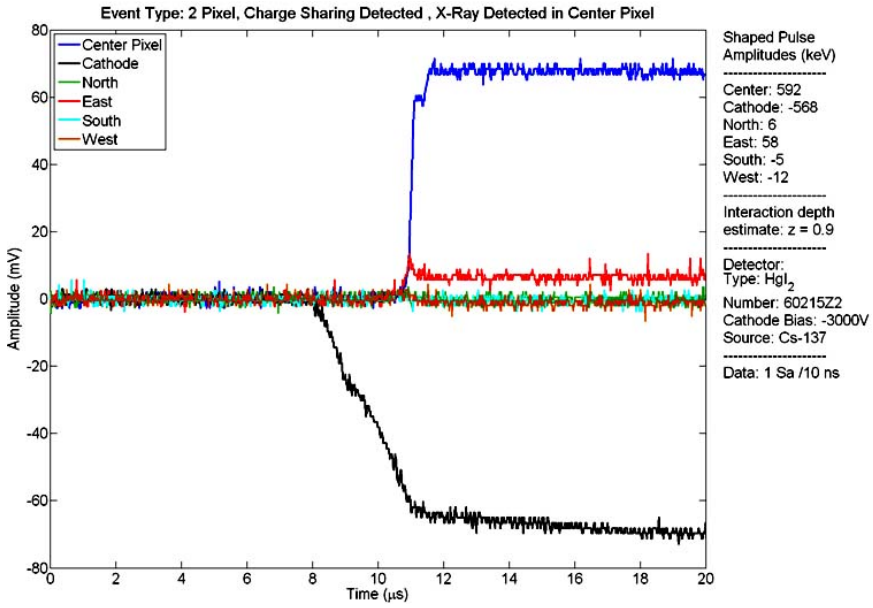

Figure 6.14: A signature photoelectric absorption in HgI_2 with charge sharing detected. The energy collected and the time difference in the center pixel allow for X-ray classification. The shape of the east signal indicates charge sharing.

A characteristic X-ray has been detected in the center collecting pixel. Evidence of charge sharing is also detected. Figure 6.15 shows two single depth (near cathode), single pixel energy spectra for a HgI_2 detector using a Cs-137 and Co-57 source. These spectra are useful because they demonstrate the different mercury and iodine X-ray escape peaks. In the Cs-137 spectrum the X-rays most likely escaped into another pixel. Using event classification, these X-rays can be detected and properly reconstructed. The Co-57 shows the spectrum of these X-rays that have escaped from one pixel into this collecting pixel that is demonstrated.

Figure 6.16 compares two photoelectric absorption spectra for a HgI_2 detector. The spectra include only multiple pixel events in which a characteristic X-ray has been detected. The blue spectrum is generated by events reconstructed simply by summing the energies together (after depth and weighting potential corrections were applied). The red spectrum represents an effort to add back exactly the average expected X-ray energy known for a given detected X-ray energy. In this example,

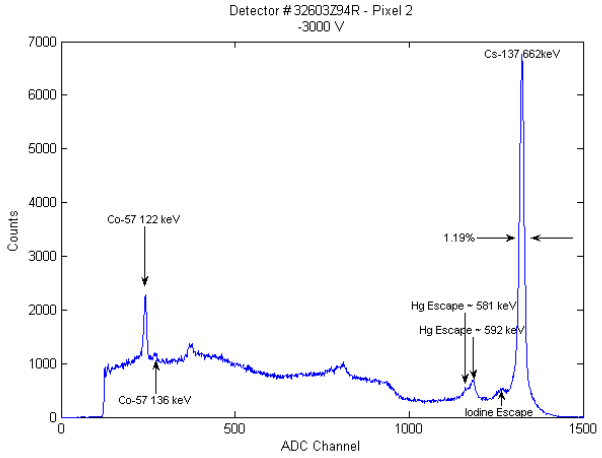

(a) Cs-137

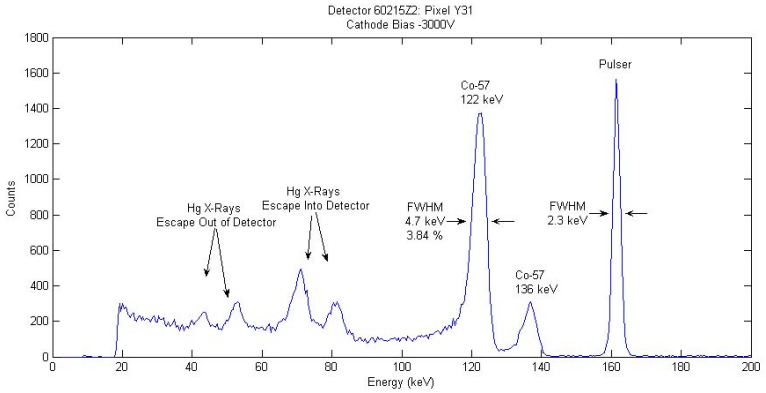

(b) Co-57

Figure 6.15: Single pixel spectra from a single depth near the cathode in a HgI_2 detector to demonstrate characteristic X-ray escape into and out-of neighbor pixels.

only 70 and 80 keV mercury K-shell X-rays were used. The method of adding exactly the expected energy back improved the resolution from 1.44% FWHM at 662 keV to 1.19%.

Although interaction type is known, the resolution of this method is not as good as the resolution of using purely single pixel events in which interaction type is not known. The main reason is that the X-ray spectra (as seen in Fig. 6.15) have their own uncertainty which, besides traditional sources including noise and charge statistics, is broadened by the difference in X-ray energies. For example, mercury K_α X-rays range between 68.9 and 70.8 keV. K_β X-rays range between 79.9 and 82.5 keV.

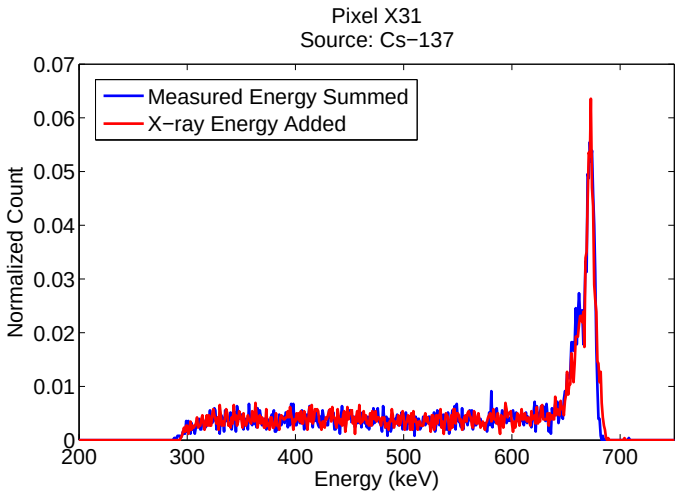

Figure 6.16: Photoelectric absorption spectrum in HgI_2 using two reconstruction methods.

Figure 6.15 (b) shows that these two X-rays can be separated, but in many cases, including 6.15 (a) whether the K_β or K_α X-ray is detected is practically impossible to discern.

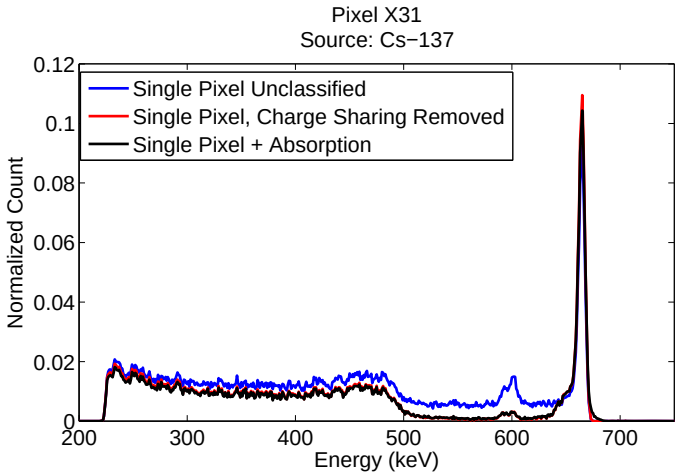

Figure 6.17: A comparison of Cs-137 spectra using three event classification techniques.

Figure 6.17 compares HgI_2 spectra generated from the same set of data: single pixel events without charge sharing classification (blue), classified single pixel events (red), and single pixel events plus classified photoelectric absorption events. These three cases are compared with other measurements in table 6.1. This table summarize the results of photoelectric absorption classification a HgI_2 detectors. There are

three main qualifying quantities in these tables: resolution, photopeak area, and photofraction. These factors provide a useful way to analyze the performance and practicality of the selected event classification methods.

Table 6.1: Summary of Photoelectric Classifications in HgI_2, Detector 60215Z2, Cs-137 Source

Method	% FWHM (662 keV)	Relitive Photopeak Area	Photo-fraction	Relative Photofraction
1. single pixel, no charge share class.	1.57	1.00	0.16	1.00
2. single pixel, w. charge share class.	1.46	0.90	0.21	1.31
3. absorption, normal reconstruction	1.57	0.10	0.31	1.94
4. absorption, X-ray reconstruction	1.18	0.10	0.31	1.94
5. single pixel plus absorption	1.47	0.99	0.23	1.44

Table 6.1 compares the results for the detector analyzed in Fig. 6.17. The first method listed is "1. single pixel, no charge sharing". This method uses the most simple classification algorithm. Here, events are classified as single pixel if the triggering channel is the only channel that collects charge above a threshold which is 25 keV for both experiments. This first method serves as a performance baseline. The resolution (FWHM @ 662 keV) for this method is 1.57 %. The photofraction of events using this method is 0.16. Since the method is the baseline method for this detector, the relative photopeak area and relative photofraction is 1.0.

The second method listed in table 6.1 includes the charge sharing event classification algorithm. This method is similar to method 1, however it uses a more sophisticated technique to sense charge sharing in neighbor pixels. As described in section 5.3, the pulse waveform tail height as a function of depth is measured for use in various calibration procedures. This data provides an expected tail height for each interaction depth. In method 2, when a single pixel event is detected using the basic threshold in method 1, the tail pulse height is compared to the expected tail height as measured during the calibration process. If the tail of the current event is higher than the expected value plus a user-defined number of standard deviations,

then the event is classified as a charge sharing event. Using method 2, events that occur near the anode surface having a negative amplitude can still be classified as a charge sharing event. The FWHM for method 2 is 1.46 % at 662 keV. The relative photopeak area for method 2 compared to method 1 is 0.90. Since the exact same measurement (the event list resulting from the digital signal processing stage) is used in both methods, the photopeak area can be compared directly. The photopeak area for method 2 is smaller than method 1 because correct classification of charge sharing events removes these events from the photopeak and are reconstructed in a separate algorithm. The photofraction for method 2 is higher than method 1 because a higher number of non-photopeak events were classified as charge sharing events than photopeak events.

Methods 3 and 4 are event classification results from two photoelectric absorption classification methods. The methods are described in the discussion of Fig. 6.16. Method 3 is the reconstruction technique where the measured energies of the multiple pixel event are added using the normal calibration adjustments. Method 4 is a method where exactly the expected X-ray energy is added to the main energy deposition measurement. The difference in energy resolution for these two methods is significant. When the exact X-ray energy is added, the FWHM is 1.18 % compared to 1.57 % at 662 keV. This difference is due to two primary factors. First, it eliminates uncertainty in the final number of charge carriers that are collected by the anode. This uncertainty includes the inherent fluctuation in charge carriers, and charge loss due to trapping. It also eliminates the need for calibration of the measured X-ray energy deposition. Calibrations that would otherwise have to be applied include the depth-dependant response calibration that accounts for trapping, weighting potential non-uniformity and material non-uniformities, as well as the weighting potential

cross-talk correction. Weighting potential cross-talk still needs to be applied for the non X-ray signal. It is also important to note that these corrections were used prior to the step to detect that the energy deposition fell within the X-ray energy range in the first place.

The relative photopeak area for both photoelectric absorption classification methods is significantly lower than the other two methods. This is a measurement of how often characteristics X-rays can be identified for this measurement. In this experiment, only 4 neighbor pixels are used to detect for characteristic X-rays. X-rays are also identified that occur under a single pixel if the interactions occur at depths that can be distinguished by a time difference in the signal processing software. The photofraction for methods 3 and 4 are the highest of all the methods presented in Table 6.17.

Method 5 combines the non-charge sharing, single pixel events from method 2 are combined with events that have been classified as photoelectric absorption events. This includes single or multiple pixel events. The FWHM of method 5 is 1.47 % at 662 keV. The relative photopeak area for this method is almost equal to that of the baseline value. This is because method 5 contains all of the single pixel events as reported in method 2 as well as additional photoelectric absorption multiple pixel events not included in method 1 or 2. The photofraction for method 5 is similar to that of method 2, but is slightly better due to the presence of the events classified in method

Table 6.2 includes the same analysis as Table 6.1 for another HgI_2 detector. The energy resolution of this detector is better than the detector in Table 6.1. The photofraction results are higher using the classification methods because 8 neighbor pixels were used instead of 4. Using twice as many neighbor pixels allows better

X-ray and charge sharing identifications. The four neighbor pixels that were added are the four corner pixels relative to a central pixel.

Table 6.2: Summary of Photoelectric Classifications in HgI_2, Detector 61420Z2, Cs-137 Source

Method	% FWHM (662 keV)	Relative Photopeak Area	Photo-fraction	Relative Photofraction
1. single pixel, no charge share class.	1.05	1.00	0.18	1.00
2. single pixel, w. charge share class.	1.04	0.84	0.24	1.33
3. absorption, normal reconstruction	1.44	0.25	0.50	2.78
4. absorption, X-ray reconstruction	1.19	0.25	0.49	2.72
5. single pixel plus absorption	1.06	1.03	0.35	1.94

6.1.3 Pair Production

Classification of pair production is similar to photoelectric absorption because it relies on detection of a characteristic energy. Detecting 511 keV is easier than detecting a 30 or 70 keV X-ray, however complications can arise when the 511 keV photon undergoes Compton scattering. To demonstrate classification of pair production, an experiment was conducted using a Th-228 source. The photon of interest from this source is the 2.614 keV photon from Tl-208.

As described in table 6.7, classification of pair production is relatively easy. If a 511 keV energy deposition is detected, either individual or summed, the likelihood for pair production is high and can be compared to the likelihood of a Compton scatter with a 511 keV deposition on an event by event basis. If two 511 keVs are measured, then pair production is almost certain. In this case, as in table 6.7, if the two 511 keV photons lie in the same axis as the pair production location, then pair production is a virtual certainty.

Unfortunately, the experimental data that was collected did not contain significant measurements of this last signature. The reason is that the detector volume that could be measured using the prototype system was limited to 15 pixels, roughly 10 % of the total volume. With this limitation, it is very unlikely that the two 511

keV annihilation photons would be detected in this small region. This, combined with the fact that the source was low activity, and the 2.614 MeV yield is low, made experimental demonstration impractical.

Luckily, this problem turned into a discovery. Figure 6.18 shows the single-pixel spectrum for the Th-228 source. When the sub-pixel response calibration was made, a discontinuity was observed at the 1592 keV double escape peak. The three boxes in the top of Fig. 6.18 show the sub-pixel interaction distribution for the 1592 keV double escape peak and the Compton scatter events immediately on either side of the peak. Only single pixel events are used. The source was positioned on cathode side of the detector. As the energy of photoelectric absorption or Compton scatter interactions increases, the charge cloud scales linearly as described in chapter II. As clouds from these interactions increase in size, the likelihood of charge sharing increases. For example, a 1592 keV photoelectric absorption interaction would have a charge cloud with a dimension 2.4 times that of a 662 keV photoelectric absorption interaction. However, the single-pixel sub-pixel distribution of the 1592 keV double escape peak is larger than that of the Compton scatter interactions within a mere 50 keV of the escape peak.

The sub-pixel distribution for Compton scatter interactions near 1592 keV is small because charge clouds from these interactions can only be a single-pixel event (no charge shared with a neighbor) if the centroid of the electron cloud is in the middle of the pixel. This distribution is seen in the sub-pixel distributions on either side of the double escape peak. Most of the events in the escape peak energy range are pair production interactions. Unlike a Compton scatter interaction at 1592 keV, the energy remaining after pair production is shared between the electron and positron. Instead of a charge cloud with a dimension proportional to a 1592 keV photoelectric

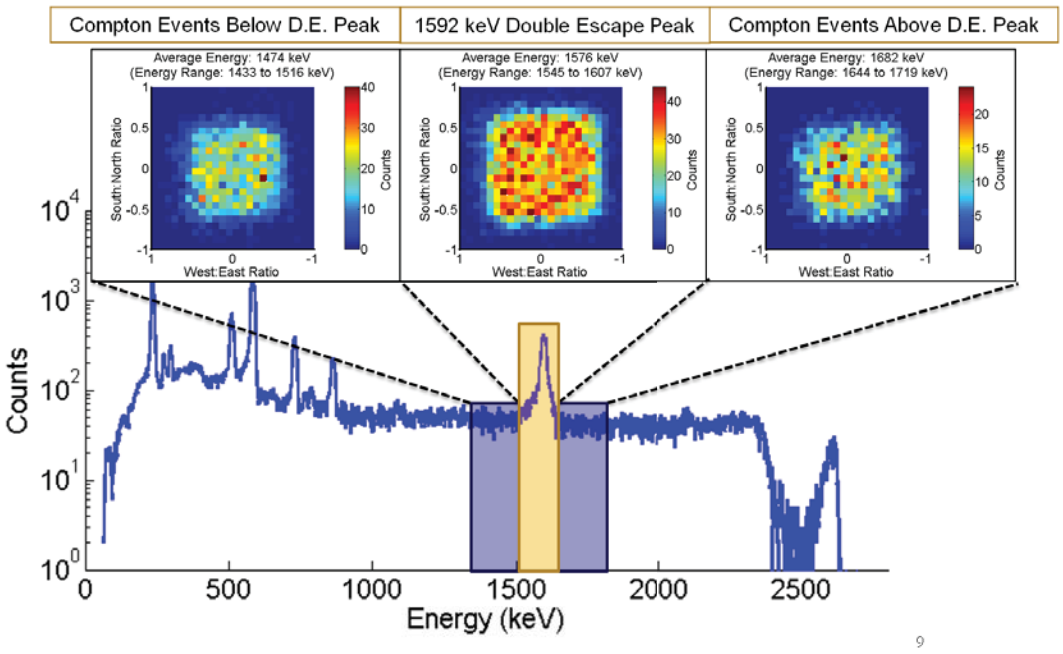

Figure 6.18: The sub-pixel, single-pixel-interaction distribution is shown for three energy regions: before the 1592 keV double escape peak, the double escape peak, and after the double escape peak. The distribution for the events in the double escape peak is larger than the distribution for the Compton scatter events on either side. Since the sub-pixel distribution for single pixel events depends on the size of the charge cloud, the charge cloud for pair prodction events in the double escape peak is smaller.

absorption or Compton scatter, the cloud from energy loss of the pair has a smaller dimension. The result observed in this experiment is that pair production interactions can occur in sub-pixel positions *other than* the center of the pixel without sharing charge with a neighbor. A similar-energy Compton scatter (depositing 1592 keV) cannot occur outside of the pixel center without sharing charge with a neighbor.

Figure 6.19 shows another way of looking at this phenomenon. This chart plots the FWHM of the vertical (y) and horizontal (x) sub-pixel, single-pixel-interaction distributions for ten different energy regions of the Th-228 spectrum. The values of the distribution have been normalized. In this case, a sub-pixel event distribution that would span across an entire pixel pitch would have a value of "$d = 1$." On the other extreme, if a charge cloud is larger than the lateral area of a pixel, all events would be multiple pixel events and there would be no single pixel distribution, there-

fore "$d = 0$." As expected, the distribution decreases with energy. As the size of an electron cloud decreases, events occurring near the edge of a pixel are classified as multiple pixel events and will not show up in these single pixel distributions. As a result, the width of these distributions decreases in both the x and y dimensions. Values of distributions associated the simulated dimensions of electron clouds of various energies are also shown for comparison. A second set of simulated data includes an electron cloud diffusion model that includes. At higher energies, the experimental data (for x and y) diverges from the simulation data. The distributions from the experimental data are larger than those predicted by experiment. The experimental distributions are larger because of how the experiment was set up. Because the pixels were irradiated from the cathode side of the detector, the incident angle of the photons was normal to the lateral area of the pixel. At higher energies the photoelectron is emitted in a forward direction which causes the charge cloud to become elongated as is shown in the simulated results. However, since the photoelectron is emitted parallel to the volume of a pixel, this electron cloud is formed parallel to the pixel volume. The vertical dimension may be as the simulation predicts, however the lateral cross section is smaller. If the Th228 source were placed on the side of the detector, and the electron clouds formed perpendicular to the volume of a pixel, the distribution would follow closer to the simulated results at higher energies. As illustrated in Fig. 6.18, the distribution of the double escape peak is wider than the Compton scatter events at energies just above and below the double escape peak. For reference, the dashed lines that bracket the distribution of the double escape peak show the simulated distribution from an 800 keV electron cloud (above) and the estimated size of two 800 keV electron clouds that would have formed in opposite directions (below).

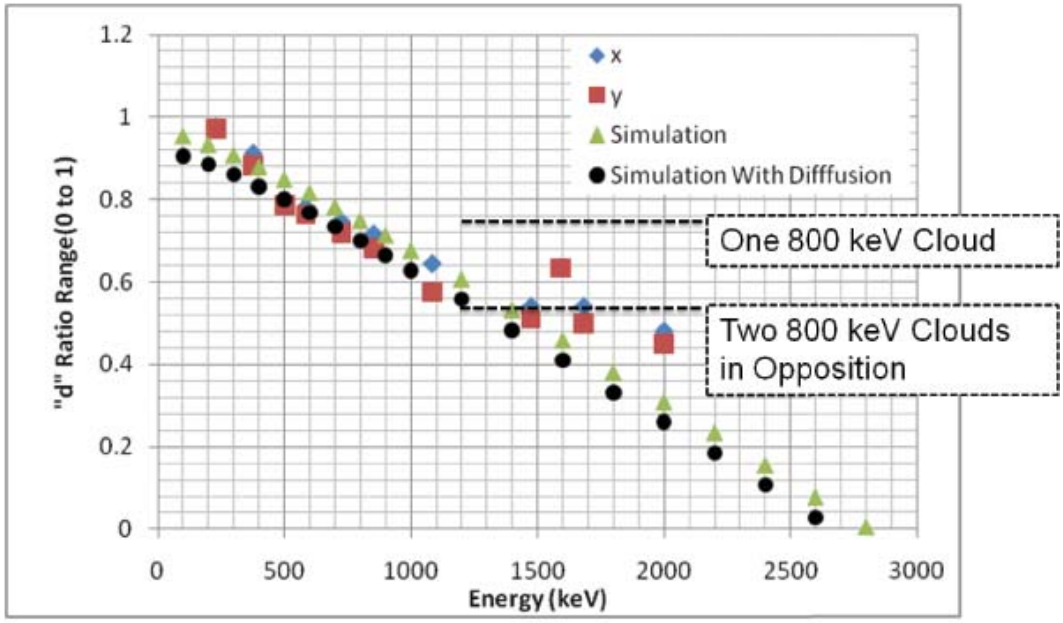

Figure 6.19: The FWHM of the vertical (y) and horizontal (x) sub-pixel, single-pixel-interaction distribution (or "Ratio") is shown for ten different energy regions of the Th-228 energy spectrum. Simulated values of the distributions of electron clouds of various energies are also shown for comparison. The simulated data includes a model that includes diffusion of the electron cloud. The distribution of the double escape peak is wider than the Compton scatter events at energies just above and below the double escape peak. For reference, the dashed lines that bracket the distribution of the double escape peak show the simulated distribution from an 800 keV electron cloud (above) and the estimated size of two 800 keV electron clouds that would have formed in opposite directions (below).

This observation leads to an entirely new way to classify a pair production event, one that does not require detection of a single 511 keV. If the charge cloud of a double escape energy event is measured to be smaller than the expected cloud for that energy, then pair production is likely. This can be measured in the pixelated detectors studied in this thesis using classifications of charge sharing and sub-pixel position estimates. A classification of a pair production event without a 511 keV photon detection would require the following criterion: the event occurs in sub-pixel position outside the expected region for an escape peak energy charge cloud. This criterion requires knowledge of the expected charge cloud size for a given energy, but this distribution expectation is a part of the sub-pixel calibration process. At high

energies, the lateral distribution of a charge cloud changes depending on the incident angle of the incoming photon. This study only characterized interactions from one source incident angle. Future studies will analyze the charge cloud distribution as a function of incident angle.

6.1.4 Compton Scatter

The task of classifying scattering interactions is made easier because identification of pair production and X-ray escape occurs before scattering. If characteristic energies are detected, the event is never considered for Compton scatter classification. With the options narrowed in this way, classification of Compton scatter events is relatively easy except for the specific case of same-depth scatters into a neighbor pixel. At this point in the routine, if charge is collected in a non-neighbor, then it is classified as Compton scattering. In the case of a neighbor pixel, if charge is deposited in different depths, a difference in collection time is observed and serves as a Compton scatter signature. Figure 6.20 shows an example of depth-separate Compton scattering in a neighbor pixel for CZT and HgI_2.

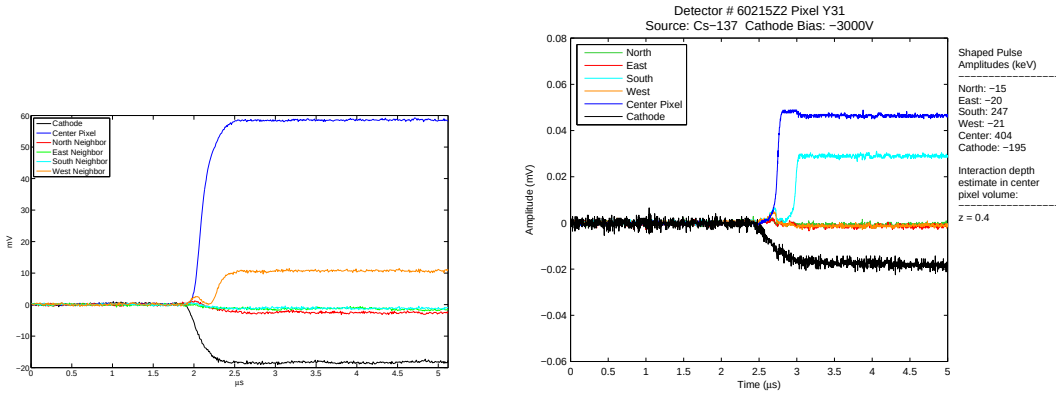

(a) CZT (b) HgI_2

Figure 6.20: Experimental examples pulse waveforms of multiple pixel Compton scattering in CZT and HgI_2.

Figure 6.21 shows examples of a single pixel scatter event in CZT and HgI_2. This

signature relies on recognition of two electron clouds in the same pixel which can be observed as pile-up in a single pixel pulse. The time length of the "step" seen in the center pixel is equal to the difference in drift time between the two electron clouds.

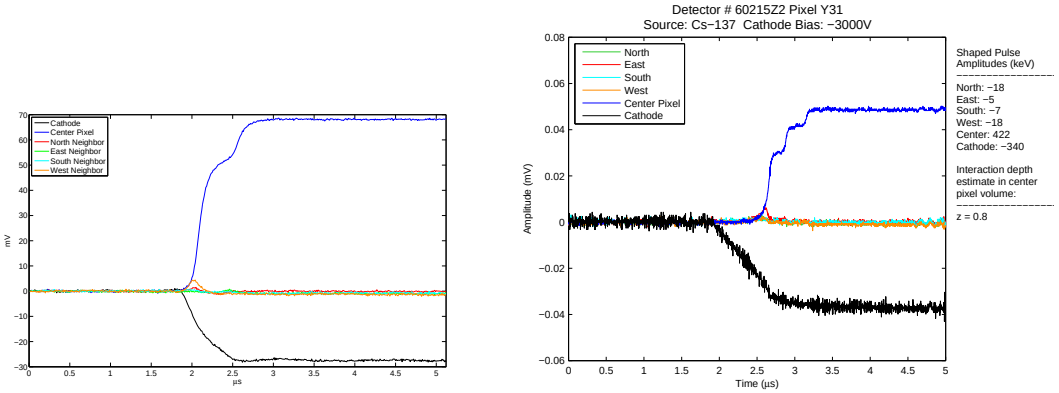

(a) CZT (b) HgI_2

Figure 6.21: Compton scatter events that occur under the same pixel anode.

If the charge is collected in coincidence, it is possible that the second energy deposition happened at the same depth (same charge drift time). Another possibility is that the charge cloud is shared between two or possibly more pixels. The next sections explore methods to distinguish charge sharing.

6.1.5 Charge Sharing Detection

Figure 6.22 shows two CZT waveform sets where charge sharing is present. A small transient peak can be seen in the neighbor pixels that collect charge. The sub-pixel position of the interaction provides the classification algorithm with additional evidence of charge sharing. The sub-pixel classification of charge sharing is demonstrated in detail in section 6.2.

When a single interaction takes place near the anode, the non-collecting neighbor pulse is expected to be negative due to the difference in weighting potential. When a neighbor shares charge in this situation, the expected negative tail must be taken

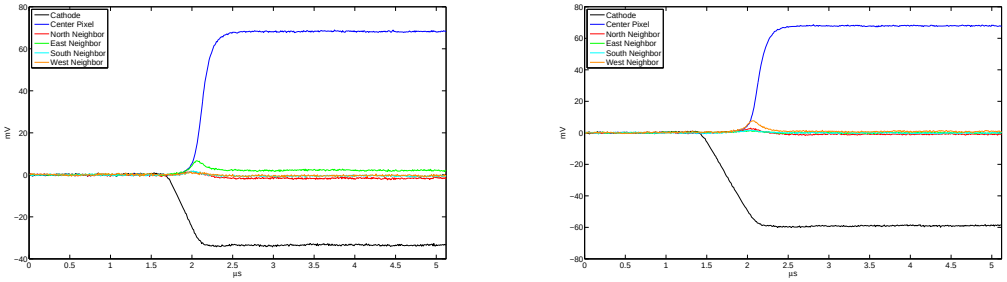

(a) Charge Sharing (b) Charge Sharing

Figure 6.22: Easy Charge Sharing Sum = 662 keV

into consideration. Figure 6.23 shows an example waveform set in CZT. The amount of charge collected by the west neighbor would then be equivalent to the west amplitude plus the magnitude of the negative response on the west pixel when no charge is shared. This reconstruction requires a detailed calibration of the negative tail response as a function of depth. With such a calibration it is also possible to detect charge sharing even when there is no positive amplitude in the tail.

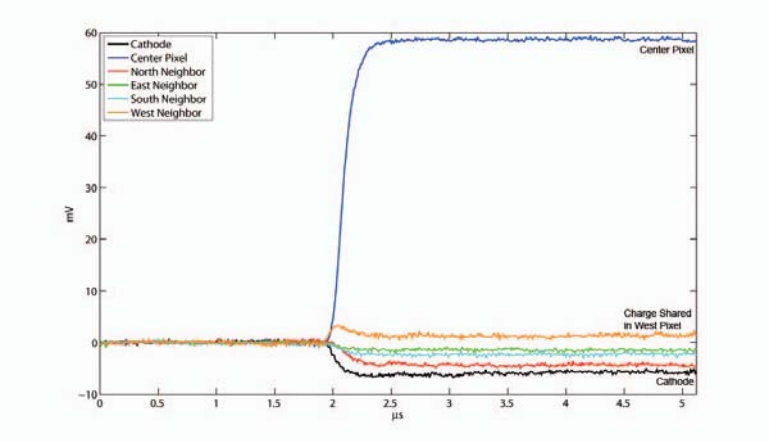

Figure 6.23: Charge sharing near the anode.

6.2 Classification Method Verification

The event classification algorithms developed for this study are based on experimental observations and theoretical understandings of the detector response to various interaction mechanisms. In order to verify the accuracy of the classification

algorithms, a series of experiments were conducted that used known events to test the software. There are three categories of tests that were carried out. The following subsections present the details of the experiments and explain the methods and results of these validation tests.

6.2.1 Simulation Verification Study

Chapter II discussed the waveform simulation tools that have been developed for this thesis study. The waveform simulator can accept events generated by the user, or events generated by Monte Carlo based radiation transport simulations. In this section, event lists generated in GEANT 4 were passed into the detector response simulation software described in chapter II. A benefit of the simulation method is that the event type can be known and compared to the algorithm response. Simulation testing is powerful because the type of event that is used to test the classification algorithm can be known with absolute certainty.

Sets of event data were collected from two separate simulations, one at 662 keV, and one at 2.6 MeV. Subsets of data from these simulations were used to test the event classification algorithm. The subset of events that were selected from each simulation was based on criteria including event type, energy, and interaction position. For example, the subset used to test the photoelectric absorption algorithm group does not include photoelectric absorptions that emit X-rays below 25 keV nor X-rays that interact too close to the original interaction site because these are well-understood limitations of the algorithm. As described earlier in this chapter, the current classification algorithm is limited by the precision of the data coming from the detector. Ideally, 100 % of the selected *simulated* events would be identified correctly, but this does not happen because selection of test data is made before reality-based detector-response complications such as noise, weighting potential and

trapping effects, and electron cloud are included in the simulation.

At 662 keV, the algorithm correctly classified 12.7 % of all simulated photoelectric absorption events where the characteristic X-ray was absorbed in a single pixel. This number is low because the of the algorithm's limitations and settings. For example, only 26 % of the simulated full energy deposition photoelectric absorption events had X-rays over 25 keV which is the threshold used in the software. When events were selected to include only events that yield X-rays above 25 keV interacting in depths 1 mm away from the original interaction depth, 89.4 % of events were classified as photoelectric absorption. The events that were classified incorrectly were classified as single pixel events with no X-ray. When the characteristic X-ray was detected in a neighbor pixel, the result using the selected events was 90.2% photoelectric absorption classifications. For Compton scatter events, there was no energy limitation included in the selected events because the events are known to be Compton scatter, but events that occur with a difference in depth that is greater than 1 mm were not included in the test. Classification of Compton scattering in a single pixel and into a neighbor pixel was correct 90.2% and 94.6% of the time respectively. The remainder of the events were classified as charge sharing or photoelectric absorption. Finally, charge sharing events were correctly identified 71.2% of the time. The reason charge sharing identification is lower, is because often, the amount of charge shared is below the multiple-pixel event threshold. Simulated pair production events were correctly identified 98.8% when at least one 511 keV photon was completely absorbed.

6.2.2 Collimator Verification Experiment

The collimator verification experiment is designed to test the accuracy of the classification algorithms in the difficult circumstance of side-neighbor events. The

design of the collimator study is illustrated in Fig. 6.24. The collimator was used to generate two sets of test events. The first position generated events in the center of a pixel. The second collimator position generated events in the inter-pixel gap. Figure 6.25 shows the actual experimental setup. The collimator is made of 6 cm thick tungsten with a 100μm opening. The collimator is located 3 cm away from the surface of the detector. A Cs-137 point source is placed in the collimator and used to irradiate on the cathode side of the detector. At the cathode surface, the collimator beam expands to a width of approximately 200 μm. At the pixel surface, the beam width is approximately 250 μm.

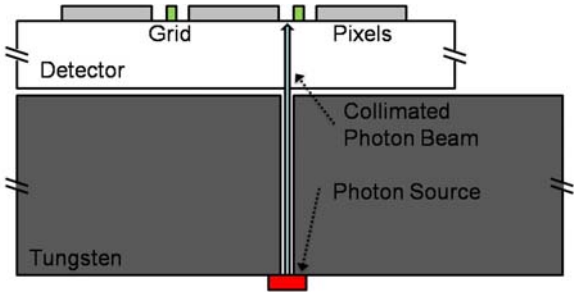

Figure 6.24: The collimator experiment design for collecting data at desired lateral sub-pixel positions. The collimator is used to study the difference between interactions occurring in the center of a pixel and those occurring in the inter-pixel gap.

When the collimator is positioned near the center of the pixel, there should be little charge sharing between the neighbor pixels at an energy of 662 keV. Since the collimator is a fan-beam, two of the neighbor pixels would experience charge sharing, but they were not included in this study. Since the collimator eliminates the possibility of charge sharing, multiple pixel events at this energy involving the irradiated pixel and its neighbors can only be due to characteristic X-ray escape or Compton-scattering. Because the goal is to test the classification algorithm with a set of known events, the next step of the validation effort requires the separation of photoelectric absorption from Compton scatter events.

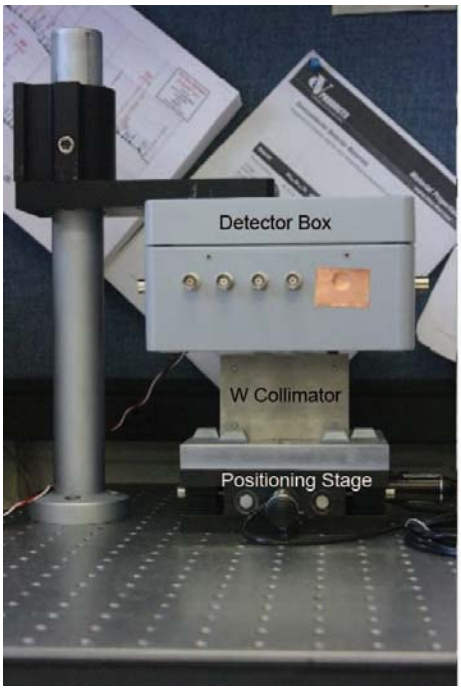

Figure 6.25: A side view of the actual collimator used in the experiment. The collimator is positioned underneath the detector box. The beam is focused on the cathode side of the detector.

Since the source energy and incident angle is known, these two event types can be separated using an energy threshold. First, we only consider events involving both the irradiated and neighbor pixels whose combined charge collection would place the event in the 662 keV photopeak. Among this set of data, photoelectric absorption events can be identified by choosing all instances where a characteristic X-ray energy is measured in the neighbor pixel and the remainder of the 662 keV is measured in the irradiated pixel. This set of data will not include all photoelectric absorption interactions, but all the interactions in the set of data will be photoelectric absorptions. The events cannot be charge sharing because of the collimator position. The events cannot be due to Compton scatter because it is not kinetically possible for there to be 25-33 keV deposited in a neighbor pixel at this energy and source position. Compton scatter interactions can be separated using the same concept. Again, charge sharing is impossible because of the collimator. All 25-32 keV events

in the neighbor are photoelectric absorption. Therefore all other full energy events that have an energy deposition in the neighbor pixel must be Compton scatter events.

When the experimental photoelectric absorption event data was processed by the classification routine, 12.4 % of the events were classified as photoelectric absorption. Ideally 100% of these events would be classified correctly since all of the events in this test were determined experimental to be photoelectric absorption. However, the result is relatively low because the algorithm cannot distinguish between photoelectric absorption and charge sharing when the measured depth difference between charge collected in two pixels is less than 1 mm. Because the characteristic X-ray energy is low (and therefore has a small range in CZT), there is a high likelihood that the X-ray will be absorbed in a neighbor pixel at a depth less than 1 mm from the interaction site in the irradiated pixel. This means that the remaining 87.6 % of events that we knew to be photoelectric absorption events were incorrectly classified as charge sharing because these events met the criteria for charge sharing events. Besides serving as a source of test data, this experiment demonstrates that if the algorithm was configured to consider known incident angles, better event classification decision could be made. However, the algorithm configuration tested in this study assumes no knowledge of the source energy or position.

The other data set from the pixel-centered collimator experiment include Compton scatter into a neighbor events. When the experimental Compton scatter events were passed through the classification algorithm, 79.3 % were correctly identified. Since these events were pre-selected with a known full energy deposition, potential X-ray escape events were effectively removed. Since the energies of the scattered photon is much higher than characteristic X-ray energies, the depth difference between the charge collected in the two pixels was not a significant issue. However, some of these

events were classified as charge sharing because of this constraint even though the collimator minimized the presence of charge sharing events.

The collimator was moved to the gap between the pixels to study charge sharing. To test the algorithm's ability to classify charge sharing, we need a set of data that only includes charge sharing events. Again we only consider events where all 662 keV was deposited in the detector. First we eliminate events where the full 662 keV was deposited in the gap (measured in the two pixels). This eliminates photoelectric absorption events and the contamination that could come from characteristic X-rays looking like charge sharing. Next, instead of eliminating Compton scatter events we use them to our advantage. We only select events where the sum of the energy in between the two "sharing" pixels and another energy deposition elsewhere in the detector is the full 662 keV in another pixel. In this way we have a high degree of certainty that the shared energy is from a single, non-photoelectric interaction. When these events were processed by the event classification software, 93.3 % were classified as charge sharing events.

6.2.3 Sub-Pixel Resolution Based Classification Verification Study

The purpose of the sub-pixel verification study is nearly identical to that of the collimator study. Instead of a mechanical collimator, sub-pixel information is used to isolate charge sharing, photoelectric absorption, and Compton scatter events. The same event separation criteria used for the collimator test was used in this test. There is a slight difference in that sub-pixel information alone does not tell you where the source is. Sub-pixel information does give a more precise estimate of the interaction location and we do still know the source position in the experiment. However, because there is no collimator, there is more uncertainty in the incident angle.

Before the classification algorithm is tested, the sub-pixel position requirement associated with certain classification decisions is turned off. In this case, charge sharing is the default interaction type for charge collection in a neighbor pixel that does not meet the other criteria including characteristic X-ray energies and non-coincident charge collection. Without the sub-pixel position requirement, a significant fraction of the charge sharing events were classified as photoelectric absorption events if the energy fell within the X-ray window.

Another goal of the sub-pixel verification study is to study charge sharing in greater detail. The effect of charge sharing on energy resolution of both single and multiple pixel events is an issue that can be corrected. As described in chapter V, the lateral interaction position within a single pixel can be calculated using analysis of the charge induction signals from pixels that neighbor the pixel where the interaction takes place.

Sub-pixel position estimates can be used to compare spectra from different interaction locations within a single pixel. Figure 6.26 shows two depth-corrected Cs-137 spectra from the same pixel. The first spectrum includes events from all interactions locations within the pixel volume. The second spectrum only includes interactions occurring in the center sub- pixel region of the pixel. The photopeak areas of the two spectra have been normalized for comparison. The Compton continuum of the center pixel spectrum has fewer counts than the full-pixel spectrum because the current sub-pixel method is noise-limited to events with large transient pulses. Depending on the interaction position, some transient signals can be distinguished from noise at relatively low energies. Both of the spectra in Fig. 6.26 show a reduction in events below 200 keV and very few below 100 keV which indicates that the method performs poorly below this energy. The event trigger threshold of the experiment was 30 keV.

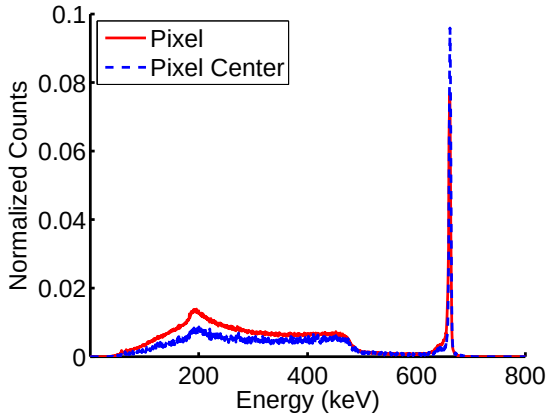

Figure 6.26: Comparison of spectra from events that interact in the middle of a pixel (dashed line), with those that interact throughout the entire pixel (solid line).

The most interesting difference between these spectra occurs in the photopeak region. The first difference can be found in the low-energy photopeak tails. In the pixel -center spectrum, there are fewer events in the low-energy tail region compared to the full-pixel spectrum. This observation is consistent with the understanding that one factor that results in low-energy photopeak tail counts in a pixelated detector is the deficiency of collected charge due to charge sharing and loss in the gap between pixels. Events from interactions occurring in the center of a pixel are the least likely to share or lose charge (assuming the size of the electron cloud is smaller than the pixel size). The full-pixel spectrum has more counts in the low energy tail because it includes events near the pixel edge where charge can be shared to other pixels or lost to the gap. Photopeak energy resolution solution is another difference between these two spectra. The FWHM at 662 keV of the full pixel spectrum is 0.65%, which improves to 0.58% in the center-pixel spectrum. In this way, calibration methods based on the sub-pixel interaction positions can improve overall energy resolution by accounting for charge sharing and loss for events near a pixel edge.

Sub-pixel interaction position estimates can also be used to study the effect of charge sharing on multiple-pixel events. Figure 6.28 shows depth-corrected spectra

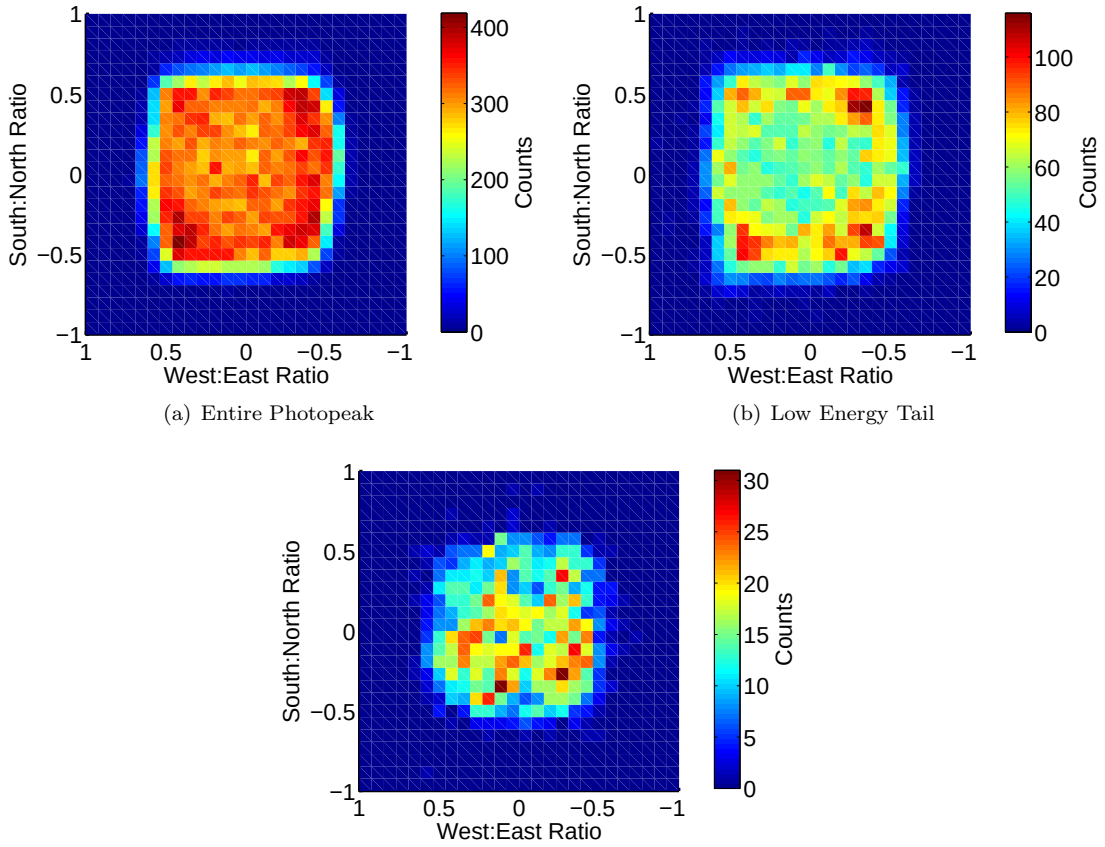

(a) Entire Photopeak

(b) Low Energy Tail

(c) High Energy Side of Photopeak

Figure 6.27: Comparison of sub-pixel interaction position for three different energy windows. The color bar indicates the number of counts per 2-D bin.

from two-pixel events of non-neighbor pixels. A Compton scatter between two pixels is an example of the type of event that makes up this spectrum. Two spectra are shown in Fig. 6.28. The first includes scatters between any interaction location in the first pixel to any interaction location in the second pixel. The second spectrum includes scatters from interactions in center region of the first pixel to an interaction in the center of the second pixel. When the two interactions occur in the center region of each pixel, the photopeak resolution (FWHM at 662 keV) is 0.79 % compared to 0.99 % for full-pixel interaction events. As in the case of single pixel events in Fig. 6.26, the low energy tail of the pixel-center spectrum is smaller than the full-pixel spectrum.

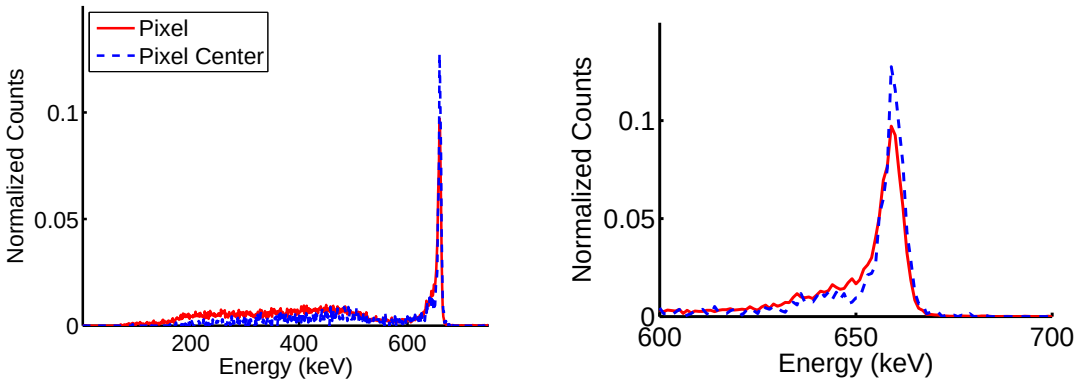

(a) Entire Spectrum (b) Photopeak Region

Figure 6.28: Two-pixel CS-137 spectrum for events between two non-neighboring pixels. The spectrum of events interacting in the center of the pixel (dashed line) is compared to the spectrum due to events interacting in the entire pixel volume.

6.3 Event Classification Result Summary

A summary of the event classification results for a variety of experiments is given in Table 6.3. Table 6.3 displays the percentage of events that fall into the four primary classifications for a given measurement. For example, in the first HgI_2 experiment, 3.2 % of all events measured were classified as single pixel photoelectric absorption events. There were two major experiments conducted with HgI_2 detectors. Both used a Cs-137 source. There are five separate CZT experiments listed in this table. Experiments 1, 2, and 3 used a Cs-137 source. Experiments 4 and 5 use a Th-228 source. One of the difficult parameters to set in the CZT classification procedure is the time threshold used to separate events at different depths. To demonstrate the effect of this parameter, three different thresholds are presented in table 6.3. Experiments denoted by "a" use a 200 ns threshold, "b" experiments use a 100 ns threshold, and "c" experiments use a 50 ns threshold.

In HgI_2, it is relatively easy to identify characteristic X-rays because they are over twice the energy of X-rays in CZT. In HgI_2, characteristic X-rays could also be

Table 6.3: Event Classification Result Summary (% of Recorded Events)

Detector	Photoelectric Absorption		Pair Production	Compton Scatter		Charge Sharing
	Single Pixel	Neighbor		Single Pixel	Neighbor	
HgI_2: 1C-19	3.2	28.5	-	4.0	53.2	14.8
HgI_2: 1C-20	4.2	30.7	-	6.7	50.7	13.4
CZT: 4E-07 (1a)	-	3.9	-	1.3	10.0	69.8
CZT: 4E-07 (2a)	-	3.9	-	1.2	10.0	69.9
CZT: 4E-07 (3a)	-	3.7	-	1.4	12.6	67.9
CZT: 4E-07 (1b)	-	3.4	-	1.9	15.4	65.9
CZT: 4E-07 (2b)	-	3.4	-	2.2	15.5	65.9
CZT: 4E-07 (3b)	-	3.3	-	2.0	17.8	64.1
CZT: 4E-07 (1c)	-	1.4	-	2.7	35.1	51.5
CZT: 4E-07 (2c)	-	1.3	-	2.8	35.3	51.4
CZT: 4E-07 (3c)	-	1.3	-	2.7	36.9	50.1
CZT: 4E-07 (1d)	-	0.7	-	3.9	51.2	39.0
CZT: 4E-07 (2d)	-	0.7	-	3.8	51.2	39.0
CZT: 4E-07 (3d)	-	0.7	-	3.9	52.6	37.9
CZT: 4E-07 (4)	-	-	21.0	-	-	-
CZT: 4E-07 (5)	-	-	21.9	-	-	-

identified in single pixel events, and 3.2 % and 4.2 % of all single pixel events could be classified as photoelectric absorption events. In the two HgI_2 experiments, 28.5 and 30.7 % of two-pixel neighbor events were photoelectric absorption interactions. This percentage is much higher than the photoelectric absorption results for CZT. Because the energy is low, and the charge transport speed is higher than in HgI_2, detection of characteristic X-rays in a single pixel was impractical. However, it was possible to detect some characteristic X-rays in neighbor pixels. Over the various CZT experiments, between 0.7 and 3.9 % of two-pixel neighbor events were classified as photoelectric absorption.

As described in section 6.1.3, pair production classification is quite easy for multiple pixel events, however significant event statistics were not available for pair production events. The pair production classification values in table 6.3 are for single pixel events. These classifications were made using the sub-pixel distribution method. Roughly 21 % of single pixel events in the double 1592 keV escape peak of

a Th-228 source were classified as pair production events.

For both CZT and HgI_2, Compton scatter events in a single pixel could be classified if the energies and depth differences fell within the applied thresholds. In HgI_2, just over 50 % of two-pixel neighbor events were classified as Compton scatter interactions. As is evident in the CZT experiments, the time threshold plays an important role in the distinction between charge sharing and Compton scatter events.

CHAPTER VII

Conclusions and Future Work

7.1 Future Work

This section explores the ongoing research goals and introduces future research avenues. As discussed in chapter I, the ultimate goal of an event classification procedure is to identify interaction types event by event. If more than one possible interaction type is possible, a calculated likelihood is desired if the event is to be reconstructed properly. As demonstrated in chapter VI there are only a few relatively rare cases where more than one event type is likely. The best example involves coincident charge collection in neighbor pixels. Sub-pixel information has provided useful information in distinguishing most charge sharing from same-depth Compton scatters and characteristic x-ray escape. The Compton sequence reconstruction algorithms already implemented in the imaging software used for these detectors can be used to further estimate likelihoods of unclassified neighbor events. This effort is already being investigated using the current analog ASIC readout methods and associated software.

7.1.1 UM Digital ASIC

The experimental data used for this thesis were all collected using the prototype waveform digitizer system described in chapter III. A new, fully functional digi-

tal ASIC capable of collecting digitized waveforms from all 121 detector pixels has recently been tested. Future experiments using full digital ASIC systems should proveide greater detailed analysis and more advanced capability.

7.1.2 Applications on Alternative Wide Bandgap Semiconductors

Thallium bromide[1] is an alternative room temperature semiconductor material that has been studied using the digital pulse waveform processing system described in this thesis. One of the shortcomings of current TlBr detectors is the phenomenon of polarization which significantly limits the lifetime of a detector. Because the detector lifetime is on the order of days or even hours, digital waveform collection is a critical tool because it allows the pulse waveforms to be saved for future analysis. This saved waveform list can then be used repeatedly to study items including noise, polarization, and gamma-ray spectroscopy. An algorithm has also been developed to use the cathode waveform to study the electric field distribution in a pixelated detector [47].

7.2 Conclusions

The current generation of gamma-ray imaging spectrometers based on the 3-D position sensing method relies on analog circuitry to sense the motion of charge in a pixelated semiconductor detector. The information that can be obtained from this design is limited. Analog systems rely on shaping amplifiers to provide estimates of pulse amplitude and time relative to other pulses. This shaping process destroys the detailed history of charge motion that exists in the preamplifier output signal. A motivating principle behind digital readout technology is the preservation and utilization of this time dependent record of charge motion. The direct readout of

[1]For a discussion of the historical context and early work on thallium bromide, see references [50] and [55].

preamplifier output signal opens the door to new techniques including: digital optimization of signal to noise ratio for energy and time estimates, sub-pixel position resolution, advanced charge transport analysis, and digital event classification.

Event-by-event classification of radiation events in pixelated CZT and HgI_2 detectors has been achieved through analysis of preamplifier waveforms of collecting pixels, neighbor pixels. Waveform based algorithms are powerful because the preamplifier signals contain the detailed charge drift and collection process history of the electron cloud in the detector. Digital signal processing methods are optimized to measure the different signal features in the waveform. Precise measurements of these features enable detection of signatures of photoelectric absorption, Compton scattering, X-ray escape, pair production, and charge sharing events. Application of these classification algorithms to real detector data has demonstrated improvements in single and multiple pixel energy resolutions.

Energy resolution is improved through more accurate event reconstruction. At 662 keV this improvement ranged between 3% and 6% without losing efficency and up to 30% in HgI_2 if only known-photoelectric absorption events are used. Event classification based on digitized pulse waveforms allow for a more accurate event reconstruction because it can distinguish small amounts of charge collected by neighbor pixels. In the analog system, this small amount of charge is impossible to measure if it is below the noise level or signal baseline threshold. In this case, an event may be improperly classified as a single pixel event leading to a low energy tail in the photopeak. The digital system can sense this small amount of charge and apply the correct energy reconstruction algorithm. This is done by separating the preamplifier into regions: baseline, charge collection region, and tail. Careful analysis of these regions is made easier through use of optimized digital signal processing algorithms.

If charge sharing is sensed, it will be considered in the multiple pixel analysis algorithms. Charge sharing is a particularly important type of event to classify. As photon energy increases, charge sharing is unavoidable and will occur in every event when the electron cloud dimensions exceed the pixel pitch. Cloud sizes can also increase in size due to diffusion if significantly thicker detectors are developed. Besides charge sharing, this method of reconstruction can be applied to Compton scatter and pair production events. Pair production events are unique. If the presence and location of annihilation radiation can be determined, the original energy can be reconstructed by simply adding the energy equivalent to two electron masse energies to the energy deposited at the annihilation site.

Imaging efficiency is improved through more accurate Compton scatter event identification and sequence, and sub pixel position estimates. Event classification provides a more accurate Compton scatter identification because it can separate Compton events from charge sharing and pair production. This is done by measuring the time difference between neighbor events and checking for transient pulses. Compton scatter can also be identified within a single pixel. Event classification can also provide a more accurate Compton sequence reconstruction in detectors with a measureable characteristic X-ray. Event classification is the critical first step to any sub-pixel position estimate. There are separate algorithms for single pixel, Compton scatter, and charge sharing sub-pixel estimates. Correct identification of the event will provide more accurate and efficient sub pixel estimates because events will be passed to appropriate algorithms and less events will be discarded.

The sub-pixel position calculation methods described in chapter V allows for a new level of precision for measuring interaction position in pixelated semiconductor detectors. This precision enables more accurate imaging measurements. At 662keV,

the sup-pixel resolution was mesured to be 230 μm. Sub-pixel information also enables a new level of precision in terms of detector response calibrations. Inherent to the pixelated design is response non-uniformity. Events that occur anywhere within a pixel pitch can be better calibrated using sub-pixel information.

The software developed for this project is modular and separate functions can be called by the main program or other functions to collect, process, calibrate, classify, and reconstruct events in a 3-D position sensitive semiconductor detector. The accuracy of the software has been demonstrated for each module. The event classification algorithms are based on the theoretical detector response for specific interaction types described in chapter II. The accuracy of these algorithms has been validated in chapter VI using simulation tools, a collimator experiment, and sub-pixel interaction position experiment.

BIBLIOGRAPHY

BIBLIOGRAPHY

[1] *Application Note: AN-282, Fundamentals of Sampled Data Systems.* Analog Devices, P.O. Box 9106, Norwood, Mass. 02062.

[2] *Maxwell.* Ansoft, Pittsburgh, PA.

[3] L. Bardelli and G. Poggi. Digital-sampling systems in high-resolution and wide dynamic-range energy measurements: Comparison with peak sensing ADCs. *Nucl. Instrum. Meth. Phys. Res. A*, 560:517523, 2006.

[4] H.H. Barrett. Charge transport in arrays of semiconductor gamma-ray detectors. *Physical Review Letters*, 75(1):156–159, 1995.

[5] Z.W. Bell. Tests on a digital neutron-gamma pulse shape discriminator with NE213. *Nucl. Instrum. Meth. Phys. Res.*, 188:105–109, 1981.

[6] M.J. Berger, J.H. Hubbell, S.M. Seltzer, J. Chang, J.S. Coursey, R. Sukumar, and D.S. Zucker. *XCOM: Photon Cross Sections Database, Version 3.1.* National Institute of Standards and Technology, 1998. `http://physics.nist.gov/PhysRefData/Xcom/Text/XCOM.html`, Accessed Nov 15, 2009.

[7] J.F. Butler, F.P. Doty, B. Apotovsky, J. Lajzerowicz, and L. Verger. Gamma- and x-ray detectors manufactured from $Cd_{1-x}Zn_xTe$ grown by a high pressure bridgman method. *Materials Science and Engineering B*, B16:291–295, 1993.

[8] J.F. Butler, F.P. Doty, C. Lingren, and B. Apotovsky. Cadmium zinc telluride detectors for industrial radiation measurement. *Appl. Radiat. Isot.*, 44(10/11):291–295, 1993.

[9] CERN. *GEANT4.* Geneva, Switzerland, 2003.

[10] C. Chen, W.R. Cook, F.A. Harrison, J.Y. Lin, and P.H. Maoa. Characterization of the HEFT CdZnTe pixel detectors. *Proceedings of SPIE*, 5198:9–18, 2004.

[11] M. Cromaz and et al. A digital signal processing module for gamma-ray tracking detectors. *Nucl. Instrum. Meth. Phys. Res. A*, 597:233237, 2008.

[12] B. Donmez, J. Kim, and He. Z. 3D position sensing on UltraPeRL CdZnTe detectors. *2007 IEEE Nuclear Science Symposium Conference Record*, pages 420–423, 2007.

[13] F.P. Doty, H.B. Barber, F.L. Augustine, J.F. Butler, B. Apotovsky, E.T. Young, and W. Hamilton. Pixellated CdZnTe detector arrays. *Nucl. Instrum. Methods Phys. Res. A*, A 353:356–360, 1994.

[14] R.D. Evans. *The Atomic Nucleus.* Krieger, New York, 1982.

[15] R.B Firestone. *1999 Update of the Table of Isotopes.* John Wiley and Sons, Inc, New York, eigth edition, 1999.

[16] O.R. Frisch. Isotope analysis of uranium samples by means of their a-ray groups. *British Atomic Energy Agency Report BR-49*, 1944.

[17] G. Geronimo, E. Vernon, K. Ackley, A. Dragone, J. Fried, P. OConnor, Z. He, C. Herman, and F. Zhang. Readout ASIC for 3D position-sensitive detectors. *IEEE Transactions on Nuclear Science*, 55(3):1593–1603, 2008.

[18] F.S. Goulding and D.A. Landis. Signal processing for semiconductor detectors. *IEEE Transactions on Nuclear Science*, NS-29(3):1125–1141, 1982.

[19] J. Hayward. *Charge Loss Correction and Inter-Strip Position Interpolation in a HPGe Double-Sided Strip Detector*. University of Michigan, Ann Arbor, MI, 2007. Ph.D. Dissertation.

[20] J. Hayward and D. Wehe. Observation of charge-sharing in an hpge double-sided strip detector. *Nucl. Instrum. Methods Phys. Res. A*, A579:99–103, 2007.

[21] J. Hayward and D. Wehe. Charge loss correction in a high-purity germanium double-sided strip detector. *IEEE Transactions on Nuclear Science*, 55(5):2789–2797, 2008.

[22] J. Hayward and D. Wehe. Incomplete charge collection in a hpge double-side strip detector. *Nucl. Instrum. Methods Phys. Res. A*, A586:215–223, 2008.

[23] Z. He. Review of shockley-ramo theorem and its applications in semiconductor gamma ray detectors. *Nucl. Instrum. Meth. Phys. Res. A*, 463:250–267, 2001.

[24] Z. He, G.F. Knoll, D.K. Wehe, and J. Miyamoto. Position sensitive single carrier CdZnTe detectors. *Nucl. Instrum. Meth. Phys. Res. A*, 388:180–185, 1997.

[25] Z. He, G.F. Knoll, D.K. Wehe, R. Rojeski, C.H. Mastrangelo, M. Hammig, C. Barrett, and A. Uritani. 1-D position sensitive single carrier semiconductor detectors. *Nucl. Instrum. Meth. Phys. Res. A*, 380:228–231, 1996.

[26] Z. He, W. Li, G.F. Knoll, D.K. Wehe, J. Berry, and C.M. Stahle. 3-D position sensitive cdznte gamma-ray spectrometers. *Nucl. Instrum. Meth. Phys. Res. A*, 422:173–178, 1999.

[27] J. Hong, A. Copete, J.E. Grindlay, S.V. Vadawale, W.W. Craig, R. Harrison, W.R. Cook, and N. Gehrels. Detector and telescope development for protoEXIST and fine beam measurements of spectral response of CZT detectors. *Proceedings of SPIE*, 5898, 2005.

[28] J. Hong and J.E. et al. Grindlay. Czt imaging detectors for protoexist. *Proceedings of SPIE*, 6319, 2006.

[29] W. Kaye, J. Berry, F. Zhang, and Z. He. Depth reconstruction validation in pixelated semiconductor detectors. *Nuclear Science Symposium Conference Record*, pages 1768 – 1770, 2009.

[30] J.C. Kim, S.E. Anderson, W. Kaye, S. Joshi, Y. Zhu, F. Zhang, and Z. He. Study on effect of charge sharing events in common-grid pixelated CdZnTe detectors. *Nuclear Science Symposium Conference Record*, pages 1640 – 1646, 2009.

[31] J.C. Kim, W. Kaye, F. Zhang, and Z. He. Study on energy resolution degradation in simple pixel CZT detectors through system modeling. *IEEE Transactions on Nuclear Science*, Submitted for Publication, 2009.

[32] J.C. Kim, W. Kaye, F. Zhang, and Z. He. Study on effect of charge sharing events in common-grid pixelated CdZnTe detectors. *IEEE Transactions on Nuclear Science*, To Submitted for Publication, 2010.

[33] Glenn F. Knoll. *Radiation Detection and Measurement*. John Wiley and Sons, Inc, Hoboken, NJ, third edition, 2000.

[34] M.O. Krause. Atomic radiative and radiationless yields for K and L shells. *Journal of Physical and Chemical Reference Data*, 8(2):307–327, 1979.

[35] T. Kroll and D. Bazzacco. A genetic algorithm for the decomposition of multiple hit events in the gamma-ray tracking detector MARS. *Nucl. Instrum. Meth. Phys. Res. A.*, 565:691–703, 2006.

[36] I.Y. Lee. Gamma-ray tracking detectors. *Nucl. Instrum. Meth. Phys. Res. A.*, 422:195–200, 1999.

[37] I.Y. Lee and et al. Gretina: A gamma ray energy tracking array. *Nuclear Physics A*, 746:255–259, 1993.

[38] W. Li. *Three-dimensional position sensitive CdZnTe gamma ray spectrometers.* University of Michigan, Ann Arbor, MI, 2001. Ph.D. Dissertation.

[39] W. Li, Z. He, G.F. Knoll, D.K. Wehe, and J.E. Berry. A data acquisition and processing system for 3d position sensitive czt gamma-ray spectrometers. *IEEE Transactions on Nuclear Science*, 46(6):1989–1994, 1999.

[40] P.N. Luke. Single-polarity charge sensing in ionization detectors using coplanar electrodes. *Applied Physics Letters*, 65(22):2884–2886, 1994.

[41] P.N. Luke. Unipolar charge sensing with coplanar electrodes-application tosemiconductor detectors. *IEEE Transactions on Nuclear Science*, 42(4):207–213, 1995.

[42] W. McMaster, N. Kerrdelgrande, J. Mallett, and J. Hubbell. *Compilation of X-ray cross sections UCRL-50174, section II revision 1.* University of California, Lawrence Radiation Laboratory, Berkeley, CA, 1969.

[43] R.E. McMurray, G.S. Hubbard, P.F. Wercinski, and R.G. Keller. MeV gamma ray detection algorithms for stacked silicon detectors. *IEEE Transactions on Nuclear Science*, 40(4):882–889, 1993.

[44] L. J. Meng and Z. He. Estimate interaction timing in a large volume hgi2 detector usingcathode pulse waveforms. *Nucl. Instrum. Methods Phys. Res. A*, 545:234251, 2005.

[45] L. J. Meng and Z. He. Exploring the limiting timing resolution for large volume CZT detectors with waveform analysis. *Nucl. Instrum. Methods Phys. Res. A*, 550:435445, 2005.

[46] L. J. Meng, Z. He, B. Alexander, and J. Sandoval. Spectroscopic performance of thick HgI_2 detectors. *IEEE Trans. Nucl. Sci.*, 53(3):1706–1712, 2006.

[47] S.F. Nowicki, S.E. Anderson, and Z. He. Characterization of pixellated thallium bromide radiation detectors for gamma-ray spectroscopy. 2008.

[48] G. Pasquali, R. Ciaranfi, L. Bardelli, M. Bini, A. Boiano, F. Giannelli, A. Ordine, and G. Poggi. A DSP equipped digitizer for online analysis of nuclear detector signals. *Nucl. Instrum. Meth. Phys. Res. A*, 570:126132, 2007.

[49] F. Petry. Background recognition in germanium detectors by pulse shape analysis. *Prog.Part.Nucl.Phys.,*, 32:281–283, 1994.

[50] I.U. Rahman and R. Hofstadter. Thallium halide radiation detectors. *Physical Review B*, 29(6):3500 – 3507, 1984.

[51] S. Ramo. Currents induced by electron motion. *Proceedings of the I.R.E.*, pages 584–585, 1939.

[52] A. Robertson, G.C. Cormick, T.J. Kennett, and W.V. Prestwich. Continuum reduction 1n the spectral response of Ge(Li) pair spectrometers. *Nucl. Instrum. Meth.*, 127:373–379, 1975.

[53] T.E. Schlesinger and R.B. James, editors. *Semiconductors for Room Temperature Nuclear Detector Applications*. Academic Press, San Diego, CA, 1995.

[54] G.J. Schmid, D. Beckedahl, J.J. Blair, A. Friensehner, and J.E. Kammeraad. HPGe compton suppression using pulse shape analysis. *Nucl. Instrum. Meth. Phys. Res. A.*, 422:368–372, 1999.

[55] K.S. Shaw, J.C. Lund, F. Olschner, L. Moy, and Squillante M.R. Thallium bromide radiation detectors. *IEEE Transactions on Nuclear Science*, 36(1):199–202, 1989.

[56] W. Shockley. Currents to conductors induced by a moving point charge. *Journal of Applied Physics*, 9:635–636, 1938.

[57] Helmuth Spieler. *Semiconductor Detector Systems*. Oxford University Press, New York, 2005.

[58] S.P. Swierkowski, G.A. Armantrout, and R. Wichner. High-resolution HgI_2 x-ray spectrometers. *Applied Physics Letters*, 23(5):281–282, 1973.

[59] E. Vernon, K. Ackley, G. Geronimo, J. Fried, Z. He, C. Herman, and F. Zhang. ASIC for high rate 3D position sensitive detectors. *2009 IEEE Nuclear Science Symposium Conference Record*, pages 412–417, 2009.

[60] W.R. Willig. Mercury iodide as a gamma spectrometer. *Nucl. Instrum. Methods*, 96(4):615–616, 1971.

[61] W.R. Willig. Large bandgap mercury and lead compounds for nuclear particle detection. *Nucl. Instrum. Methods*, 101(1):23–24, 1972.

[62] Dan Xu. *Gamma-Ray Imaging and Polarization Measure Using 3-D Position-Sensitive CdZnTe Detectors*. University of Michigan, Ann Arbor, MI, 2006. Ph.D. Dissertation.

[63] F. Zhang. *Events Reconstruction in 3-D Position Sensitive CdZnTe Gamma-Ray Spectrometers*. University of Michigan, Ann Arbor, MI, 2005. Ph.D. Dissertation.

[64] F. Zhang and Z. He. 3D position-sensitive CdZnTe gamma-ray spectrometers: improved performance with new ASICs. *Proceedings SPIE*, 5540:135143, 2004.

[65] F. Zhang and Z. He. New readout electronics for 3-D position sensitive CdZnTe/HgI2 detector arrays. *IEEE Tran. on Nucl. Sci.*, 53(5):3021–3027, 2006.

[66] F. Zhang and Z. He. Three-dimensional position sensitive CdZnTe detector array for PNNL. *2006 IEEE Nuclear Science Symposium Conference Record*, pages 3767–3771, 2006.

[67] F. Zhang, Z. He, G.F. Knoll, D.K. Wehe, and J.E. Berry. 3-D position sensitive CdZnTe spectrometer performance using third generation VAS/TAT readout electronics. *IEEE Tran. on Nucl. Sci.*, 52(6):2009–2016, 2005.

[68] F. Zhang, Z. He, D. Xu, G.F. Knoll, D.K Wehe, and J.E. Berry. Improved resolution for 3-D position sensitive CdZnTe spectrometers. *IEEE Transactions on Nuclear Science*, 51(5):2427–2431, 2004.

[69] Y. Zhu, S.E. Anderson, and Z. He. Sub-pixel position sensing for pixelated 3-D position sensitive wide band-gap semiconductor gamma-ray detectors. *EEE Transactions on Nuclear Science*, Submitted for Publication, 2010.